Electronic Supplementary Material (ESI) for Dalton Transactions.

Supporting information for

Modulation of the Magnetic and Photophysical Properties of 3d4f and 4f4f' Heterobimetallic Complexes Involving a Tetrathiafulvalene-Based Ligand

Haiet Douib,[a,b] *Jessica Flores Gonzalez,*[a] *Saskia Speed,*[c,d] *Vincent Montigaud,*[a] *Bertrand Lefeuvre,*[a] *Vincent Dorcet,*[a] *François Riobé,*[c] *Olivier Maury,*[c] *Abdelkrim Gouasmia,*[b] *Boris le Guennic,*[a] *Olivier Cador,**[a] *and Fabrice Pointillart**[a]

[a] Institut des Sciences Chimiques de Rennes UMR 6226 CNRS-UR1, Université de Rennes 1, 35042 Rennes Cedex, France

[b] Laboratoire des Matériaux Organiques et Hétérochimie (LMOH), Département des sciences de la matière, Université Larbi Tébessi de Tébessa, Route de Constantine 12002, Tébessa, Algérie.

[c] Univ Lyon, ENS de Lyon, CNRS UMR 5182, Université Claude Bernard Lyon 1, Laboratoire de Chimie, F69342, Lyon, France.

[d] Departament de Química Inorgànica i Orgànica, Secció de Química Inorgànica, Universitat de Barcelona, Martí i Franquès 1-11, 08028 Barcelona, Spain.

Olivier.cador@univ-rennes1.fr, fabrice.pointillart@univ-rennes1.fr

Experimental

Synthesis. **General Procedures and Materials**. The precursors Ln(hfac)$_3$·nH$_2$O (Ln(III) = Pr and Nd with n = 3, Dy and Yb with n = 2; hfac$^-$ = 1,1,1,5,5,5-hexafluoroacetylacetonate anion),[1] Dy(tta)$_3$·2H$_2$O[2] and the ligand 2-{1-[2,6-di(pyrazol-1-yl)-4-methylpyridyl]-4,5-[4,5-bis(propylthio)-tetrathiafulvalenyl]-1*H*-benzimidazol-2-yl}pyridine (**L**) were synthesized following previously reported methods.[3] All other reagents were purchased from Aldrich Co., Ltd. and used without further purification.

Synthesis of complexes 1-10.

[MLn(hfac)$_5$(L)]$_n$·x(CH$_2$Cl$_2$)·y(C$_6$H$_{14}$) (M=Cd, Ln=Dy, n=2, x=0 and y=0 (1); M=Zn, Ln=Dy, n=1, x=2 and y=1 (2); M=Zn, Ln=Yb, n=2, x=1 and y=2 (3); M=Mn, Ln=Dy, n=1, x=2 and y=0 (4); M=Mn, Ln=Yb, n=1, x=2 and y=0 (5); M=Co, Ln=Y, n=1, x=1 and y=0 (6); M=Co, Ln=Dy, n=1, x=2 and y=1 (7); M=Co, Ln=Yb, n=1, x=0 and y=0 (8); M=Ni, Ln=Dy, n=1, x=2 and y=1 (9); M=Ni, Ln=Yb, n=1, x=0 and y=0 (10)). 0.02 mmol of M(hfac)$_2$·2H$_2$O were dissolved in 5 mL of CH$_2$Cl$_2$ and then added to a solution of 10 mL of CH$_2$Cl$_2$ containing 14.8 mg of **L** (0.02 mmol). After 20 min of stirring, 0.02 mmol of Ln(hfac)$_3$·2H$_2$O previously dissolved in 5 mL of CH$_2$Cl$_2$ were added to the dark red mixture. 40 mL of *n*-hexane were layered at room temperature in the dark. Slow diffusion leads to dark red single crystals which are suitable for X-ray studies. Yields (**1**) 29 mg (71 %), (**2**) 30 mg (66 %),(**3**) 26 mg (63 %), (**4**) 34 mg (78 %), (**5**) 33 mg (76 %), (**6**) 29 mg (66 %), (**7**) 31 mg (69 %), (**8**) 26 mg (65 %), (**9**) 32 mg (70 %) and (**10**) 29 mg (71 %). Representative I.R.bands (KBr): 3142, 2970, 2932, 2871, 2878, 1655, 1578, 1556, 1531, 1502, 1465, 1410, 1258, 1205, 1146, 1056, 973, 797, 663 and 583 cm^{-1}. Anal. Calcd (%) for $C_{118}H_{70}Cd_2Dy_2F_{60}N_{16}O_{20}S_{12}$ (**1**): C 34.48, H 1.70, N 5.45; found: C 34.81, H 1.86 N, 5.29. Anal. Calcd (%) for $C_{67}H_{53}Cl_4ZnF_{30}N_8O_{10}S_6Dy$ (**2**): C 35.56, H 2.34, N 4.95; found: C 35.51, H 2.26 N, 4.89. Anal. Calcd (%) for $C_{119}H_{72}Zn_2Yb_2F_{60}N_{16}O_{21}S_{12}Cl_2$ (**3**): C 34.54, H 1.74, N 5.42; found: C 34.91, H 1.99 N, 5.29. Anal. Calcd (%) for $C_{61}H_{39}MnDyF_{30}N_8O_{10}S_6Cl_4$ (**4**): C 33.80, H 1.80, N 5.17; found: C 33.71, H 1.86 N, 5.09. Calcd (%) for $C_{61}H_{39}MnYbF_{30}N_8O_{10}S_6Cl_4$ (**5**): C 33.64, H 1.79, N 5.15; found: C 33.61, H 1.86 N, 5.19. Anal. Calcd (%) for $C_{67}H_{53}Cl_4CoF_{30}N_8O_{10}S_6Y$ (**6**): C 36.84, H 2.43, N 5.13; found: C 36.71, H 2.36 N, 5.05. Anal. Calcd (%) for $C_{67}H_{53}Cl_4CoF_{30}N_8O_{10}S_6Dy$ (**7**): C 35.64, H 2.35, N 4.97; found: C 35.61, H 2.30 N, 4.79. Anal. Calcd (%) for $C_{59}H_{35}CoF_{30}N_8O_{10}S_6Yb$ (**8**): C 35.22, H 1.74, N 5.57; found: C 35.61, H 1.99 N, 5.29. Anal. Calcd (%) for $C_{67}H_{53}Cl_4NiF_{30}N_8O_{10}S_6Dy$

(**9**): C 35.65, H 2.35, N 4.97; found: C 35.71, H 2.33 N, 4.78. Anal. Calcd (%) for $C_{59}H_{35}NiF_{30}N_8O_{10}S_6Yb$ (**10**): C 35.22, H 1.74, N 5.57; found: C 35.52, H 1.96 N, 5.37

Synthesis of the complex [ZnDy(tta)$_2$(hfac)$_3$(L)]·(CH$_2$Cl$_2$) (11). 10.4 mg of Zn(hfac)$_2$·2H$_2$O (0.02 mmol) were dissolved in 5 mL of CH_2Cl_2 and then added to a solution of 10 mL of CH_2Cl_2 containing 14.8 mg of **L** (0.02 mmol). After 20 min of stirring, 17.2 mg of Dy(tta)$_3$·2H$_2$O (0.02 mmol) previously dissolved in 5 mL of CH_2Cl_2 were added to the dark red mixture. 40 mL of *n*-hexane were layered at room temperature in the dark. Slow diffusion leads to red single crystals which are suitable for X-ray studies. Yield 19 mg (44 %). I.R. (KBr): 3138, 2965, 2929, 2874, 2878, 1657, 1604, 1582, 1534, 1504, 1462, 1411, 1355, 1308, 1254, 1201, 1144, 1058, 970, 792, 721, 660 and 581 cm^{-1}. Anal. Calcd (%) for $C_{66}H_{43}Cl_2DyZnF_{24}N_8O_{10}S_8$: C 37.37, H 2.03, N 5.28; found: C 37.51, H 2.16 N, 5.09.

Synthesis of the complex [Cu(hfac)(CH$_3$OH)(L')]·0.5(C$_6$H$_{14}$) (12). 10.4 mg of Cu(hfac)$_2$·2H$_2$O (0.02 mmol) were dissolved in 5 mL of CH_2Cl_2 and then added to a solution of 10 mL of CH_2Cl_2 containing 14.8 mg of **L** (0.02 mmol). After 20 min of stirring, 16.4 mg of Dy(hfac)$_3$·2H$_2$O (0.02 mmol) previously dissolved in 5 mL of CH_2Cl_2 were added to the dark red mixture. Few drops of MeOH were finally added leading to the formation of an orange solution. 40 mL of *n*-hexane were layered at room temperature in the dark. Slow diffusion leads to orange single crystals which are suitable for X-ray studies. Yield 11 mg (64 %). I.R. (KBr): 3146, 2967, 2932, 2872, 1654, 1558, 1534, 1504, 1463, 1413, 1258, 1206, 1145, 799, 662 and 586 cm^{-1}. Anal. Calcd (%) for $C_{31}H_{31}CuF_6N_1O_3S_6$: C 43.08, H 3.59, N 1.62; found: C 43.01, H 3.66 N, 1.59.

Synthesis of the complex [Cu(H$_2$O)Dy(hfac)$_4$(L)]·[Dy(hfac)$_4$]·(CH$_2$Cl$_2$) (13). This compound was obtained using the same experimental protocol as for **12** except that no methanol was used. Slow diffusion of *n*-hexane leads to purple single crystals which are suitable for X-ray studies. Yield 38 mg (66 %). I.R. (KBr): 3138, 3093, 2967, 2934, 2876, 1654, 1617, 1575, 1529, 1492, 1468, 1259, 1208, 1144, 793, 664 and 585 cm^{-1}. Anal. Calcd (%) for $C_{75}H_{40}Cl_2CuDy_2F_{48}N_8O_{17}S_6$: C 31.15, H 1.38, N 3.88; found: C 31.11, H 1.36 N, 3.93.

[Pr(hfac)$_3$(L)]$_2$·0.25(CH$_2$Cl$_2$)·0.5(C$_6$H$_{14}$) (14). 32.7 mg of Pr(hfac)$_3$·3H$_2$O (0.04 mmol) were dissolved in 10 mL of CH_2Cl_2 and then added to a solution of 10 mL of CH_2Cl_2 containing 14.8 mg of **L** (0.02 mmol). After 1 h of stirring, 40 mL of *n*-hexane were layered at room temperature in the dark. Slow diffusion leads to orange single crystals which are suitable for X-ray studies. Yield 25 mg (41 %). Anal. Calcd (%) for $C_{101.25}H_{73.5}Cl_{0.5}Pr_2F_{36}N_{16}O_{12}S_{12}$: C 39.52, H 2.39, N 7.29; found: C 39.49, H 2.36 N, 7.24. I.R. (KBr): 2957, 2870, 2853, 1654, 1574, 1557, 1532, 1506, 1465, 1410, 1258, 1207, 1146, 1099, 1057, 975, 799, 660 and 587 cm^{-1}.

$[Dy_{1.21}Nd_{0.79}(hfac)_6(L)]\cdot 2(CH_2Cl_2)\cdot(C_6H_{14})$ (15). 16.4 mg of $Nd(hfac)_3\cdot 3H_2O$ (0.02 mmol) were dissolved in 5 mL of CH_2Cl_2 and then added to a solution of 10 mL of CH_2Cl_2 containing 14.8 mg of **L** (0.02 mmol). After 15 min of stirring at room temperature, 16.4 mg of $Dy(hfac)_3\cdot 2H_2O$ (0.02 mmol) dissolved in 5 mL of CH_2Cl_2 were added to the orange mixture leading to a deep red solution. After additional 15 min of stirring, 40 mL of *n*-hexane were layered at room temperature in the dark. Slow diffusion leads to deep red single crystals which are suitable for X-ray studies. Yield 31 mg (61 %). Anal. Calcd (%) for $C_{72}H_{54}Cl_4Dy_{1.21}F_{36}N_8Nd_{0.79}O_{12}S_6$: C 33.87, H 2.18, N 4.39; found: C 33.59, H 2.16 N, 4.48. I.R. (KBr): 3146, 2972, 2934, 2878, 1652, 1558, 1533, 1500, 1464, 1411, 1257, 1208, 1145, 1099, 1058, 974, 800, 661 and 585 cm^{-1}.

$[Dy_{1.11}Nd_{0.89}(tta)_3(hfac)_3(L)]$ (16). 16.4 mg of $Nd(hfac)_3\cdot 3H_2O$ (0.02 mmol) were dissolved in 5 mL of CH_2Cl_2 and then added to a solution of 10 mL of CH_2Cl_2 containing 14.8 mg of **L** (0.02 mmol). After 15 min of stirring at room temperature, 17.2 mg of $Dy(tta)_3\cdot 2H_2O$ (0.02 mmol) dissolved in 5 mL of CH_2Cl_2 were added to the orange mixture leading to a deep red solution. After additional 15 min of stirring, 40 mL of *n*-hexane were layered at room temperature in the dark. Slow diffusion leads to deep red single crystals which are suitable for X-ray studies. Yield 31 mg (61 %). Anal. Calcd (%) for $C_{73}H_{45}Dy_{1.11}F_{27}N_8Nd_{0.89}O_{12}S_9$: C 37.49, H 1.93, N 4.79; found: C 37.01, H 1.86 N, 4.48. I.R. (KBr): 3140, 2964, 2927, 2874, 1655, 1603, 1582, 1535, 1505, 1460, 1411, 1355, 1307, 1253, 1200, 1142, 1058, 969, 792, 720, 659 and 582 cm^{-1}.

$[Yb_{1.04}Nd_{0.96}(hfac)_6(L)]$ (17). 16.4 mg of $Nd(hfac)_3\cdot 3H_2O$ (0.02 mmol) were dissolved in 5 mL of CH_2Cl_2 and then added to a solution of 10 mL of CH_2Cl_2 containing 14.8 mg of **L** (0.02 mmol). After 15 min of stirring at room temperature, 16.6 mg of $Yb(hfac)_3\cdot 2H_2O$ (0.02 mmol) dissolved in 5 mL of CH_2Cl_2 were added to the orange mixture leading to a deep red solution. After additional 15 min of stirring, 40 mL of *n*-hexane were layered at room temperature in the dark. Slow diffusion leads to deep red single crystals which are suitable for X-ray studies. Yield 30 mg (64 %). Anal. Calcd (%) for $C_{70}H_{50}F_{36}N_8Yb_{1.04}Nd_{0.96}O_{12}S_6$: C 35.17, H 2.09, N 4.69; found: C 35.01, H 1.96

N, 4.78. I.R. (KBr): 3142, 2971, 2940, 2878, 1652, 1558, 1533, 1501, 1464, 1410, 1259, 1206, 1145, 1099, 1060, 975, 799, 661 and 583 cm^{-1}.

[Nd_2(hfac)$_6$(L)] (18). 32.8 mg of Nd(hfac)$_3$·3H_2O (0.04 mmol) were dissolved in 10 mL of CH_2Cl_2 and then added to a solution of 10 mL of CH_2Cl_2 containing 14.8 mg of **L** (0.02 mmol). After 15 min of stirring at room temperature, the orange solution was refluxed for 1h leading to a deep red solution. After additional 15 min of stirring at room temperature, 40 mL of *n*-hexane were layered at room temperature in the dark. Slow diffusion leads to deep red single crystals which are suitable for X-ray studies. Yield 32 mg (68 %). Anal. Calcd (%) for $C_{70}H_{50}F_{36}N_8Nd_2O_{12}S_6$: C 35.59, H 2.12, N 4.75; found: C 35.11, H 2.00 N, 4.80. I.R. (KBr): 3142, 2970, 2938, 2878, 1652, 1558, 1533, 1500, 1465, 1410, 1257, 1206, 1145, 1099, 1058, 975, 798, 661 and 585 cm^{-1}.

[YbPr(hfac)$_6$(L)] (19). **Method a**. 16.4 mg of Pr(hfac)$_3$·3H_2O (0.02 mmol) were dissolved in 5 mL of CH_2Cl_2 and then added to a solution of 10 mL of CH_2Cl_2 containing 14.8 mg of **L** (0.02 mmol). After 15 min of stirring at room temperature, 16.6 mg of Yb(hfac)$_3$·2H_2O (0.02 mmol) dissolved in 5 mL of CH_2Cl_2 were added to the orange mixture leading to a deep red solution. After additional 15 min of stirring, 40 mL of *n*-hexane were layered at room temperature in the dark. Slow diffusion leads to deep red single crystals which are suitable for X-ray studies. Yield 33 mg (71 %).

Method b. 15.4 mg of single crystals of **14** (0.005 mmol) were dissolved in 10 mL of CH_2Cl_2 and then added to a solution of 5 mL of CH_2Cl_2 containing 8.3 mg of Yb(hfac)$_3$·2H_2O (0.01 mmol) was added to the orange mixture leading to a deep red solution. After additional 15 min of stirring, 40 mL of *n*-hexane were layered at room temperature in the dark. Slow diffusion leads to deep red single crystals which are suitable for X-ray studies. Yield 18 mg (80 %).

Anal. Calcd (%) for $C_{64}H_{36}YbF_{36}N_8PrO_{12}S_6$: C 33.40, H 1.57, N 4.87; found: C 34.00, H 1.66 N, 4.62. I.R. (KBr): 3142, 2970, 2937, 2878, 1652, 1558, 1533, 1501, 1465, 1411, 1258, 1206, 1145, 1100, 1057, 973, 799, 660 and 585 cm^{-1}.

Crystallography. Single crystals of **1**, **3**, **4**, **6**, **8**, **11-13**, **15-19** were mounted on a D8 VENTURE Bruker-AXS diffractometer for data collection (MoK$_\alpha$ radiation source, λ = 0.71073 Å), from the Centre de Diffractométrie X (CDIFX), Université de Rennes 1, France while single crystal of **14** was mounted on a APEXII Bruker-AXS diffractometer (Tables S1 and S2).

Structures were solved with a direct method using the SHELXT program[4] and refined with a full matrix least-squares method on F^2 using the SHELXL-14/7 program[5]. For all the other compounds (**2**, **5**, **7**, **9** and **10**), the cells were record on the D8 VENTURE Bruker-AXS diffractometer (Table S3). SQUEEZE procedure of PLATON[6] was performed for structures containing large solvent accessible voids in which residual peak of diffraction were observed. The ratio of metallic center on each cristallographic site were fixed from the values determined by Energy Dispersive Spectrometry. Crystallographic data are summarized in Tables S1-S3. Complete crystal structure results as a CIF file including bond lengths, angles, and atomic coordinates are deposited as Supporting Information.

Physical Measurements. The elemental analyses of the compounds were performed at the Centre Régional de Mesures Physiques de l'Ouest, Rennes. The Ln/Ln' ratio of the compounds **15-17** were determined using SEM (Scanning Electron Microscopy). All observations and measurements were carried out with a JEOL JSM 6400 scanning electron microscope (JEOL Ltd., Tokyo, Japan) with an EDS (Energy Dispersive Spectrometry) analysis system (OXFORD Link INCA). The voltage was kept at 9 kV, and the samples were mounted on carbon stubs and coated for 5 min with a gold/palladium alloy using a sputter coater (Jeol JFC 1100). Each ratio given in the text is the average value between at least three measurements. This analysis has been performed by the "Centre de Microscopie Electronique à Balayage et microAnalyse (CMEBA)" from the University of Rennes 1 (France). Cyclic voltammetry was carried out in CH_2Cl_2 solution, containing 0.1 M $N(C_4H_9)_4PF_6$ as supporting electrolyte. Voltammograms were recorded at 100 mVs^{-1} at a platinum disk electrode. The potentials were measured *versus* a saturated calomel electrode (SCE). Absorption spectra were recorded on a Varian Cary 5000 UV-Visible-NIR spectrometer equipped with an integration sphere. The luminescence spectra were measured using a Horiba-Jobin Yvon Fluorolog-3® spectrofluorimeter, equipped with a three slit double grating excitation and emission monochromator with dispersions of 2.1 nm/mm (1200 grooves/mm). The steady-state luminescence was excited by unpolarized light from a 450 W xenon CW lamp and detected at a 90° angle by either a Hamamatsu R928 photomultiplier tube (300-800 nm) or an InGaAs near -infrared detector (850-1600 nm). The magnetization of all the compounds have been measured with a Quantum Design MPMS-XL operating between 2 and 300 K. For the $\chi_M T$ vs. T plots, with χ_M the molar magnetic susceptibility and T the temperature in Kelvin, two procedures have been applied depending on the amplitude of the magnetic moment. For Yb(III)-based samples a magnetic field of 2 kOe is applied below 20 K and of 10 kOe above. For Dy(III)-based samples a magnetic field of 0.2

kOe is applied below 20 K, 2 kOe between 20 and 80 K and finally 10 kOe above 80 K. All the magnetization curves have been measured at 2 K. In ac mode, an oscillating field of 3 Oe is applied at frequencies comprised between 1 and 1000 Hz with a Quantum Design MPMS-XL and between 10 and 10000 Hz with a Quantum Design PPMS. For all samples, the magnetization is corrected for intrinsic diamagnetism evaluated with Pascal's tables and the extrinsic diamagnetism of the sample holder (Teflon tape).

Details for EDS (Energy Dispersive Spectrometry) analysis:

$[Dy_{(1+x)}Nd_{(1-x)}(hfac)_6(L)]\cdot 2(CH_2Cl_2)\cdot(C_6H_{14})$ (15) (x = 0.21)

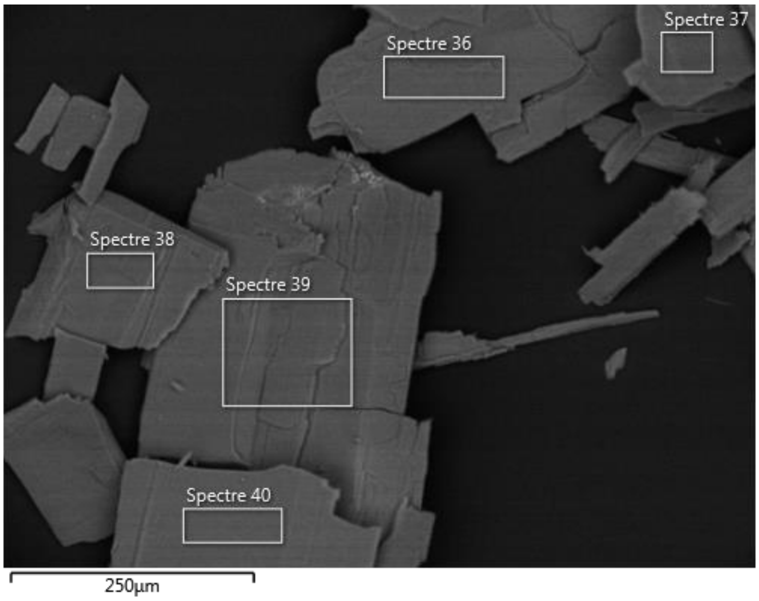

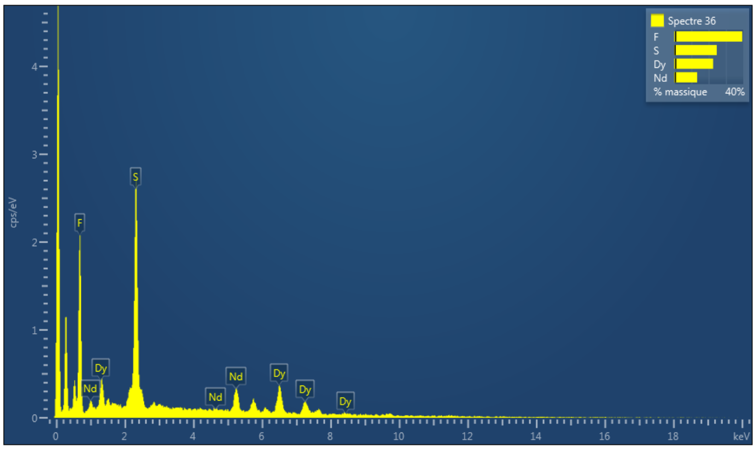

Element	Type of transition	% Mass	% atomic
F	K edge	39.43	67.47
S	K edge	24.68	25.02
Nd	L edge	13.32	3.00
Dy	L edge	22.56	4.51
Total:		100.00	100.00
Nd/Dy ratio (1-x)/(1+x)			0.65

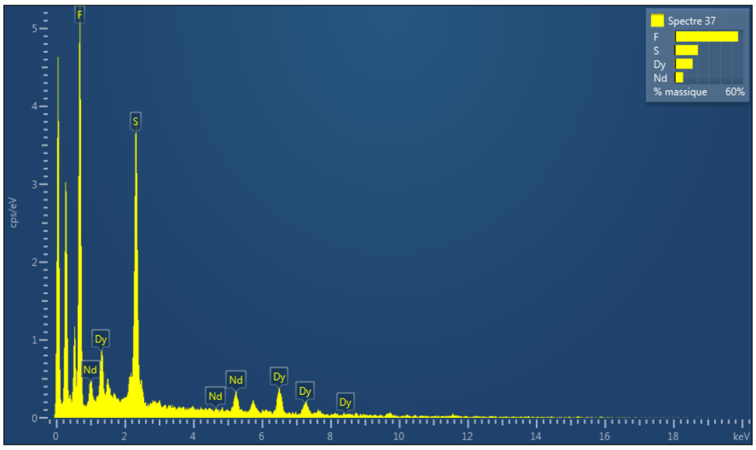

Element	Type of transition	% Mass	% atomic
F	K edge	55.50	78.57
S	K edge	20.65	17.32
Nd	L edge	7.82	1.46
Dy	L edge	16.03	2.65
Total:		100.00	100.00
Nd/Dy ratio (1-x)/(1+x)			0.55

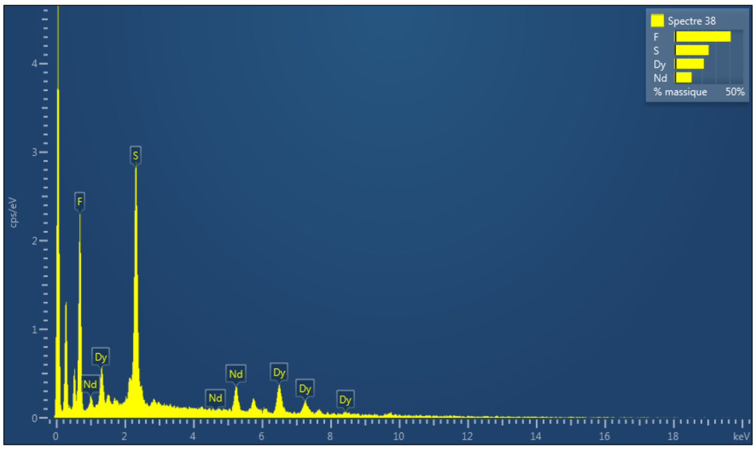

Element	Type of transition	% Mass	% atomic
F	K edge	40.93	68.35
S	K edge	24.93	24.67
Nd	L edge	12.64	2.78
Dy	L edge	21.50	4.20
Total:		100.00	100.00
Nd/Dy ratio (1-x)/(1+x)			0.66

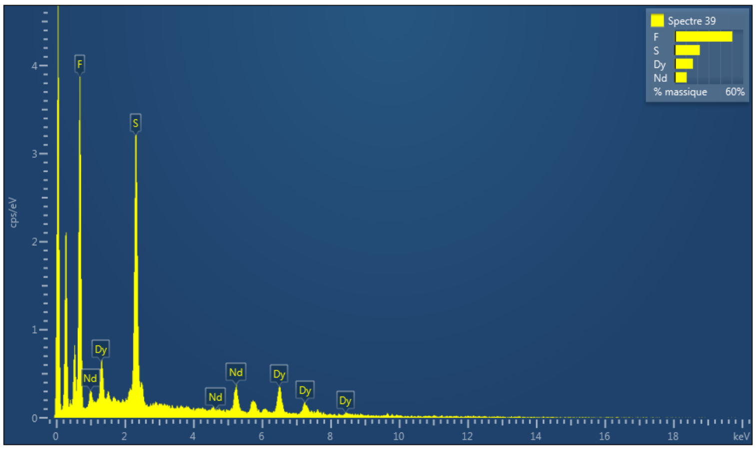

Element	Type of transition	% Mass	% atomic
F	K edge	50.52	75.32
S	K edge	22.31	19.71
Nd	L edge	10.86	2.13
Dy	L edge	16.31	2.84
Total:		100.00	100.00
Nd/Dy ratio (1-x)/(1+x)			0.75

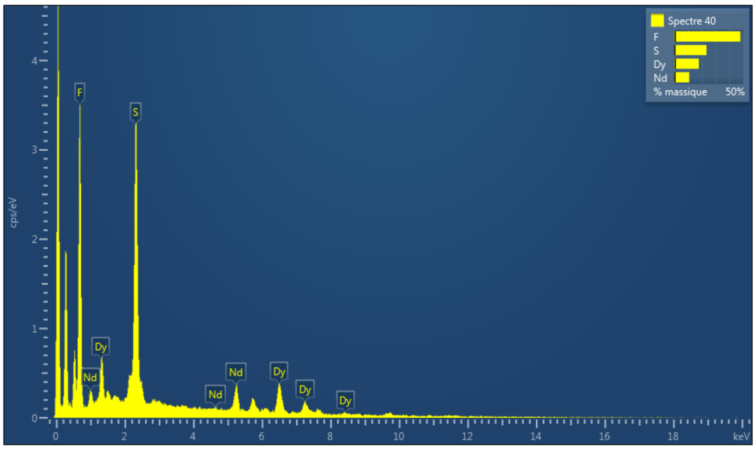

Element	Type of transition	% Mass	% atomic
F	K edge	47.87	73.36
S	K edge	23.39	21.24
Nd	L edge	10.88	2.20
Dy	L edge	17.86	3.20
Total:		100.00	100.00
Nd/Dy ratio (1-x)/(1+x)			0.75

$[Dy_{(1+x)}Nd_{(1-x)}(tta)_3(hfac)_3(L)]$ (16) (x = 0.11)

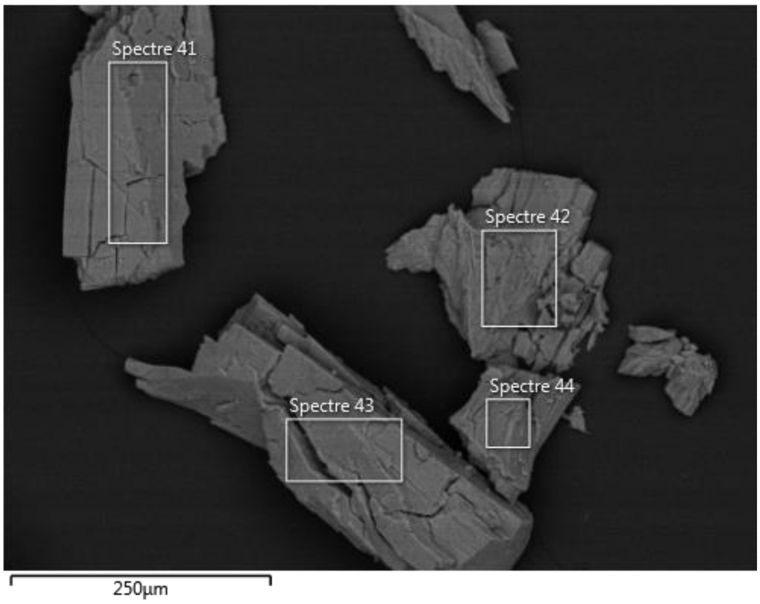

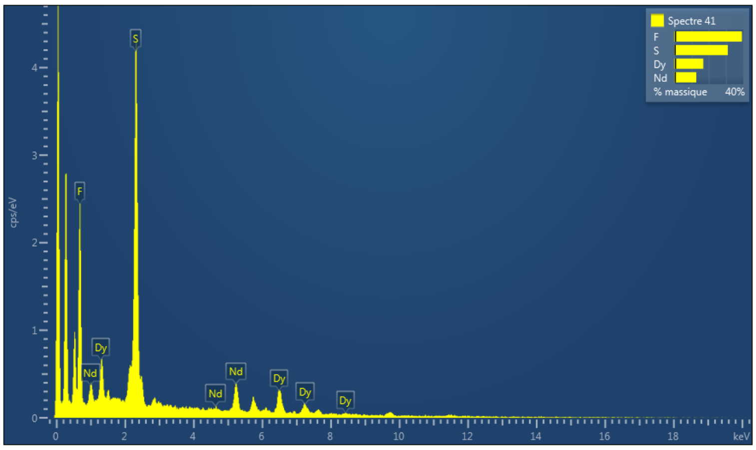

Element	Type of transition	% Mass	% atomic
F	K edge	39.21	63.98
S	K edge	31.08	30.05
Nd	L edge	12.83	2.76
Dy	L edge	16.87	3.22
Total:		100.00	100.00
Nd/Dy ratio (1-x)/(1+x)			0.86

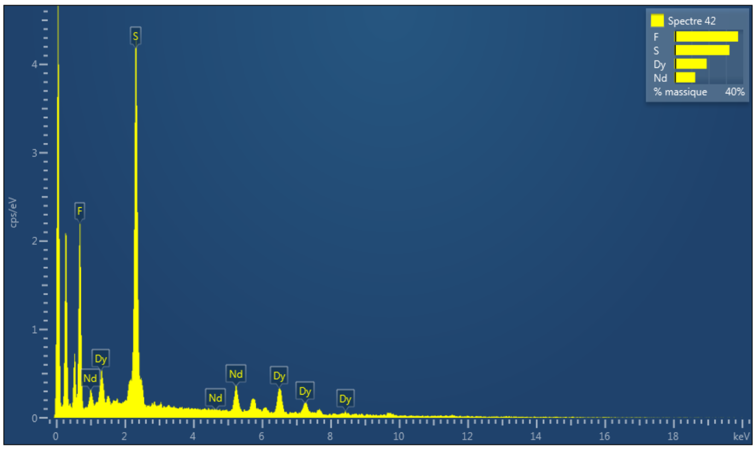

Element	Type of transition	% Mass	% atomic
F	K edge	36.99	61.90
S	K edge	32.00	31.73
Nd	L edge	12.16	2.68
Dy	L edge	18.85	3.69
Total:		100.00	100.00
Nd/Dy ratio (1-x)/(1+x)			0.73

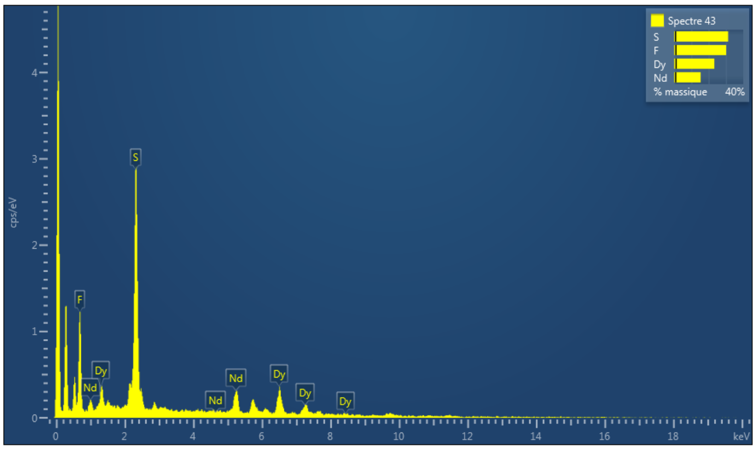

Element	Type of transition	% Mass	% atomic
F	K edge	30.11	56.39
S	K edge	31.30	34.73
Nd	L edge	15.33	3.78
Dy	L edge	23.26	5.09
Total:		100.00	100.00
Nd/Dy ratio (1-x)/(1+x)			0.74

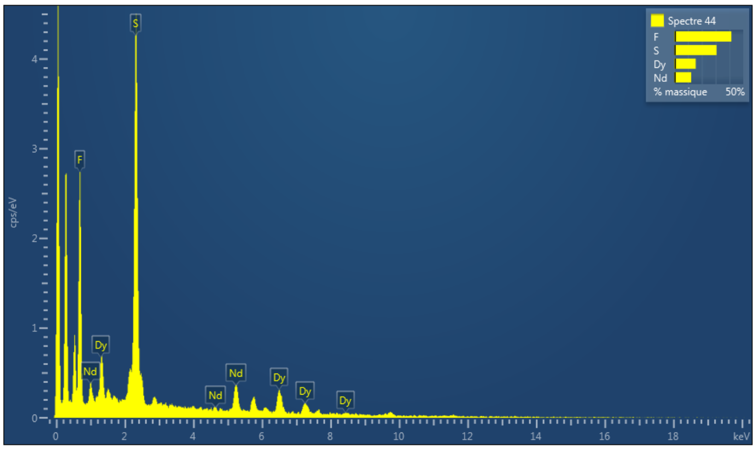

Element	Type of transition	% Mass	% atomic
F	K edge	41.44	65.74
S	K edge	30.64	28.80
Nd	L edge	12.31	2.57
Dy	L edge	15.61	2.89
Total:		100.00	100.00
Nd/Dy ratio (1-x)/(1+x)			0.74

$[Yb_{(1+x)}Nd_{(1-x)}(hfac)_6(L)]$ (17) (x = 0.04)

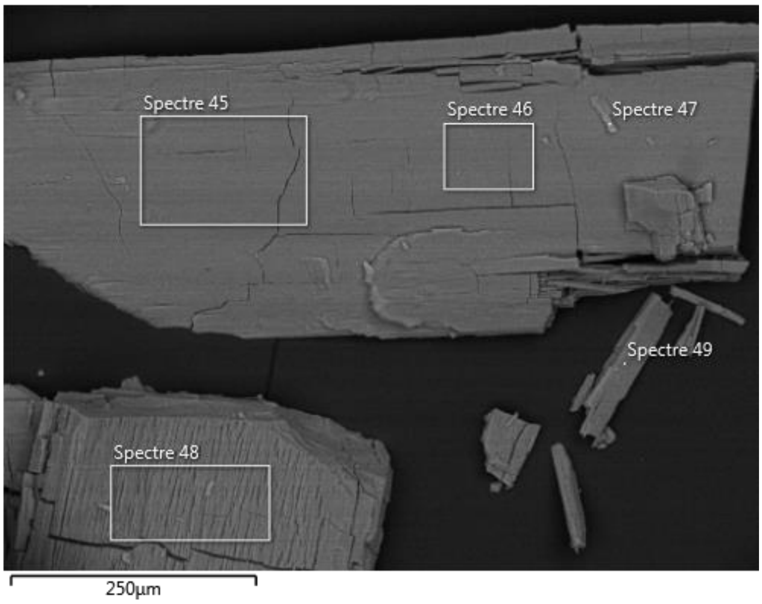

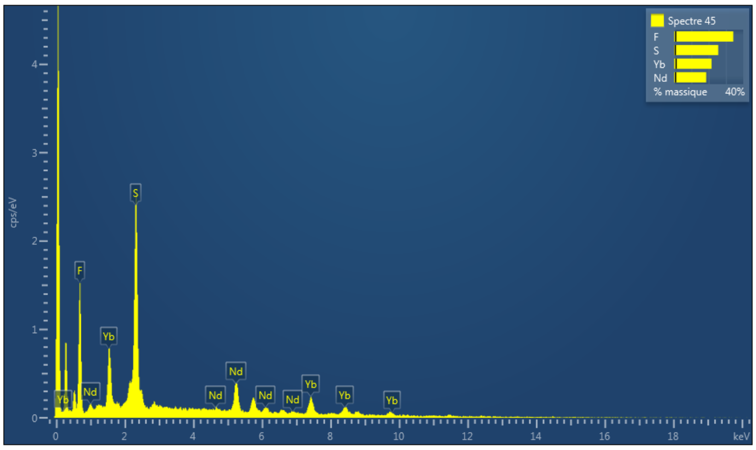

Element	Type of transition	% Mass	% atomic
F	K edge	34.27	63.19
S	K edge	25.56	27.92
Nd	L edge	18.54	4.50
Yb	L edge	21.64	4.38
Total:		100.00	100.00
Nd/Yb ratio (1-x)/(1+x)			1.03

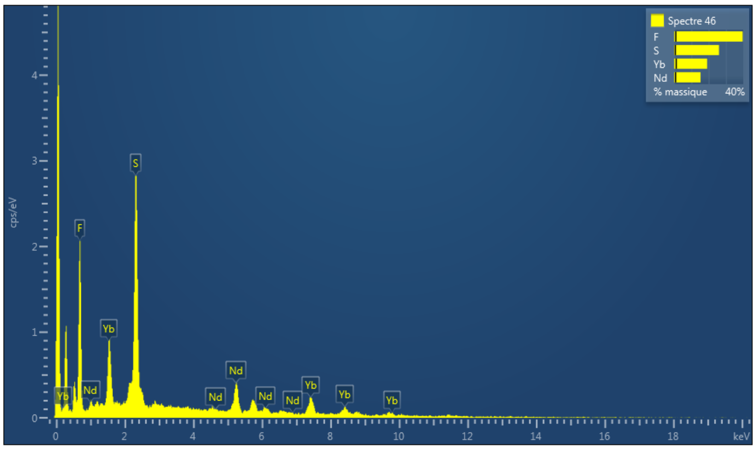

Element	Type of transition	% Mass	% atomic
F	K edge	39.66	67.03
S	K edge	25.99	26.03
Nd	L edge	15.26	3.40
Yb	L edge	19.09	3.54
Total:		100.00	100.00
Nd/Yb ratio (1-x)/(1+x)			0.96

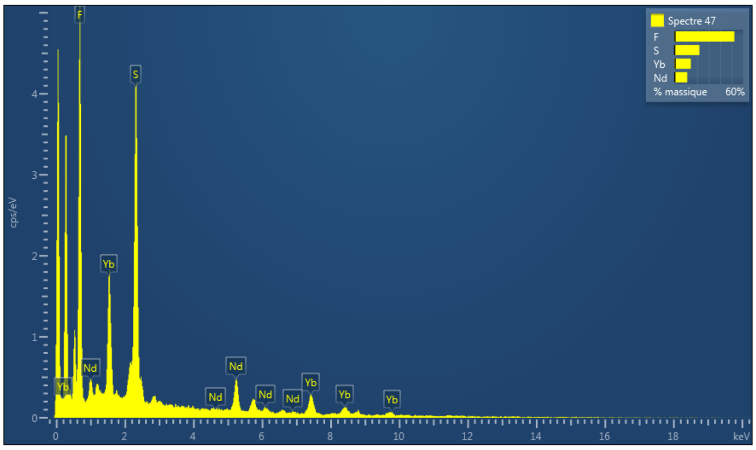

Element	Type of transition	% Mass	% atomic
F	K edge	52.26	76.48
S	K edge	21.92	19.01
Nd	L edge	11.35	2.19
Yb	L edge	14.47	2.33
Total:		100.00	100.00
Nd/Yb ratio (1-x)/(1+x)			0.94

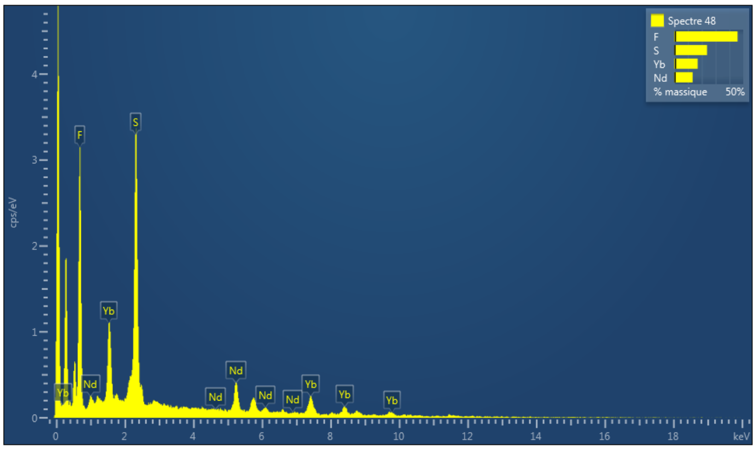

Element	Type of transition	% Mass	% atomic
F	K edge	45.87	72.14
S	K edge	23.78	22.16
Nd	L edge	13.36	2.77
Yb	L edge	16.99	2.93
Total:		100.00	100.00
Nd/Yb ratio (1-x)/(1+x)			0.95

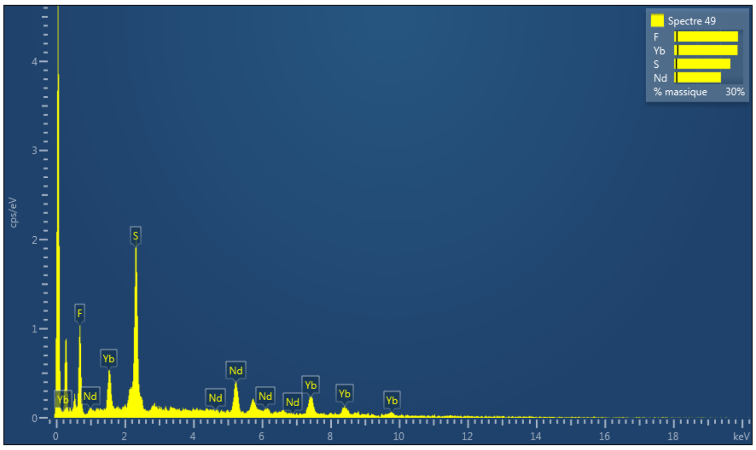

Element	Type of transition	% Mass	% atomic
F	K edge	27.71	57.87
S	K edge	24.43	30.23
Nd	L edge	20.32	5.59
Yb	L edge	27.54	6.31
Total:		100.00	100.00
Nd/Yb ratio (1-x)/(1+x)			0.89

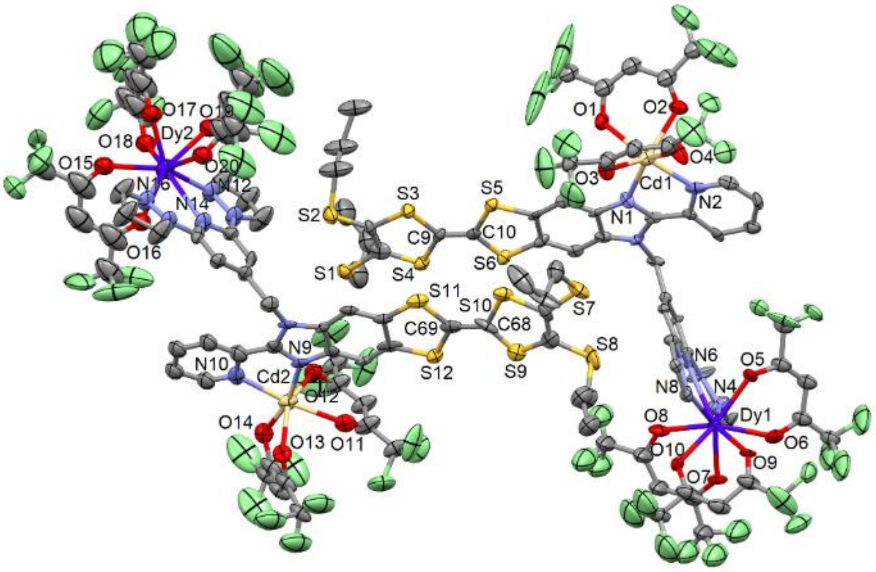

Figure S1. ORTEP view of **1**. Thermal ellipsoids are drawn at 30% probability. Hydrogen atoms and solvent molecules of crystallization are omitted for clarity.

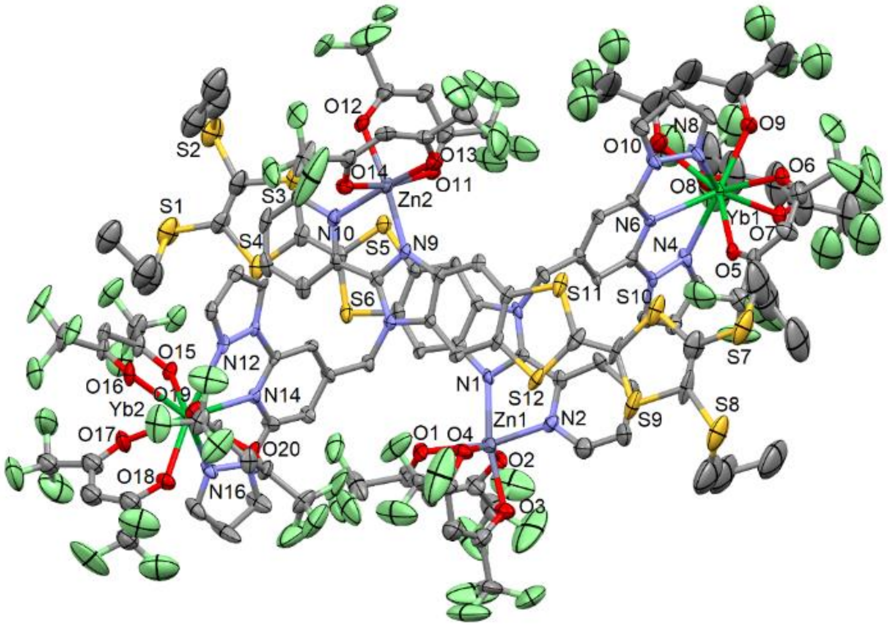

Figure S2. ORTEP view of **3**. Thermal ellipsoids are drawn at 30% probability. Hydrogen atoms and solvent molecules of crystallization are omitted for clarity.

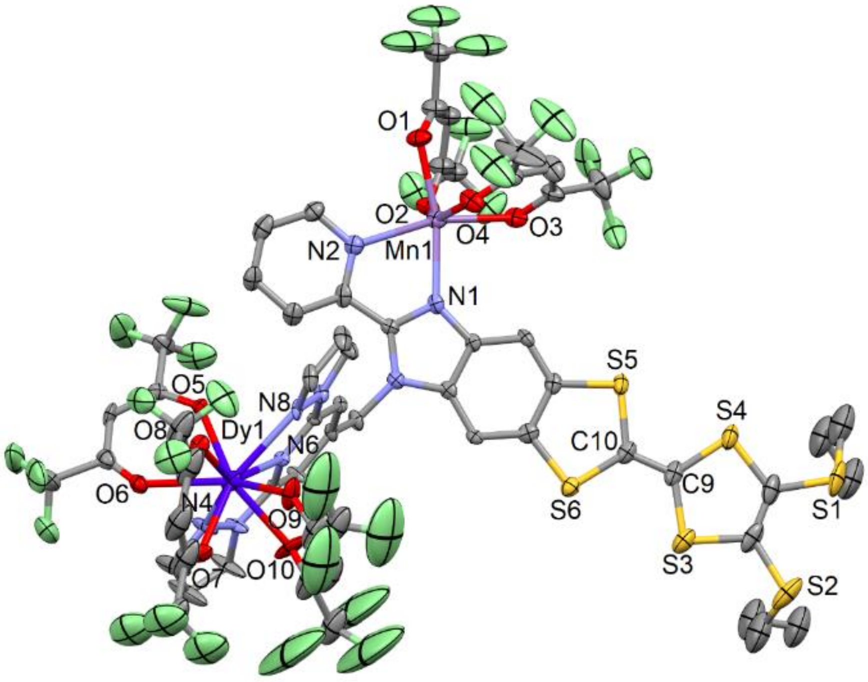

Figure S3. ORTEP view of **4**. Thermal ellipsoids are drawn at 30% probability. Hydrogen atoms and solvent molecules of crystallization are omitted for clarity.

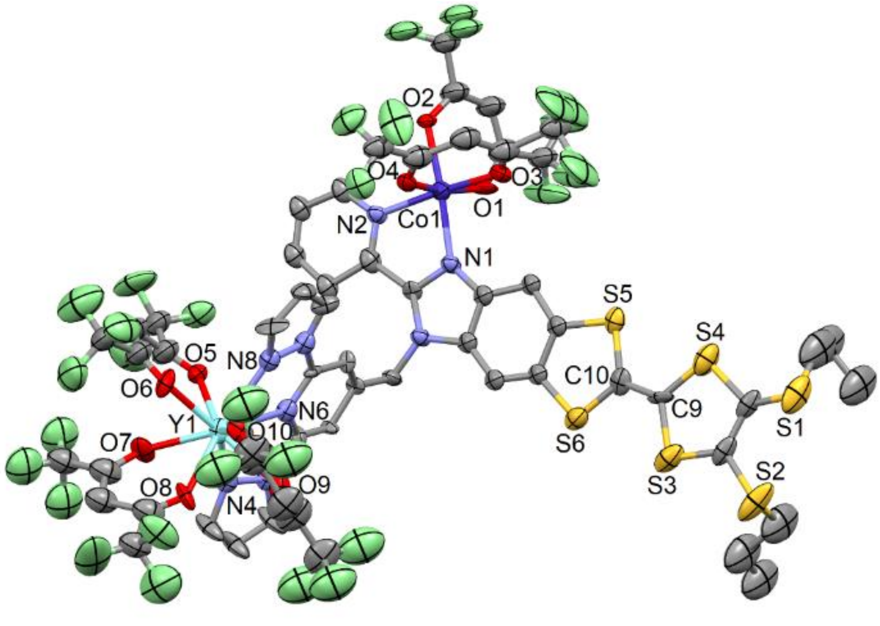

Figure S4. ORTEP view of **6**. Thermal ellipsoids are drawn at 30% probability. Hydrogen atoms and solvent molecules of crystallization are omitted for clarity.

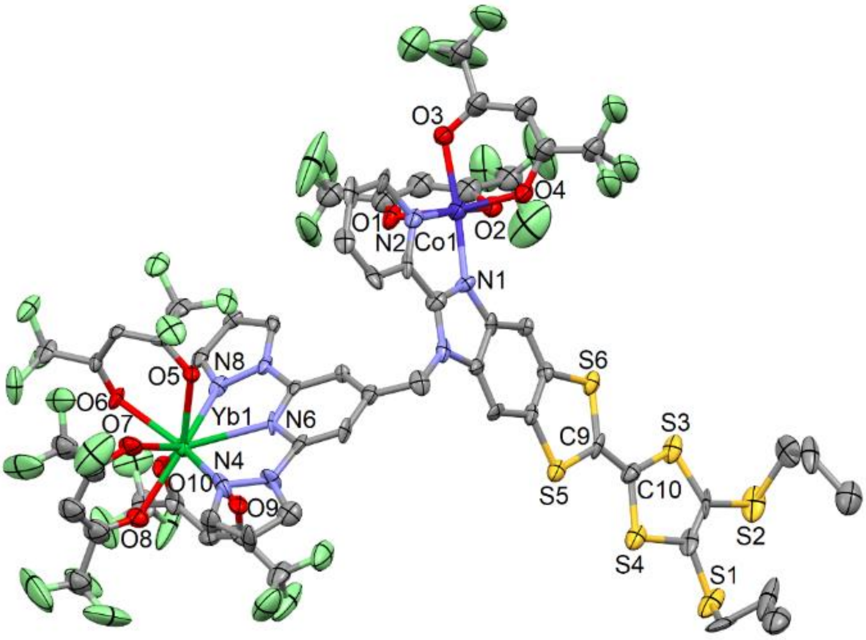

Figure S5. ORTEP view of **8**. Thermal ellipsoids are drawn at 30% probability. Hydrogen atoms and solvent molecules of crystallization are omitted for clarity.

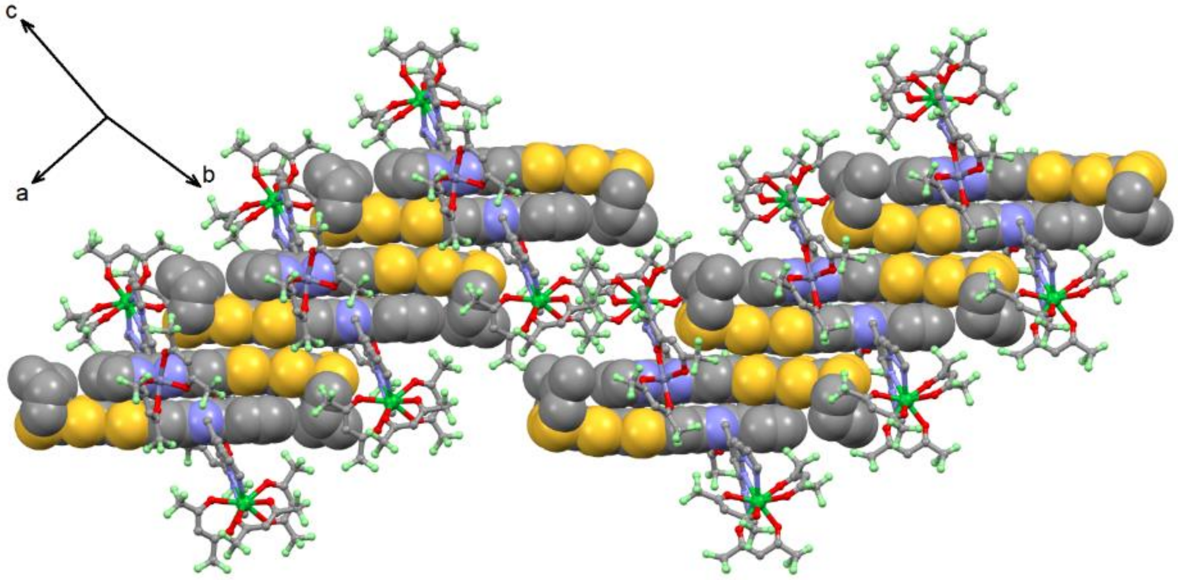

Figure S6. Crystal packing of **3**. The 4,5-[4,5-bis(propylthio)-tetrathiafulvalenyl]-1*H*-benzimidazol-2-yl}pyridine fragment is shown in spacefill representation while the dpp moiety and the organometallic precursors M(hfac)$_2$ and Ln(hfac)$_3$ are shown in ball and sticks representation.

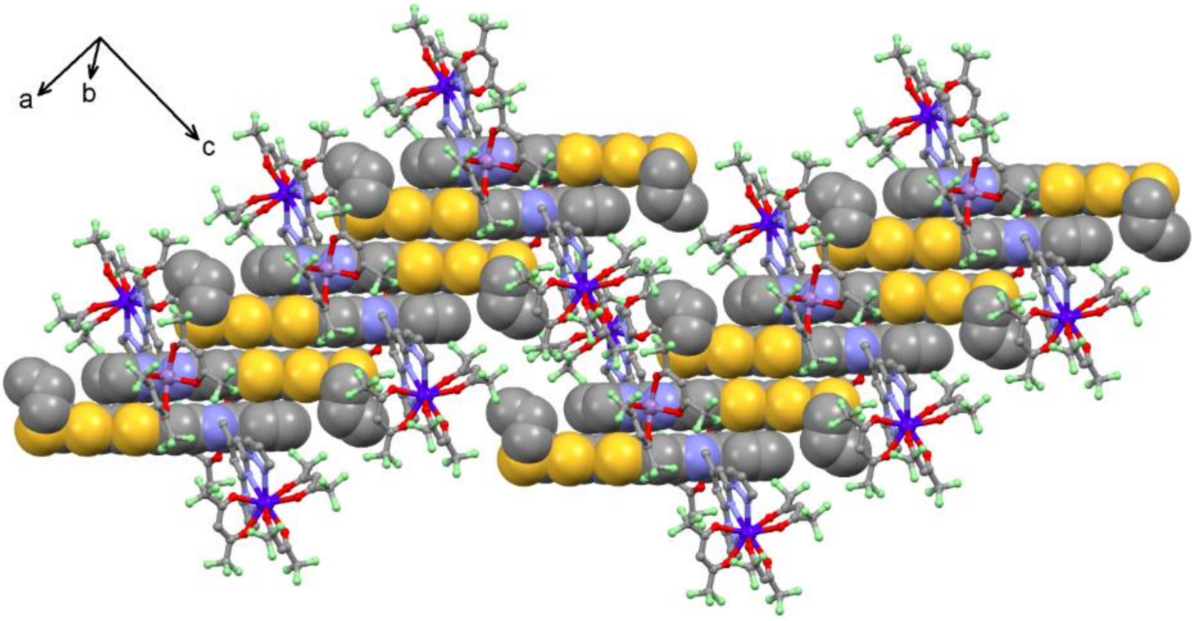

Figure S7. Crystal packing of **4**. The 4,5-[4,5-bis(propylthio)-tetrathiafulvalenyl]-1*H*-benzimidazol-2-yl}pyridine fragment is shown in spacefill representation while the dpp moiety and the organometallic precursors M(hfac)$_2$ and Ln(hfac)$_3$ are shown in ball and sticks representation.

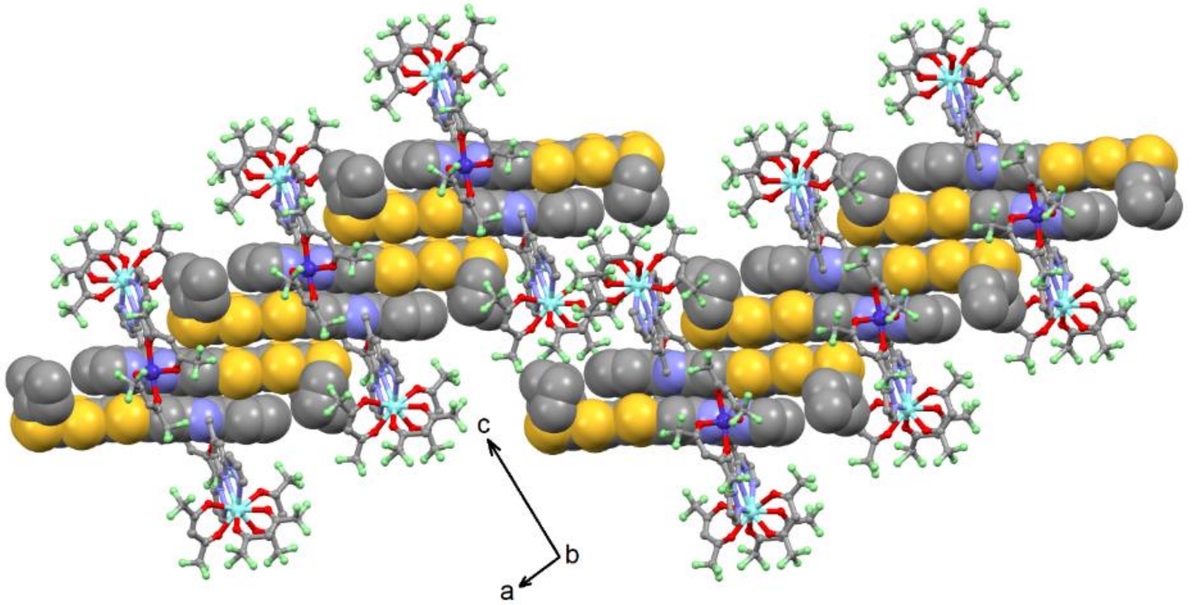

Figure S8. Crystal packing of **6**. The 4,5-[4,5-bis(propylthio)-tetrathiafulvalenyl]-1*H*-benzimidazol-2-yl}pyridine fragment is shown in spacefill representation while the dpp moiety and the organometallic precursors M(hfac)$_2$ and Ln(hfac)$_3$ are shown in ball and sticks representation.

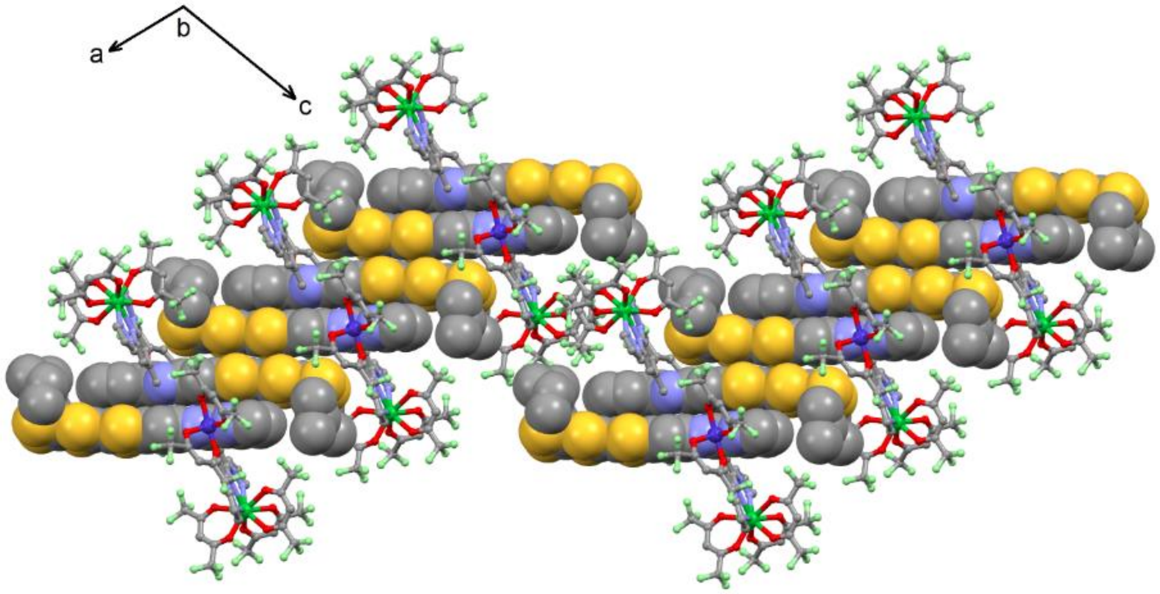

Figure S9. Crystal packing of **8**. The 4,5-[4,5-bis(propylthio)-tetrathiafulvalenyl]-1*H*-benzimidazol-2-yl}pyridine fragment is shown in spacefill representation while the dpp moiety and the organometallic precursors M(hfac)$_2$ and Ln(hfac)$_3$ are shown in ball and sticks representation.

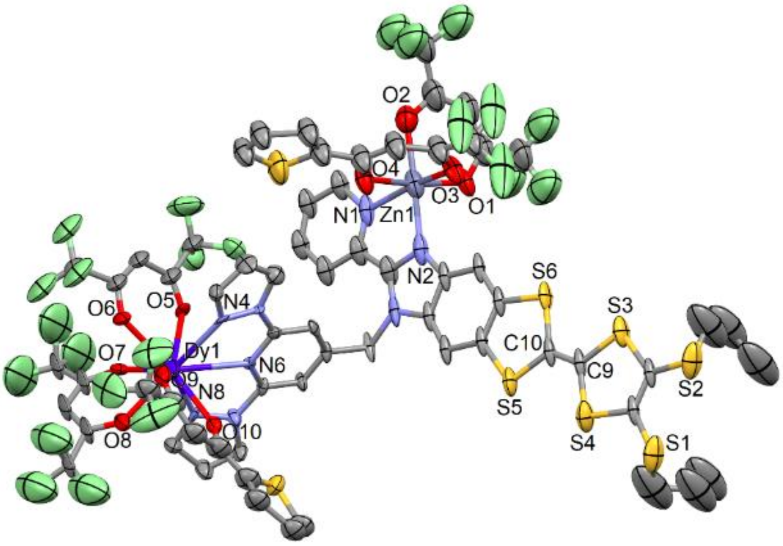

Figure S10. ORTEP view of **11**. Thermal ellipsoids are drawn at 30% probability. Hydrogen atoms and solvent molecules of crystallization are omitted for clarity.

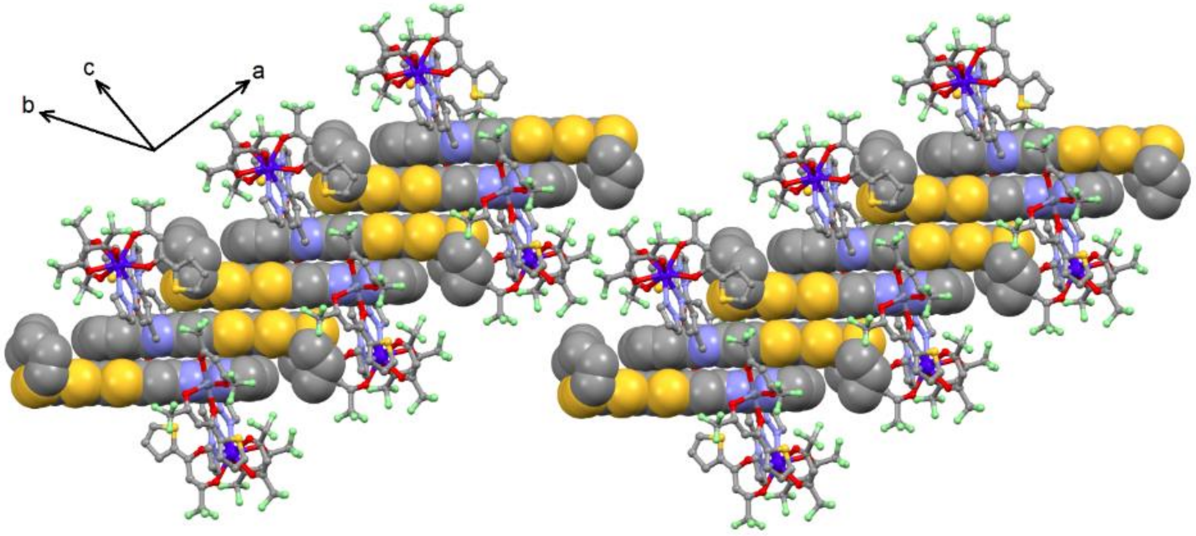

Figure S11. Crystal packing of **11**. The 4,5-[4,5-bis(propylthio)-tetrathiafulvalenyl]-1*H*-benzimidazol-2-yl}pyridine fragment is shown in spacefill representation while the dpp moiety and the organometallic precursors M(hfac)$_2$ and Ln(hfac)$_3$ are shown in ball and sticks representation.

The previous X-ray structures **1-10** have shown that Mn(II), Co(II), Ni(II), Zn(II) and Cd(II) can be inserted in the hetero-bimetallic complexes. The case of the insertion of a Cu(II) ion is special. In fact the coordination reaction of Cu(II) in presence of MeOH leads to the formation of a pure 3*d* complex of formula [Cu(hfac)(CH$_3$OH)(L')]·0.5(C$_6$H$_{14}$) (**12**) while in the absence of alcohol the formation of the unprecedented [Cu(H$_2$O)Dy(hfac)$_4$(L)]·[Dy(hfac)$_4$]·(CH$_2$Cl$_2$) (**13**) hetero-bimetallic complex is observed (see Supporting Informations for structural descriptions and Figures S12-S15).

[Cu(hfac)(CH$_3$OH)(L')]·0.5(C$_6$H$_{14}$) (12). **12** crystallizes in the P-1 (N°2) triclinic space group (Table S1). The X-ray structure reveales that the alkylated dpp fragment is not anymore present leading to the conclusion that the combination Cu(II)/alcohol allowed a N-dealkylation reaction to give the ligand 4,5-[4,5-bis(propylthio)-tetrathiafulvalenyl]-1*H*-benzimidazol-2-yl}pyridine (L'). Consequently only the bischelating site of coordination is available, it is occupied by the Cu(II) ion. The Cu(II) is coordinated to the N3 deprotonated amine and the N2 atom of the pyridine moiety (Figure S12). The negative charge of the N3 amine induced the loss of one hfac$^-$ of the Cu(hfac)$_2$ precursor and the axial position is occupied by one MeOH molecule. The Cu(II) lies in a N$_2$O$_3$ environment which can be described as a square pyramidal polyhedron with a long Cu1-O3 distance due to the Jahn-Teller effect.

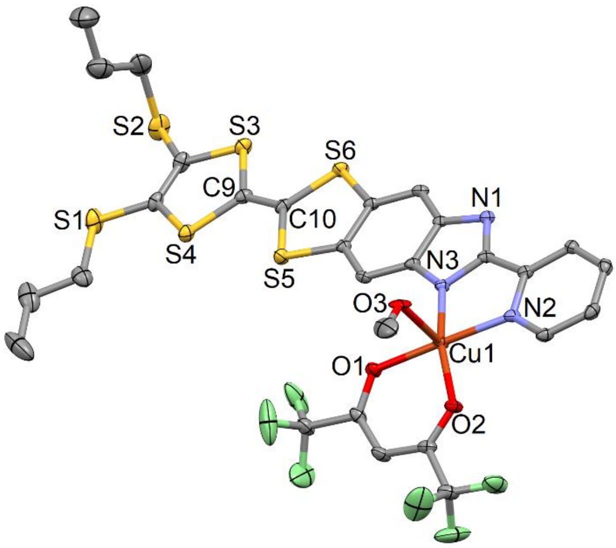

Figure S12. ORTEP view of **12**. Thermal ellipsoids are drawn at 30% probability. Hydrogen atoms and solvent molecules of crystallization are omitted for clarity.

The crystal packing highlights the formation of columns along the *a* axis composed of head-to-tail dimers (D-A dimers) and Acceptor-Acceptor (A-A) dimers (where A is the bzip fragment) (Figure S13). The D-A dimers are favored due to π-π interactions and the Cu1···S6 contacts in axial position while the A-A dimers are favored thanks to H-bonds between the coordinated MeOH and the imine of the imidazole fragment (N3···O3 = 2.784 Å).

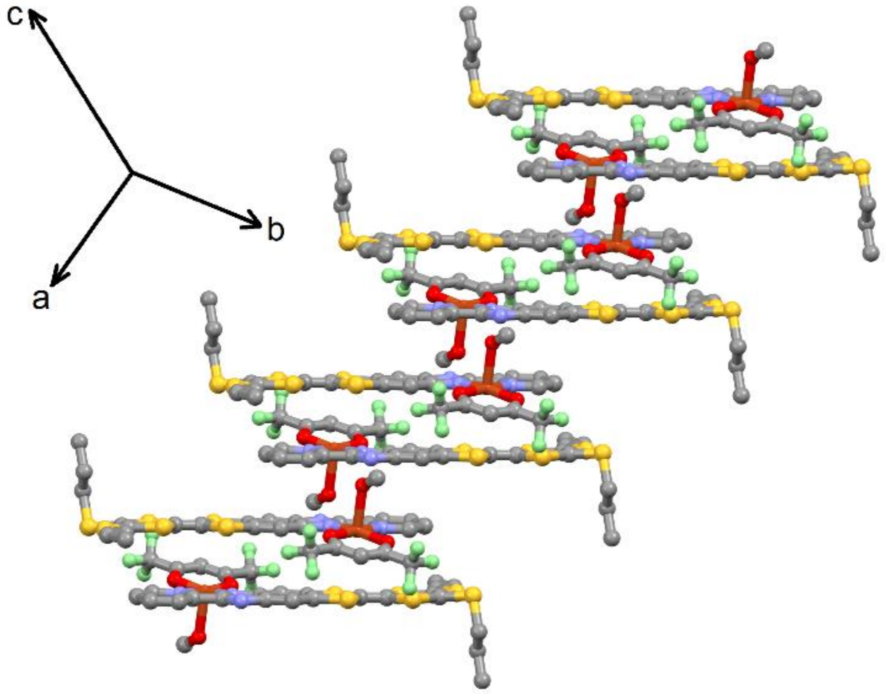

Figure S13. Crystal packing of **12** highlighting the formation of the columns along the *a* axis. In the crystal, the columns interact through the S1···S4 contacts (3.838 Å).

[Cu(H_2O)Dy(hfac)$_4$(L)]·[Dy(hfac)$_4$]·(CH_2Cl_2) (13). **13** crystallizes in the P-1 (N°2) triclinic space group (Table S1). The asymmetric unit is composed of one [Cu(H_2O)Dy(hfac)$_4$(**L**)]$^+$ cation, one [Dy(hfac)$_4$]$^-$ anion and one dichloromethane molecule of crystallization (Figure S14). The X-ray structure reveales that the dpp coordination site is occupied by the Dy(hfac)$_3$ precursor as expected. Nevertheless, it also revealed that the Cu(II) remains in an N_2O_3 square pyramidal environment even if the integrity of **L** is conserved. The axial position is now occupied by a water molecule instead of a MeOH molecule. Since such geometry leads to the loss of one hfac$^-$ anion to allow the coordination of the Cu(II) to the bischelating bzip coordination site and the Cu(II) is now coordinated to the imine nitrogen atoms of the imidazole (N1) and pyridine (N2) moieties, consequently the [Cu(H_2O)Dy(hfac)$_4$(**L**)]$^+$ fragment is cationic and so a [Dy(hfac)$_4$]$^-$ anion is formed to preserve the electro-neutrality of the complex.

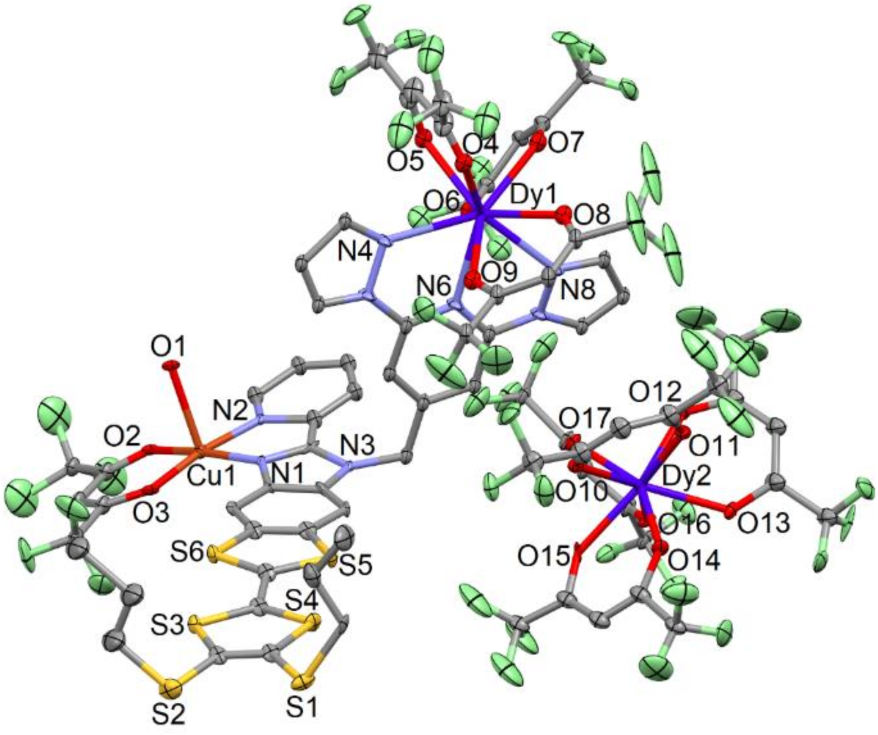

Figure S14. ORTEP view of **13**. Thermal ellipsoids are drawn at 30% probability. Hydrogen atoms and solvent molecules of crystallization are omitted for clarity.

The [Dy(hfac)$_4$]$^-$ anion strongly interacts with the axial water molecule with two identified H-bonds (O1···O13 = 2.780 Å and O1···O16 = 3.007 Å). Such proximity leads to a short intermolecular distance between Cu1 and Dy2 (6.001(4) Å) compared to the M-Ln intermolecular distances observed in the other compounds (Table S4). The α angle is also affected by the presence of the $[Dy(hfac)_4]^-$ anion with an almost orthogonality between the dpp and bzip fragments ($\alpha = 84.6(4)°$) (Table S6).

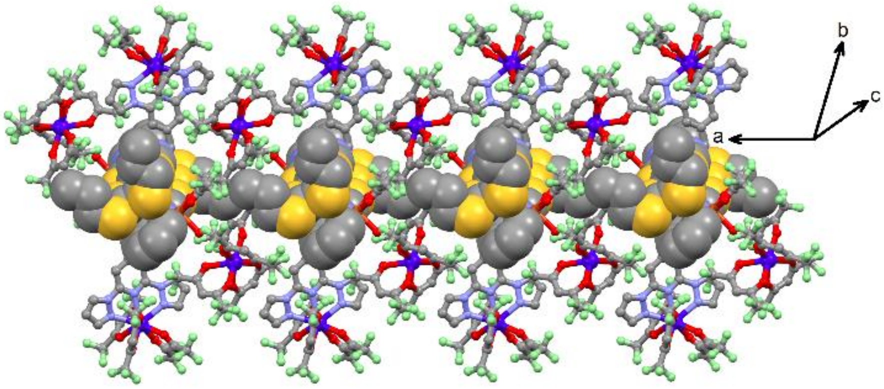

Figure S15. Crystal packing of **13**. The 4,5-[4,5-bis(propylthio)-tetrathiafulvalenyl]-1*H*-benzimidazol-2-yl}pyridine fragment is shown in spacefill representation while the dpp moiety, organometallic precursors $Cu(hfac)(H_2O)$ and $Dy(hfac)_3$, and $[Dy(hfac)_4]^-$ anion are shown in ball and sticks representation.

The crystal packing is also drastically changed with the formation of isolated head-to-tail dimers along the *a* axis and no S···S contacts are observed (Figure S15).

The shortest intramolecular Cu-Dy and intermolecular Dy-Dy are in the same range of distances than for compounds **1**-**11** (Table S4).

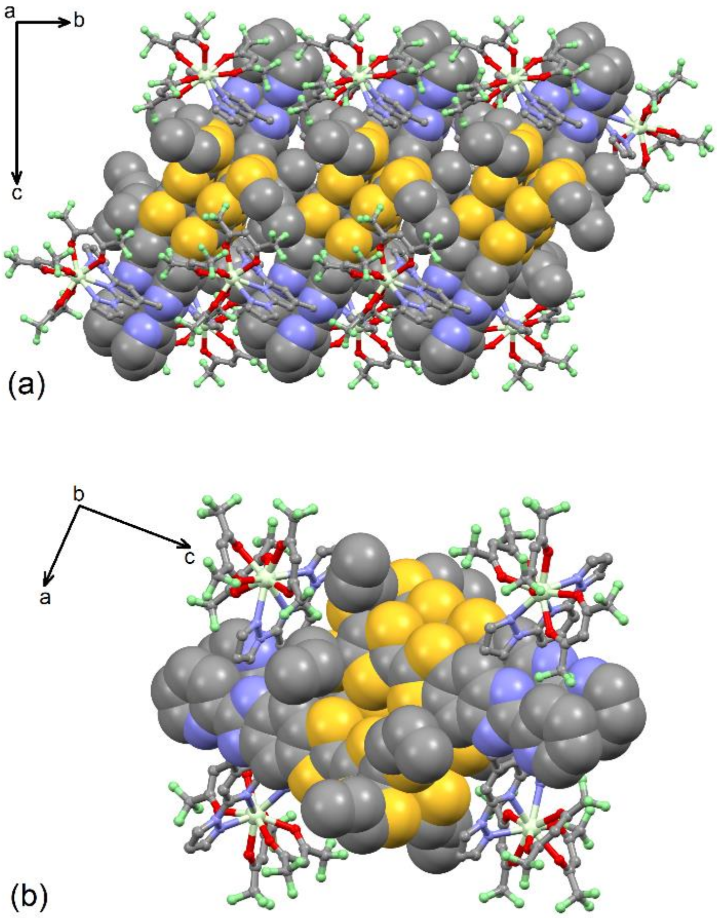

Figure S16. Crystal packing of **14**. The 4,5-[4,5-bis(propylthio)-tetrathiafulvalenyl]-1*H*-benzimidazol-2-yl}pyridine fragment is shown in spacefill representation while the dpp moiety and the organometallic precursors Pr(hfac)$_3$ are shown in ball and sticks representation.

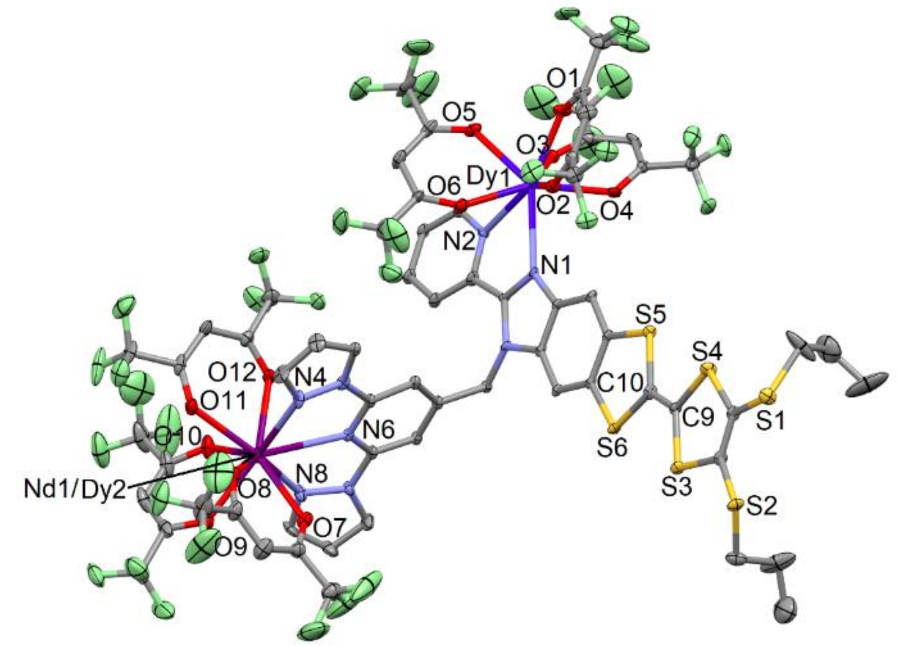

Figure S17. ORTEP view of **15**. Thermal ellipsoids are drawn at 30% probability. Hydrogen atoms and solvent molecules of crystallization are omitted for clarity.

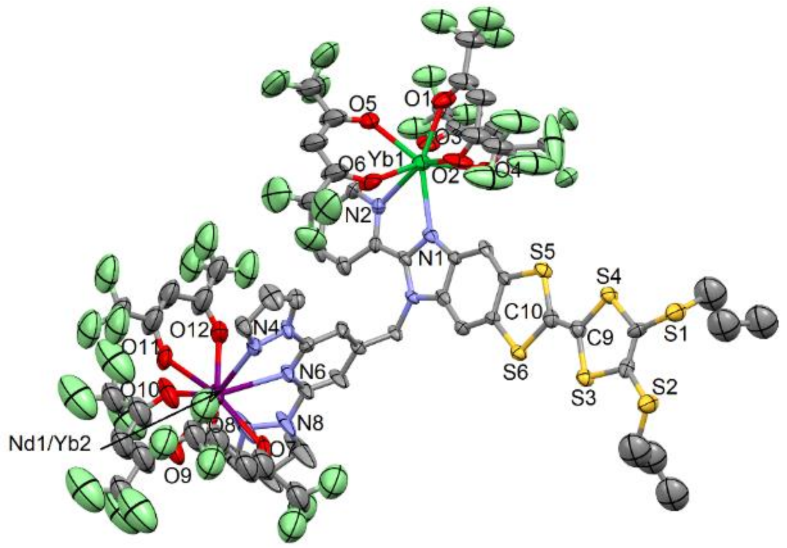

Figure S18. ORTEP view of **17**. Thermal ellipsoids are drawn at 30% probability. Hydrogen atoms and solvent molecules of crystallization are omitted for clarity.

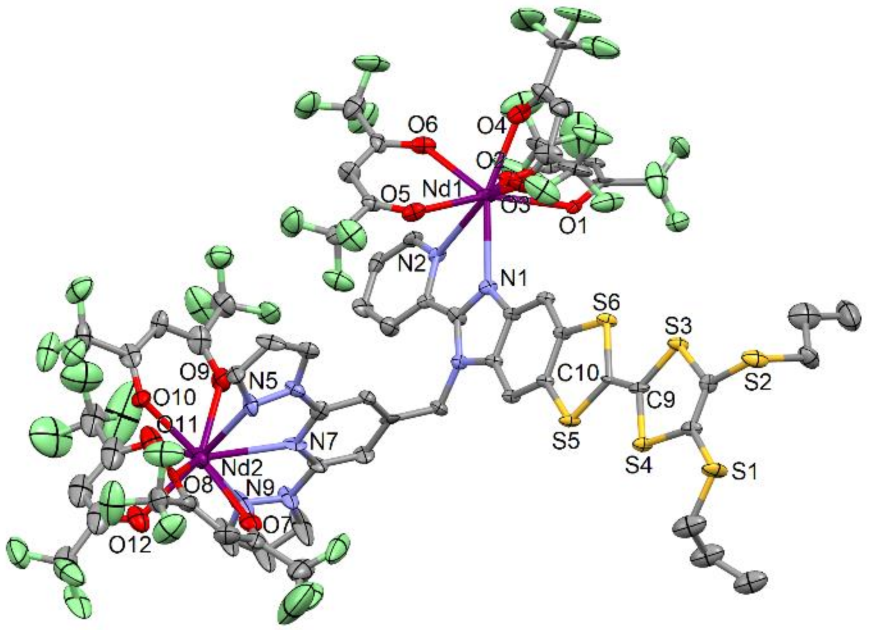

Figure S19. ORTEP view of **18**. Thermal ellipsoids are drawn at 30% probability. Hydrogen atoms and solvent molecules of crystallization are omitted for clarity.

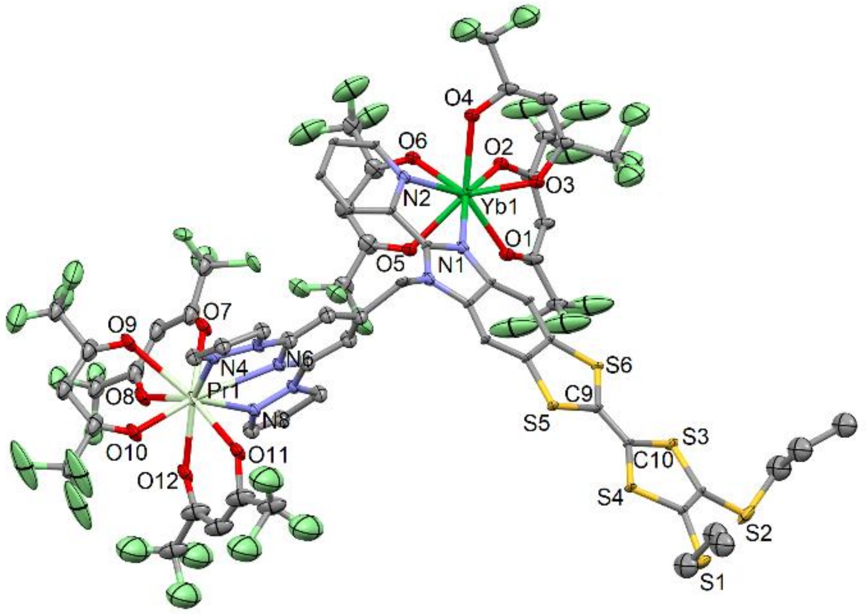

Figure S20. ORTEP view of **19**. Thermal ellipsoids are drawn at 30% probability. Hydrogen atoms and solvent molecules of crystallization are omitted for clarity.

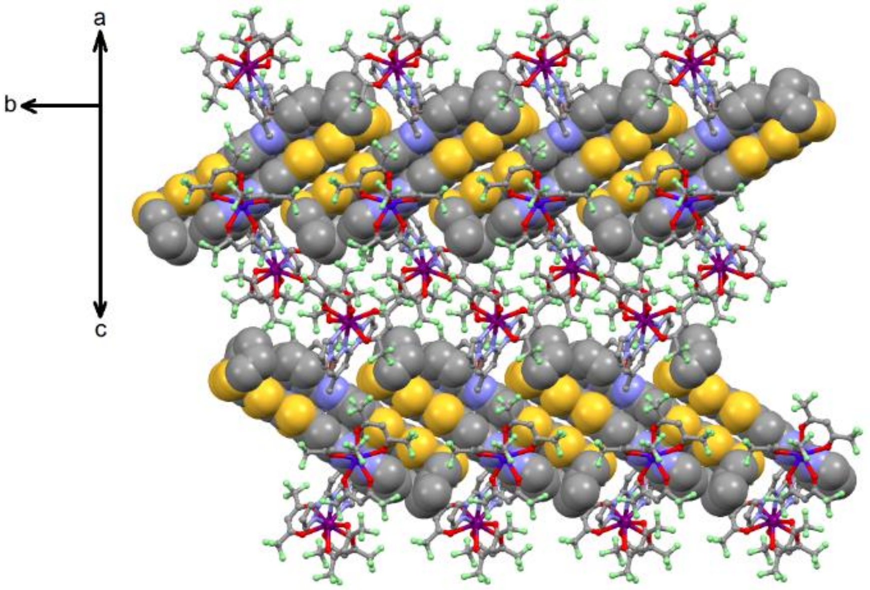

Figure S21. Representative crystal packing for compounds **15** and **17-19**. The 4,5-[4,5-bis(propylthio)-tetrathiafulvalenyl]-1*H*-benzimidazol-2-yl}pyridine fragment is shown in spacefill representation while the dpp moiety and the organometallic precursors Ln(hfac)$_3$ are shown in ball and sticks representation.

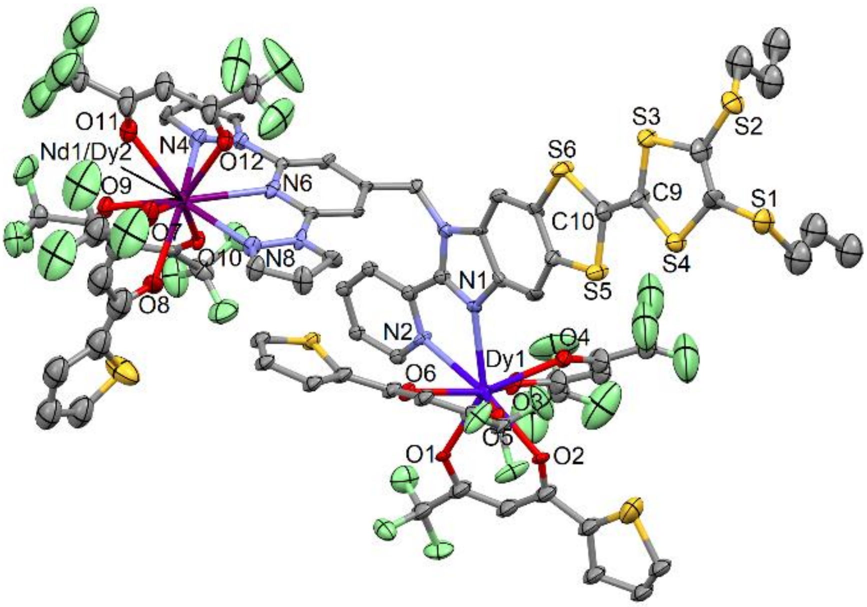

Figure S22. ORTEP view of **16**. Thermal ellipsoids are drawn at 30% probability. Hydrogen atoms and solvent molecules of crystallization are omitted for clarity.

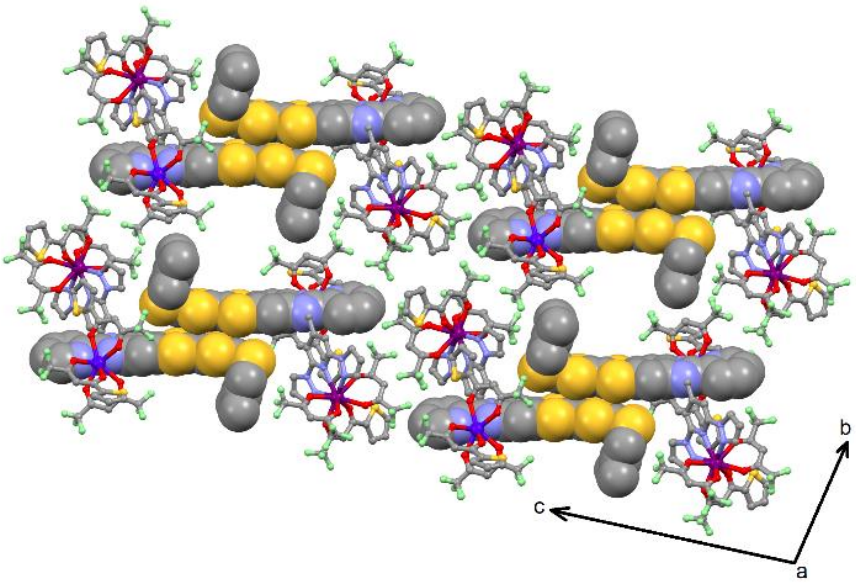

Figure S23. Crystal packing of **16**. The 4,5-[4,5-bis(propylthio)-tetrathiafulvalenyl]-1*H*-benzimidazol-2-yl}pyridine fragment is shown in spacefill representation while the dpp moiety and organometallic precursors Ln(hfac)$_3$ are shown in ball and sticks representation.

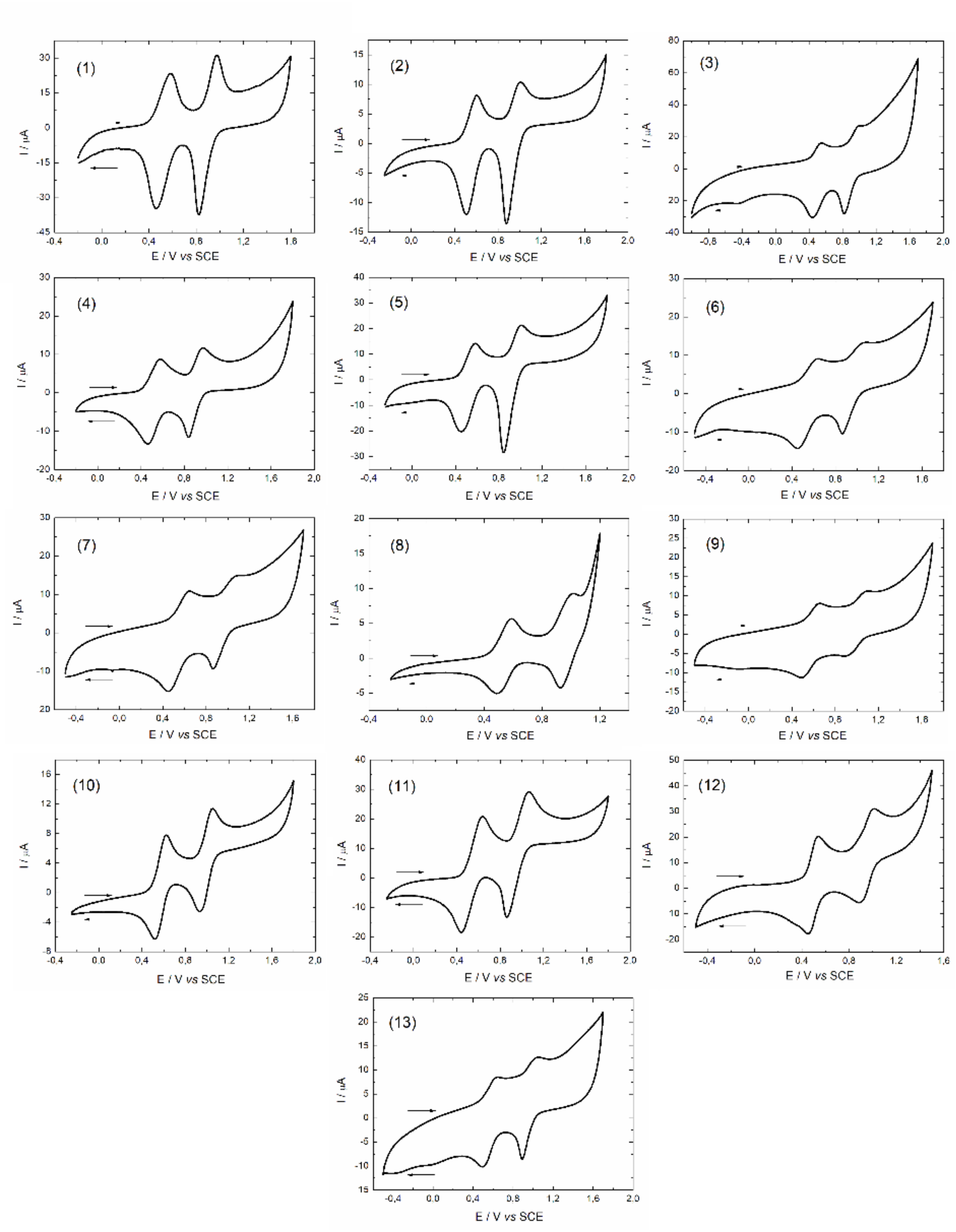

Figure S24. Cyclic voltammograms of **1-13** in CH_2Cl_2 at a scan rate of 100 $mV{\cdot}s^{-1}$. The potentials were measured *vs*. a saturated calomel electrode (SCE) with Pt wires as working and counter electrodes.

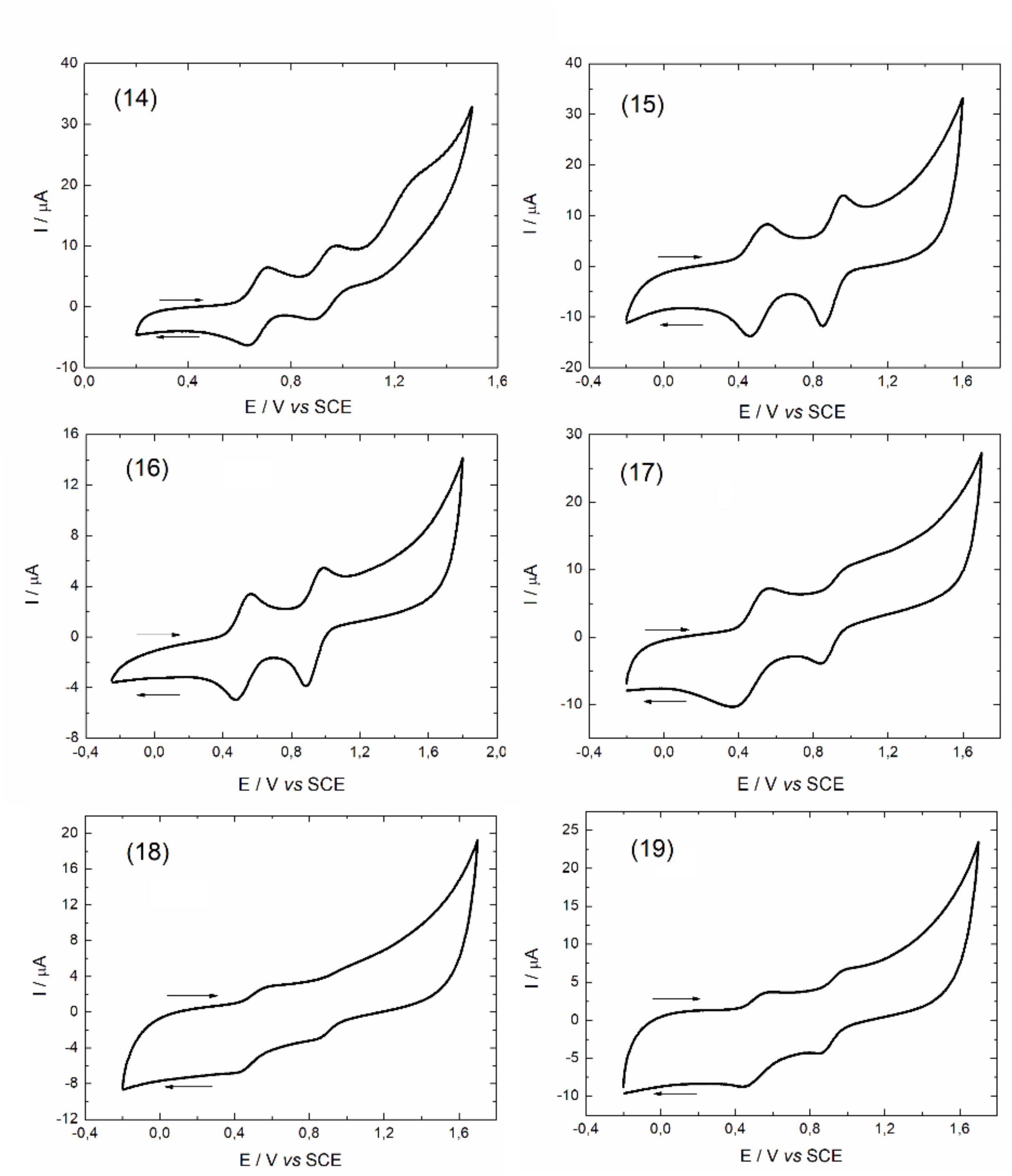

Figure S25. Cyclic voltammograms of **14-19** in CH_2Cl_2 at a scan rate of 100 $mV\cdot s^{-1}$. The potentials were measured *vs*. a saturated calomel electrode (SCE) with Pt wires as working and counter electrodes.

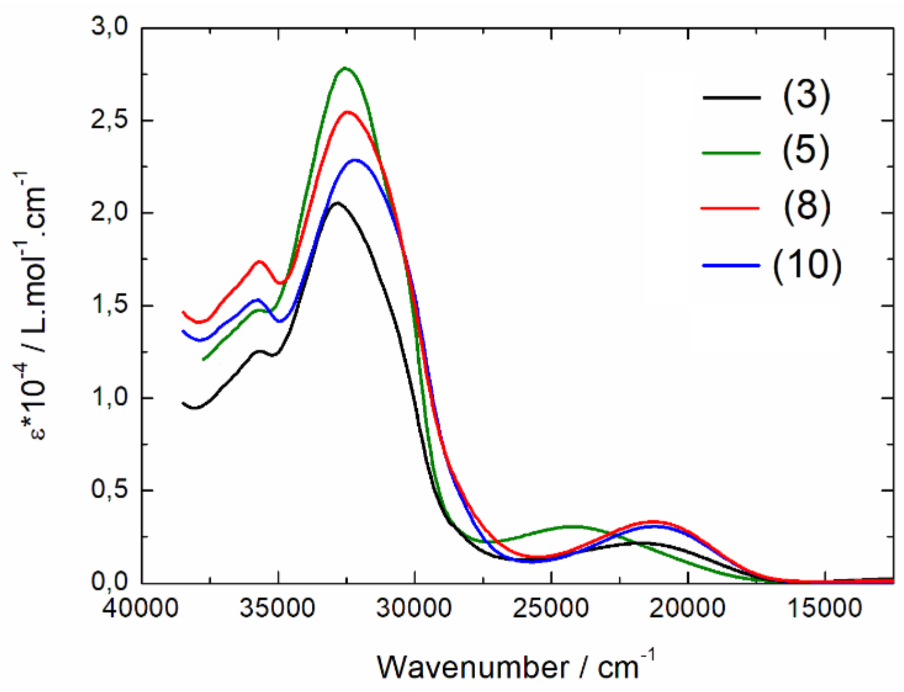

Figure S26. Experimental UV-vis absorption spectra of compounds **3**, **5**, **8** and **10** in CH_2Cl_2 solution.

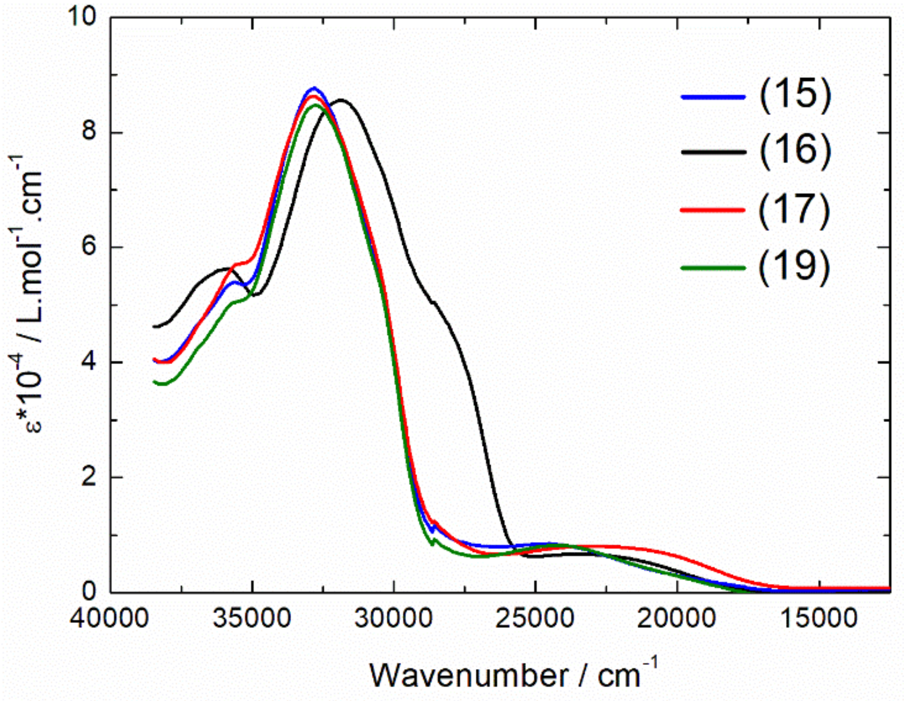

Figure S27. Experimental UV-vis absorption spectra of compounds **15-17** and **19** in CH_2Cl_2 solution.

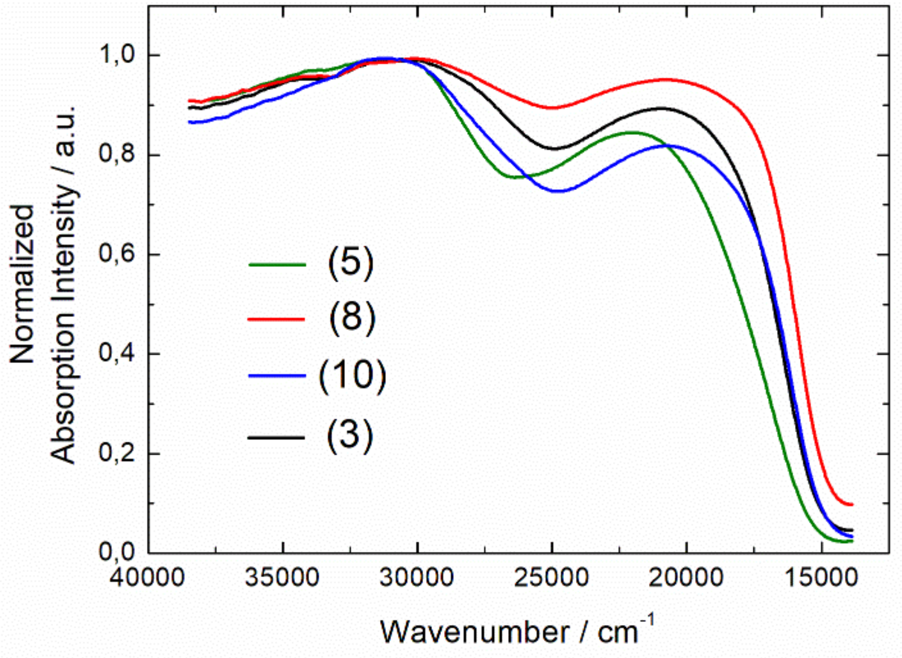

Figure S28. Experimental UV-vis absorption spectra in solid-state of compounds **3**, **5**, **8** and **10** in KBr pellets.

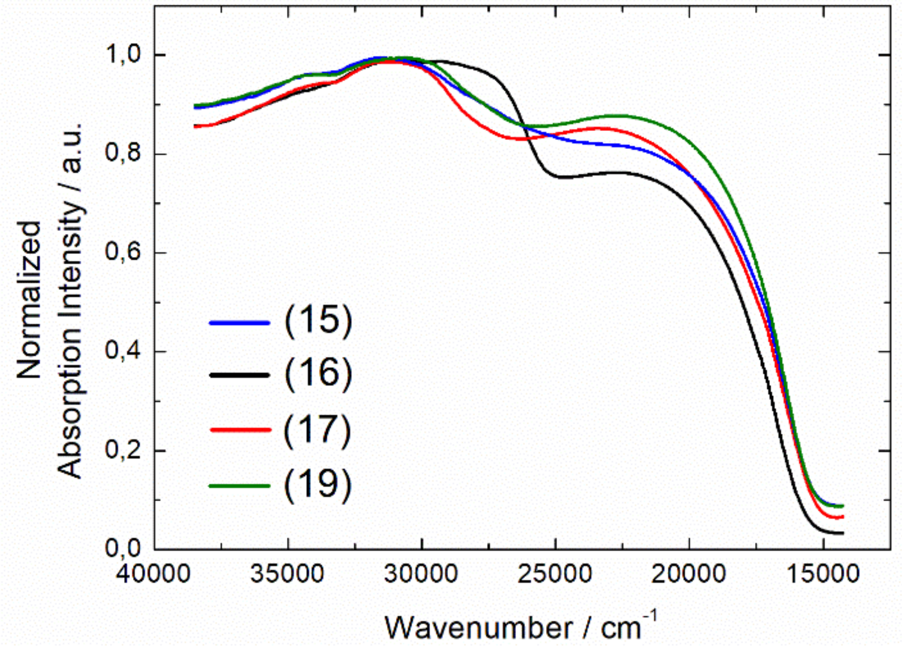

Figure S29. Experimental UV-vis absorption spectra in solid-state of compounds **15-17** and **19** in KBr pellets.

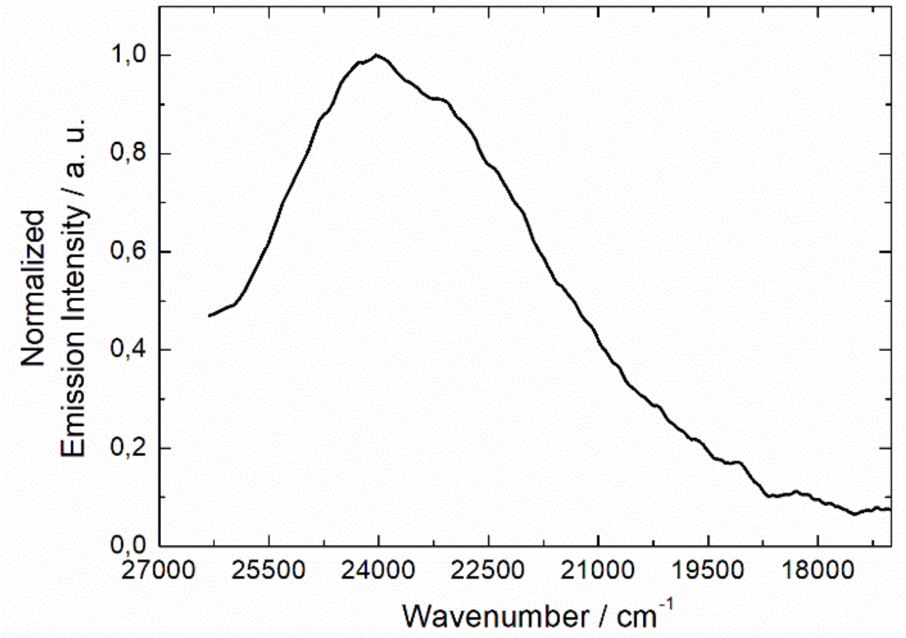

Figure S30. Visible (λ_{ex} = 350 nm) luminescence spectra of **3** in the solid state at room temperature.

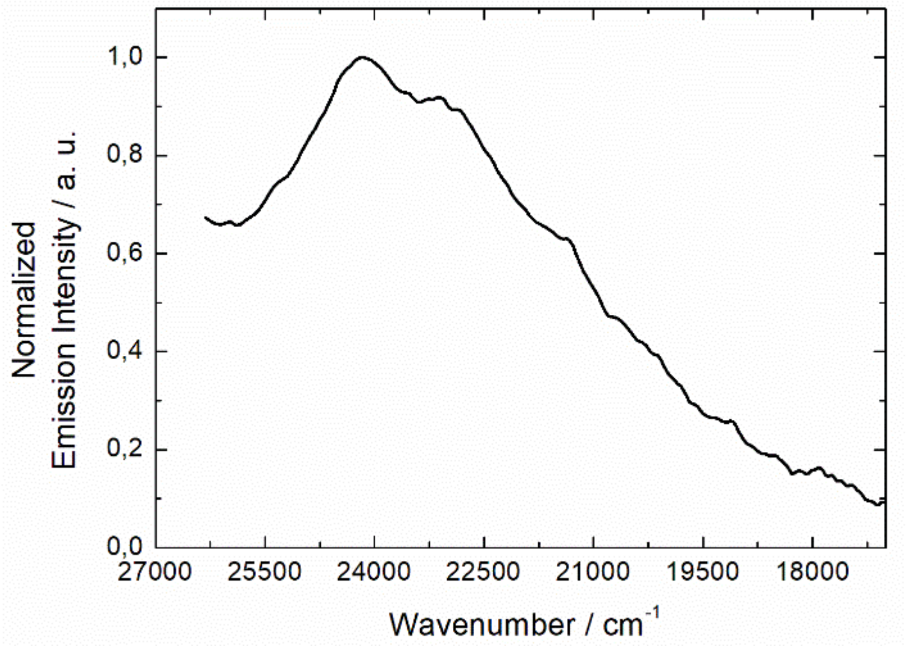

Figure S31. Visible (λ_{ex} = 350 nm) luminescence spectra of **5** in the solid state at room temperature.

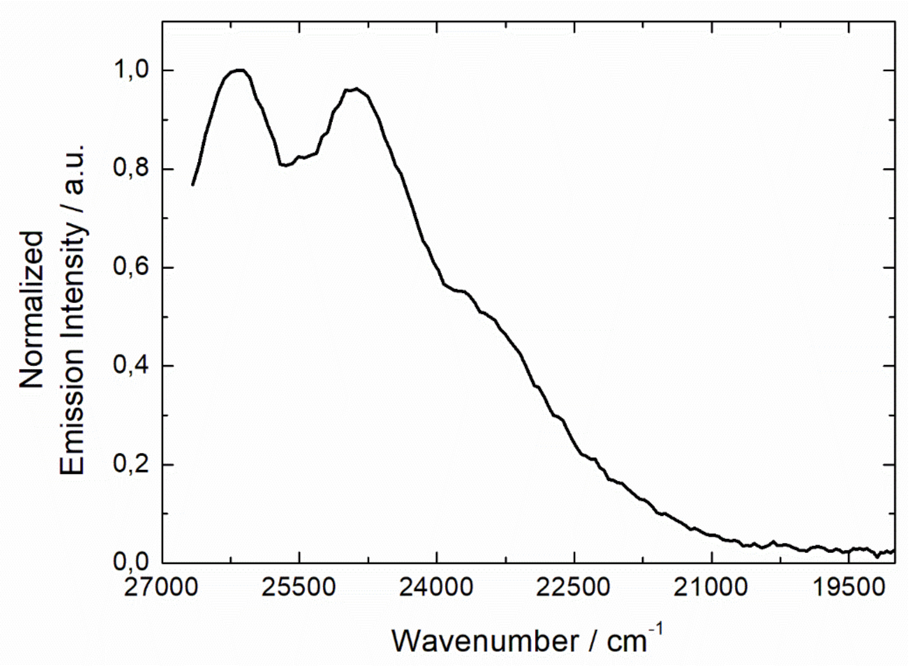

Figure S32. Visible (λ_{ex} = 350 nm) luminescence spectra of **8** in the solid state at room temperature.

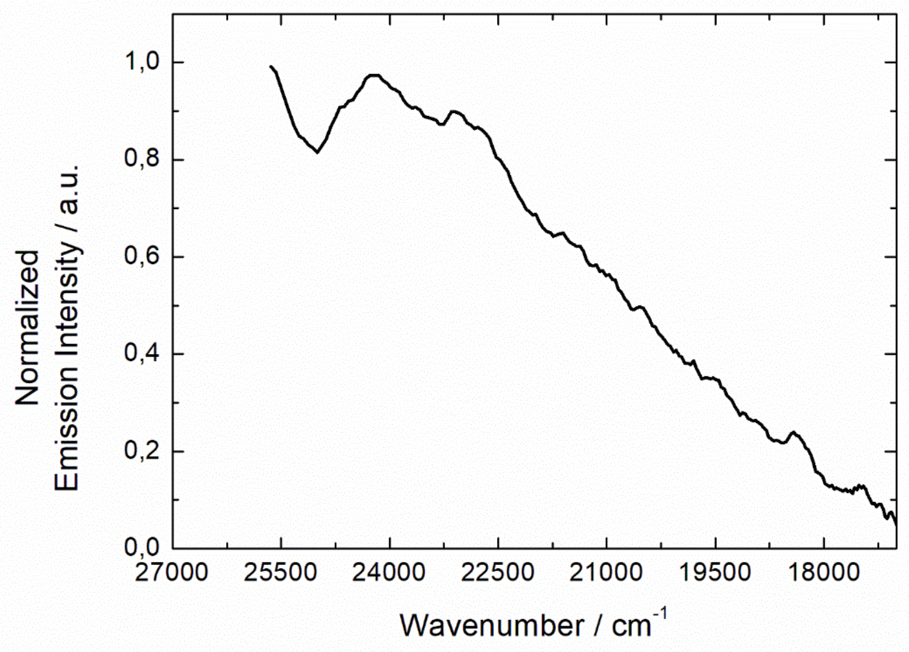

Figure S33. Visible (λ_{ex} = 350 nm) luminescence spectra of **10** in the solid state at room temperature.

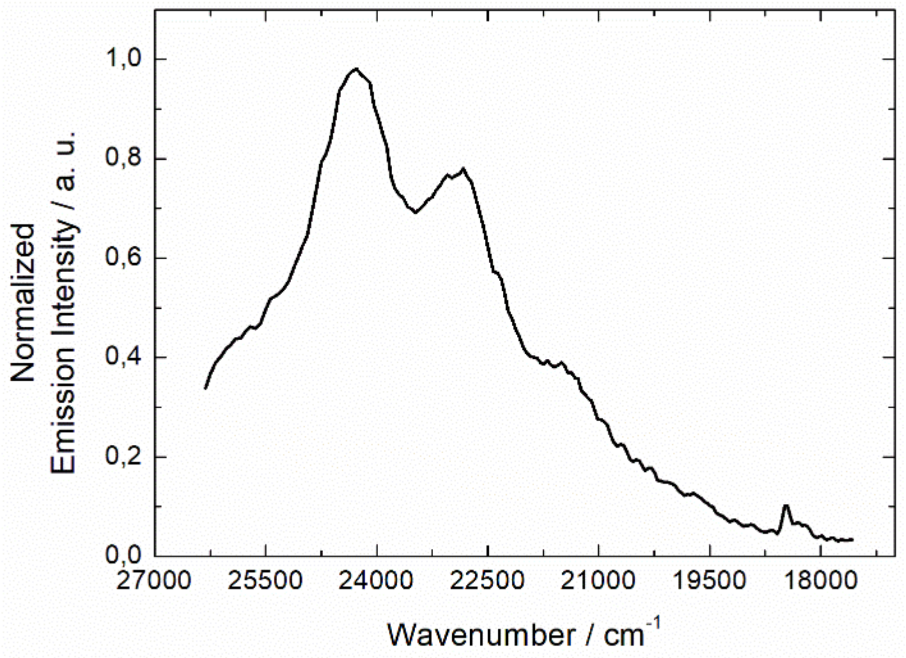

Figure S34. Visible (λ_{ex} = 350 nm) luminescence spectra of **3** in the solid state at 77 K.

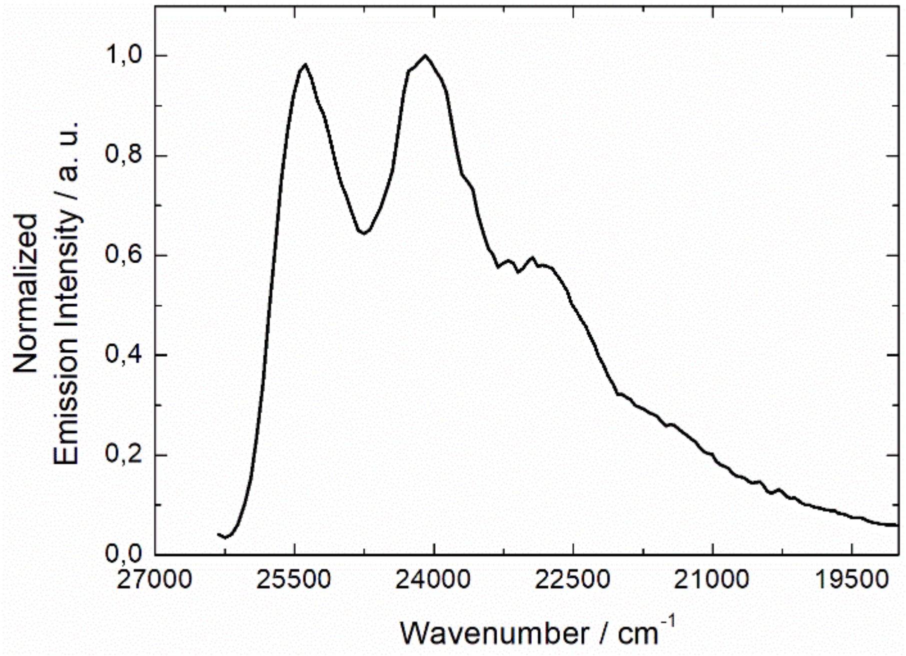

Figure S35. Visible (λ_{ex} = 350 nm) luminescence spectra of **5** in the solid state at 77 K.

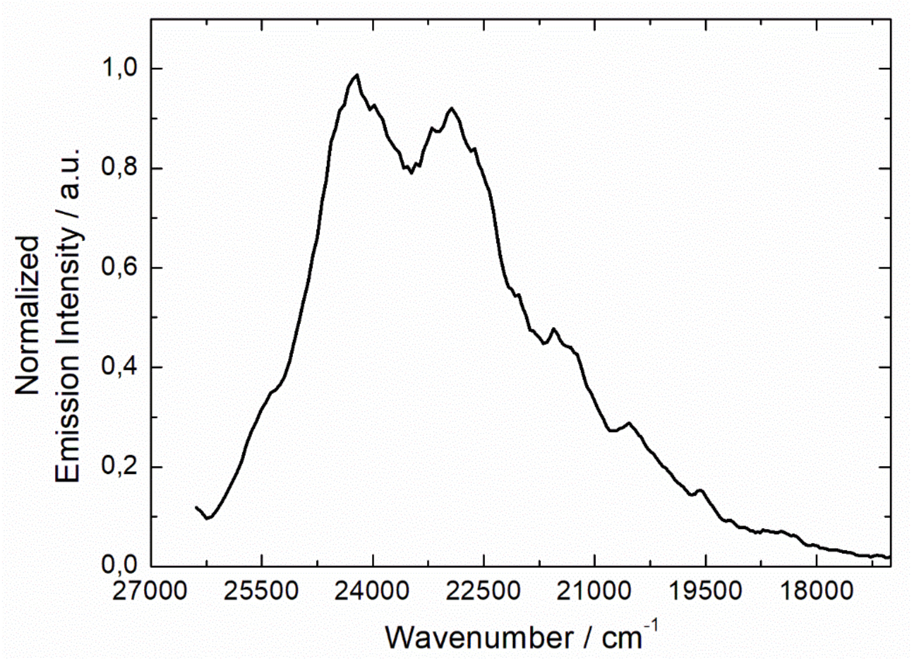

Figure S36. Visible (λ_{ex} = 350 nm) luminescence spectra of **8** in the solid state at 77 K.

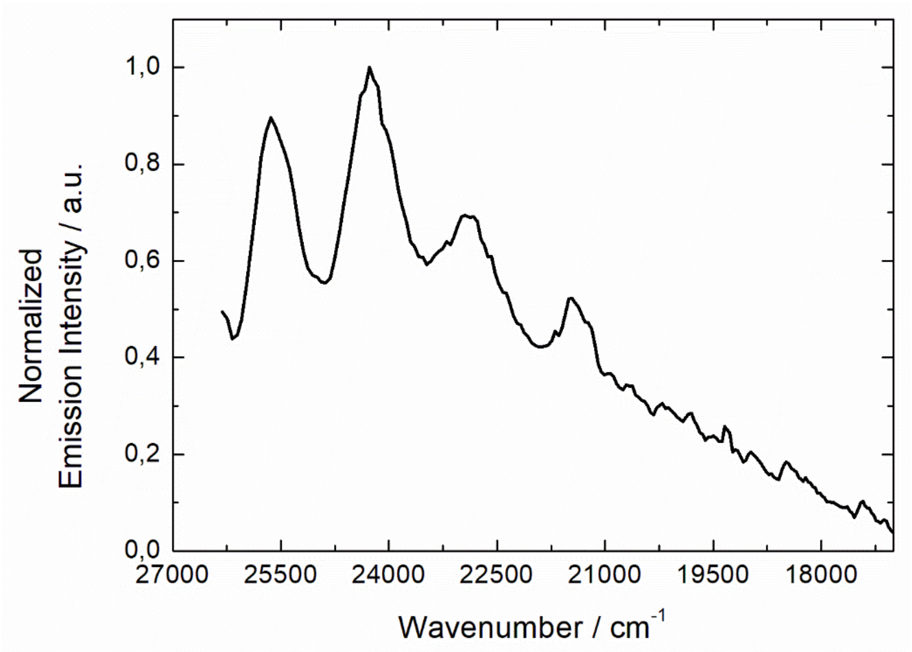

Figure S37. Visible (λ_{ex} = 350 nm) luminescence spectra of **10** in the solid state at 77 K.

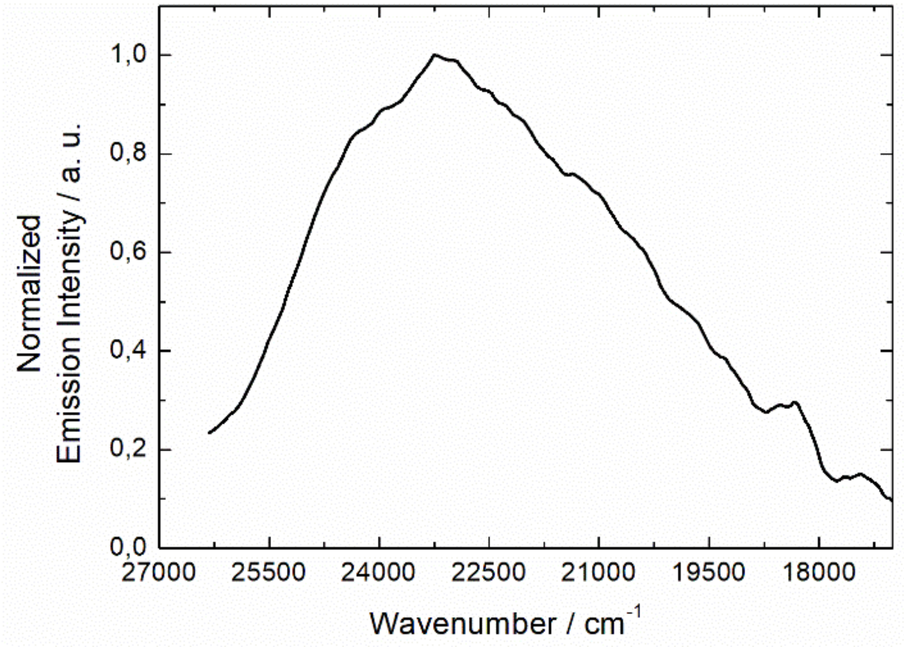

Figure S38. Visible (λ_{ex} = 350 nm) luminescence spectra of **15** in the solid state at room temperature.

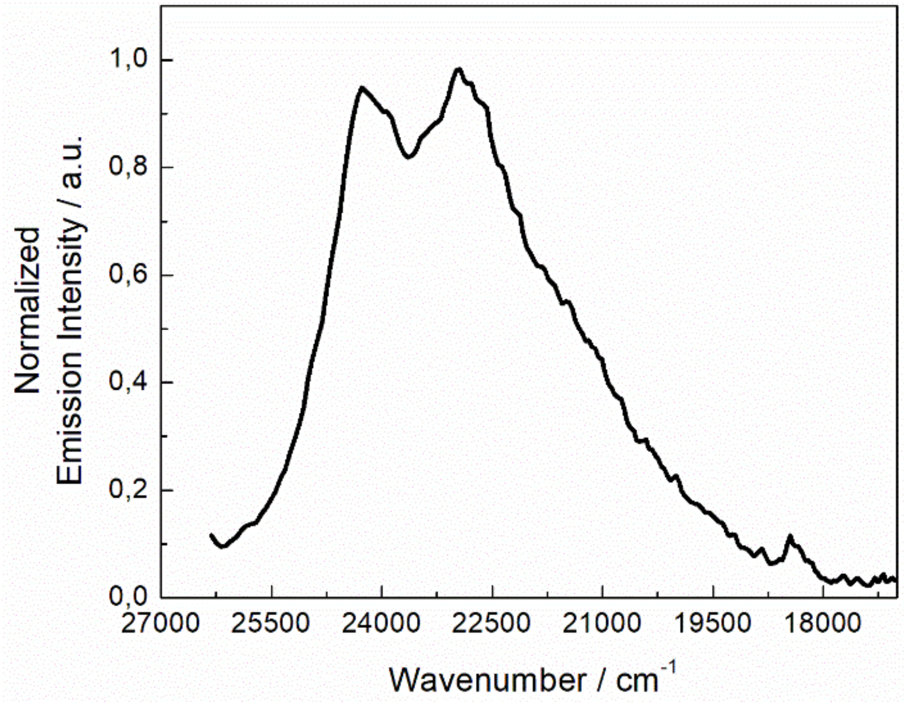

Figure S39. Visible (λ_{ex} = 350 nm) luminescence spectra of **17** in the solid state at room temperature.

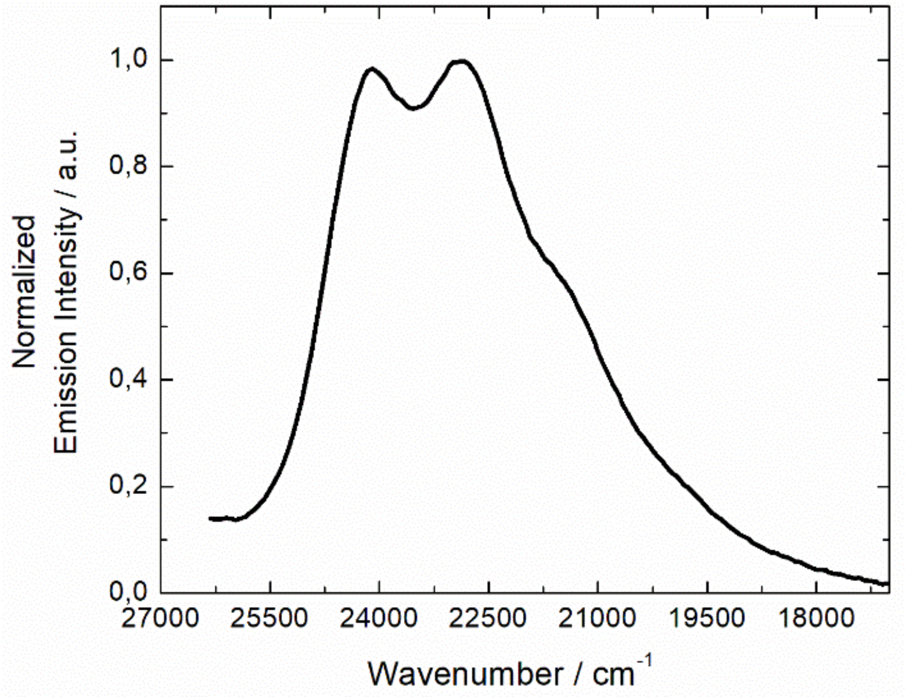

Figure S40. Visible (λ_{ex} = 350 nm) luminescence spectra of **19** in the solid state at room temperature.

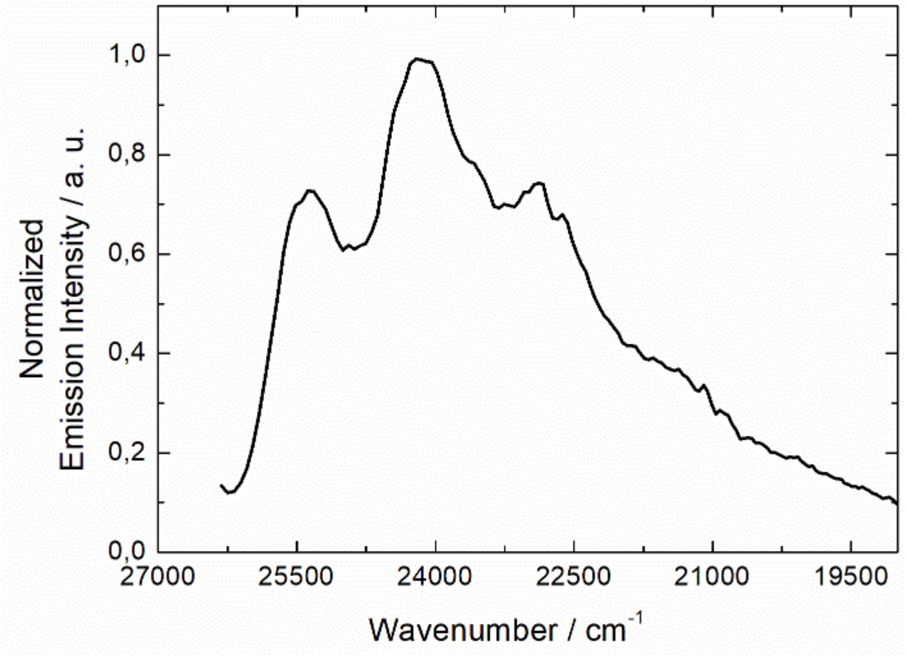

Figure S41. Visible (λ_{ex} = 350 nm) luminescence spectra of **15** in the solid state at 77 K.

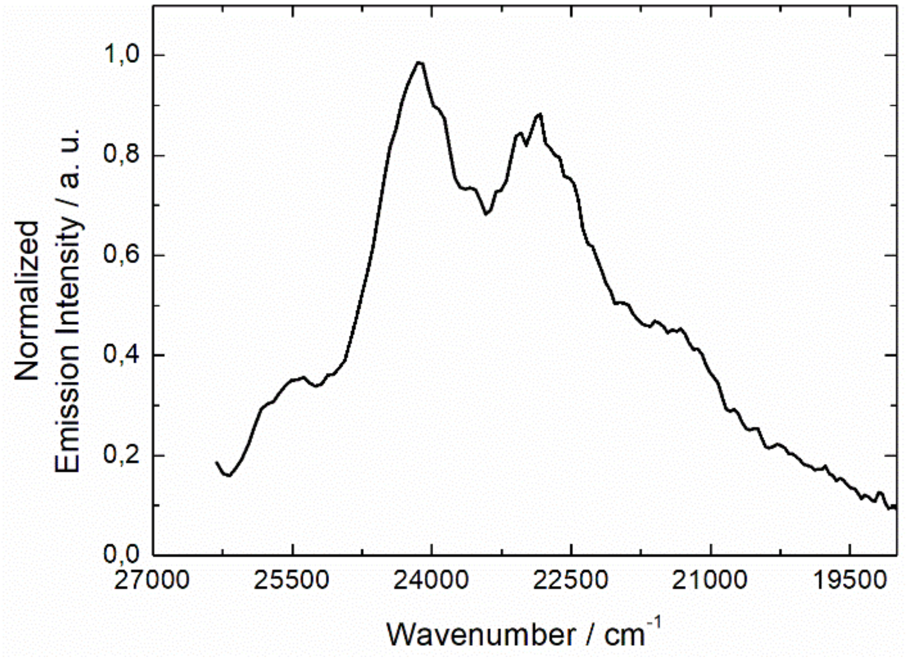

Figure S42. Visible (λ_{ex} = 350 nm) luminescence spectra of **17** in the solid state at 77 K.

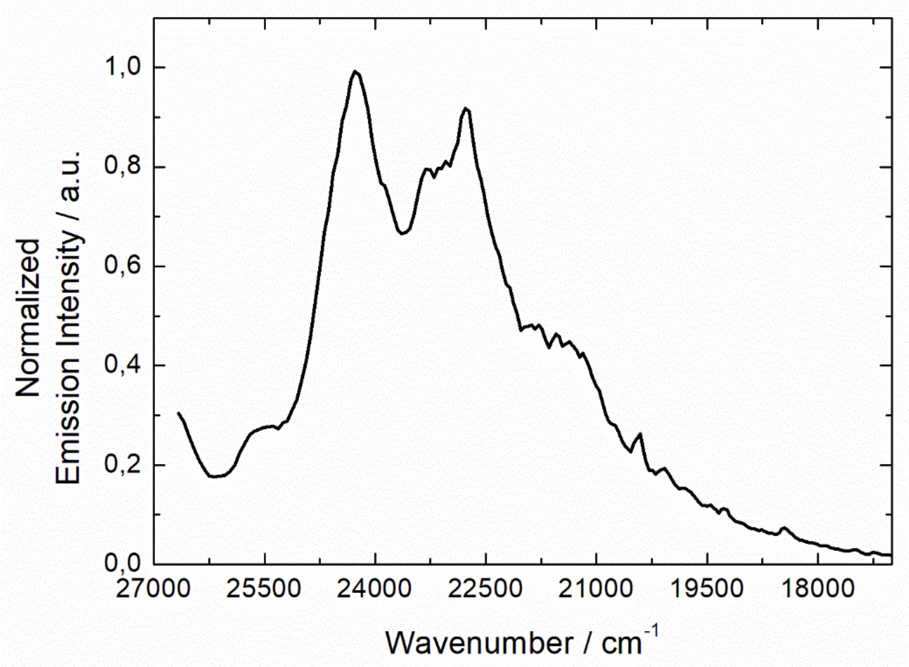

Figure S43. Visible (λ_{ex} = 350 nm) luminescence spectra of **19** in the solid state at room temperature.

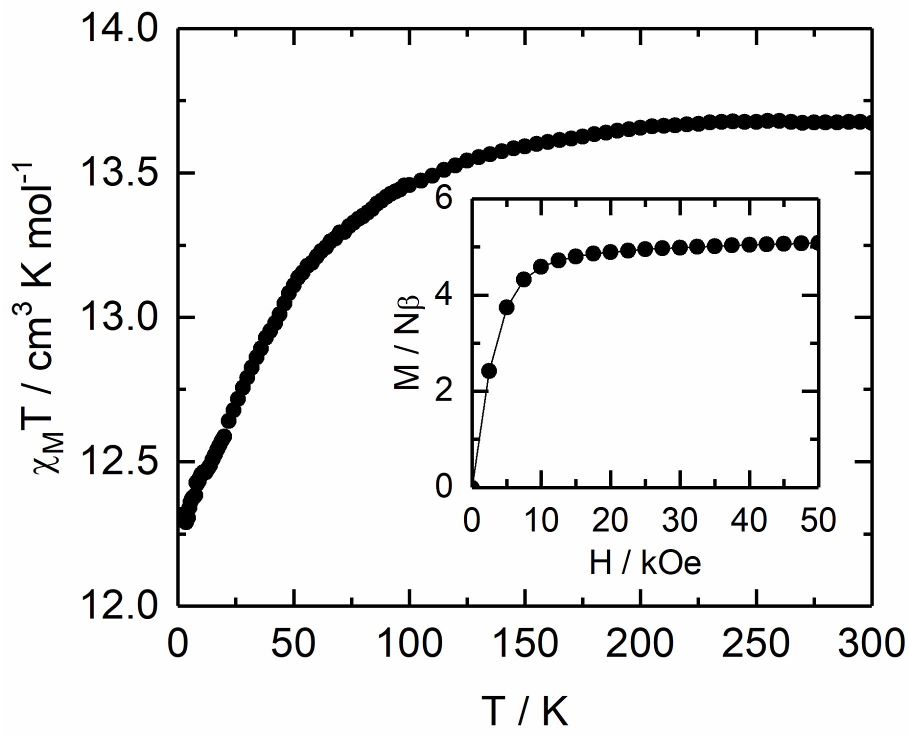

Figure S44. Thermal variation of χ_MT for **1**. Inset: field variation of the magnetization of **1** at 2 K.

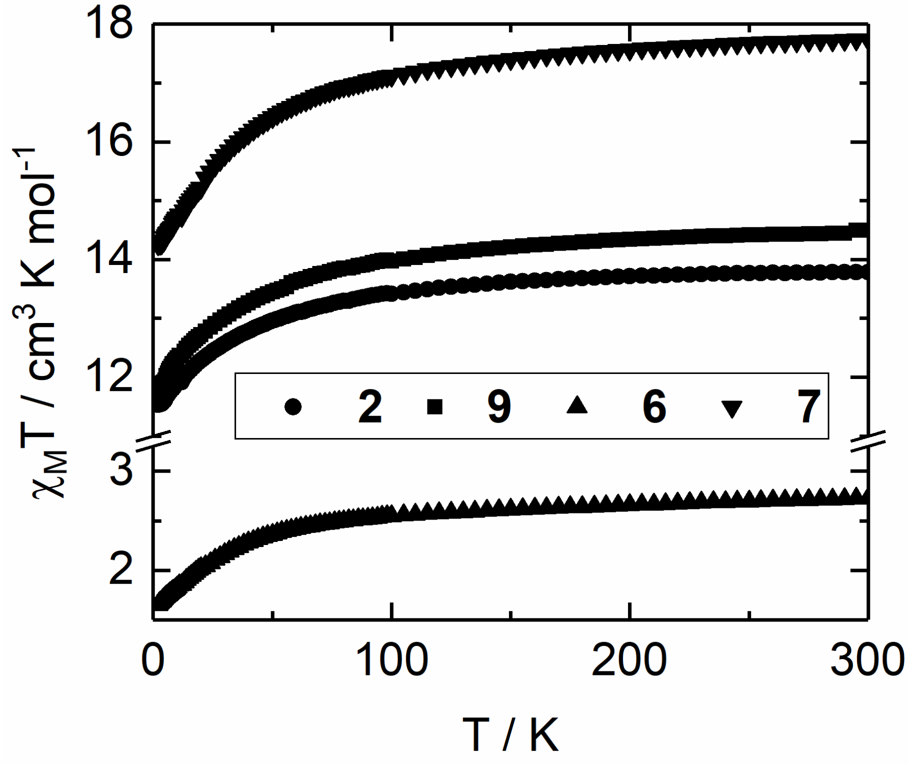

Figure S45. Thermal variation of χ_MT for **2**, **6**, **7** and **9**.

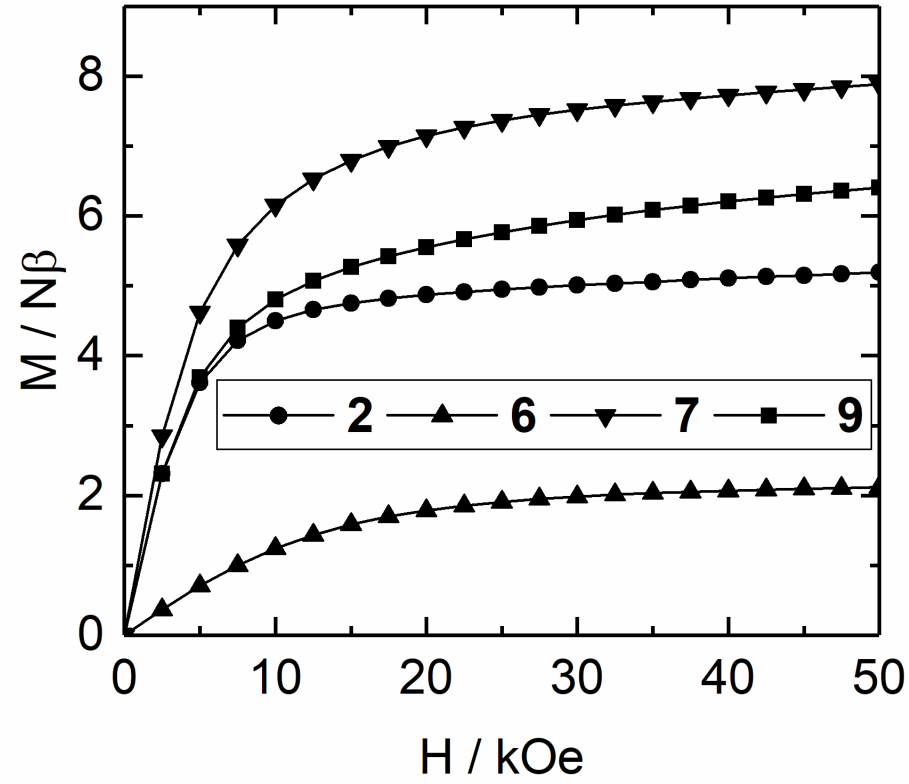

Figure S46. Magnetization curves at 2 K for **2**, **6**, **7** and **9**.

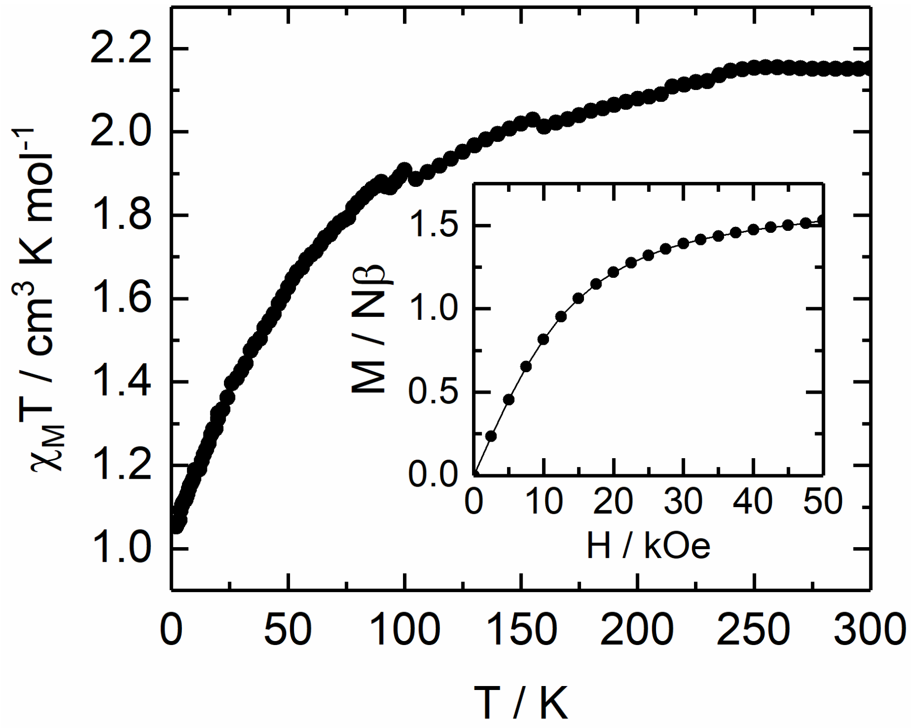

Figure S47. Temperature variation of $\chi_M T$ for **3** with the field variation of the magnetization recorded at 2 K.

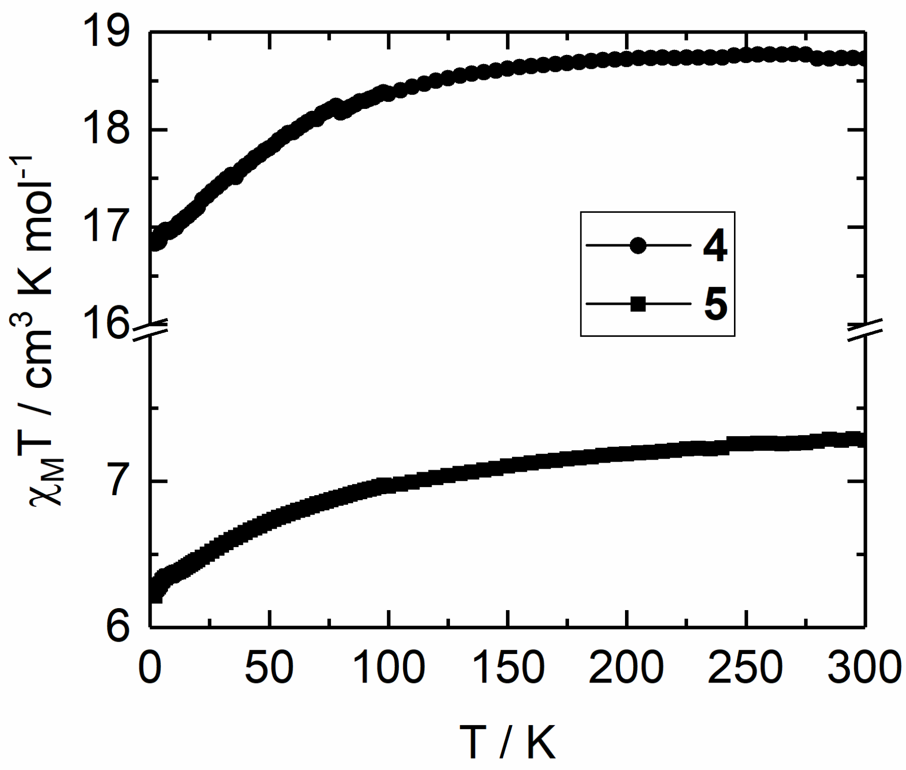

Figure S48. Thermal variation of χ_MT for **4** and **5**.

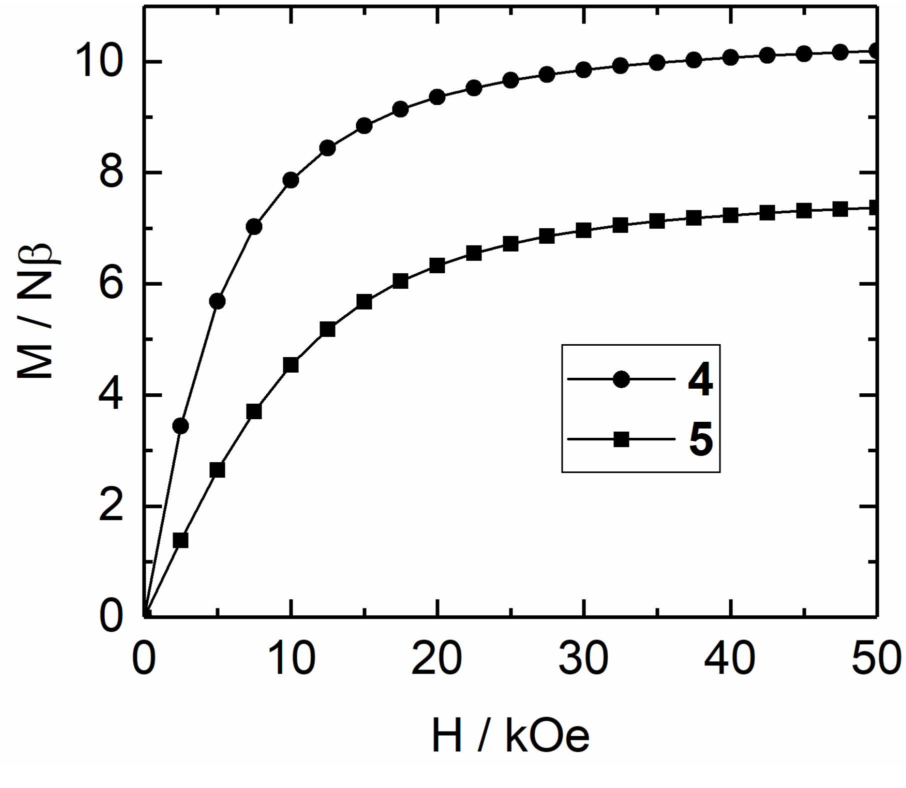

Figure S49. Magnetization curves at 2 K for **4** and **5**.

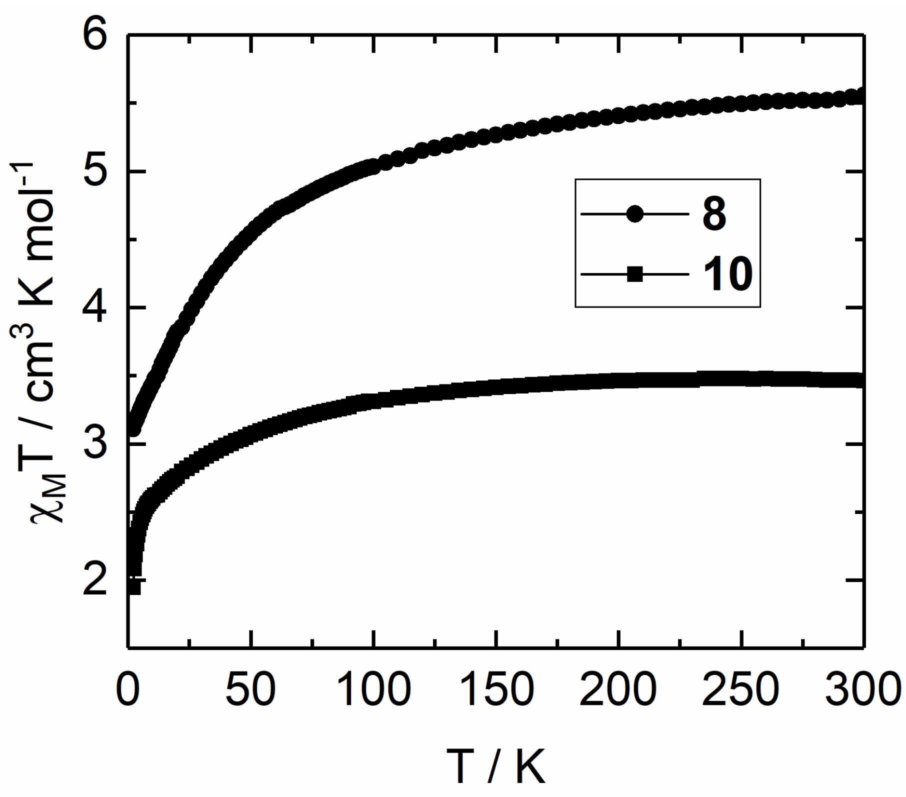

Figure S50. Thermal variation of χ_MT for **8** and **10**.

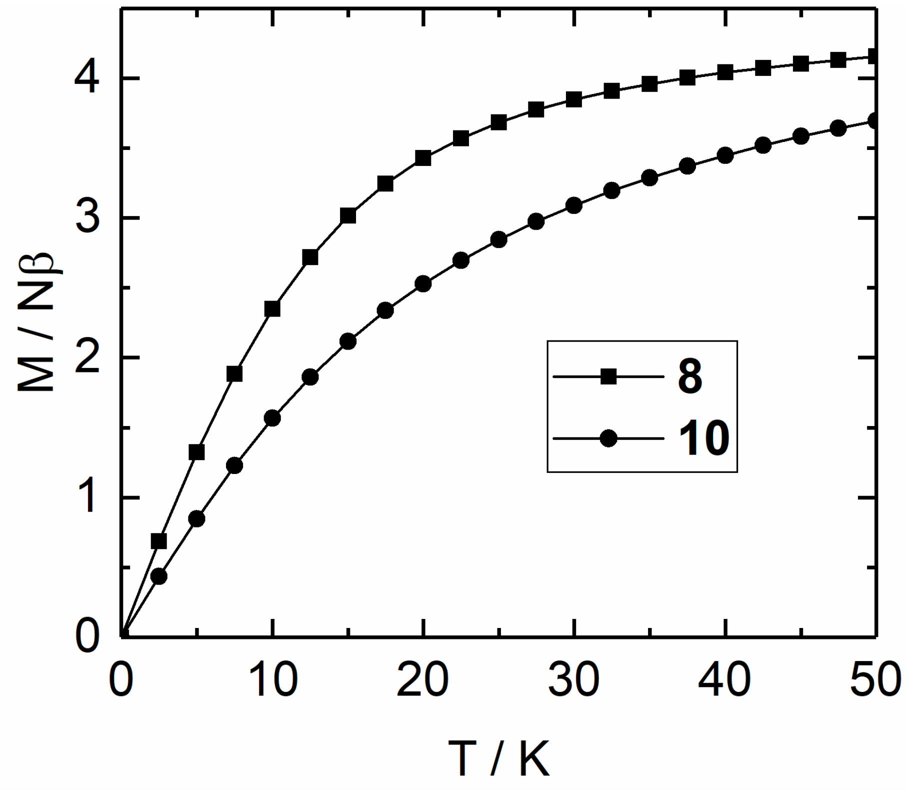

Figure S51. Magnetization curves at 2 K for **8** and **10**.

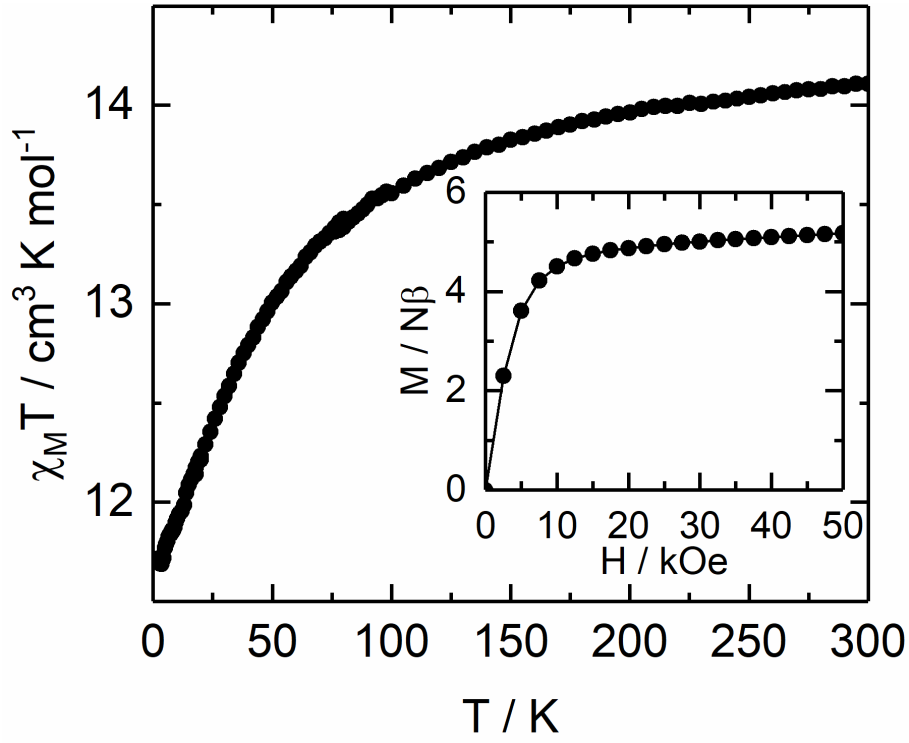

Figure S52. Thermal variation of $\chi_M T$ for **11** with the magnetization curve at 2 K in inset.

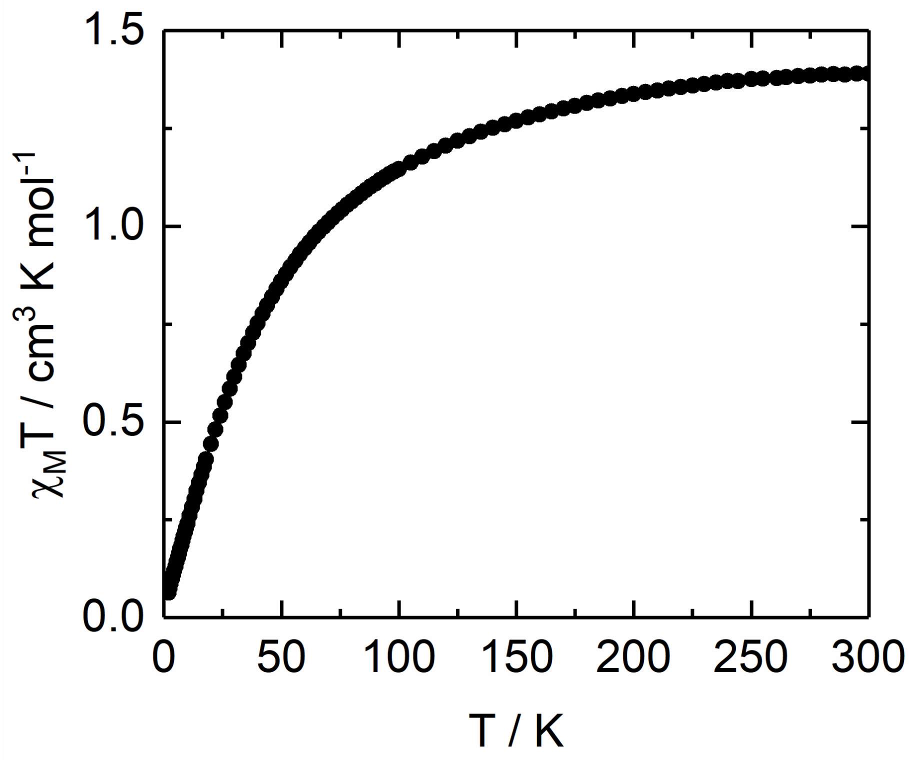

Figure S53. Thermal variation of $\chi_M T$ for **14**.

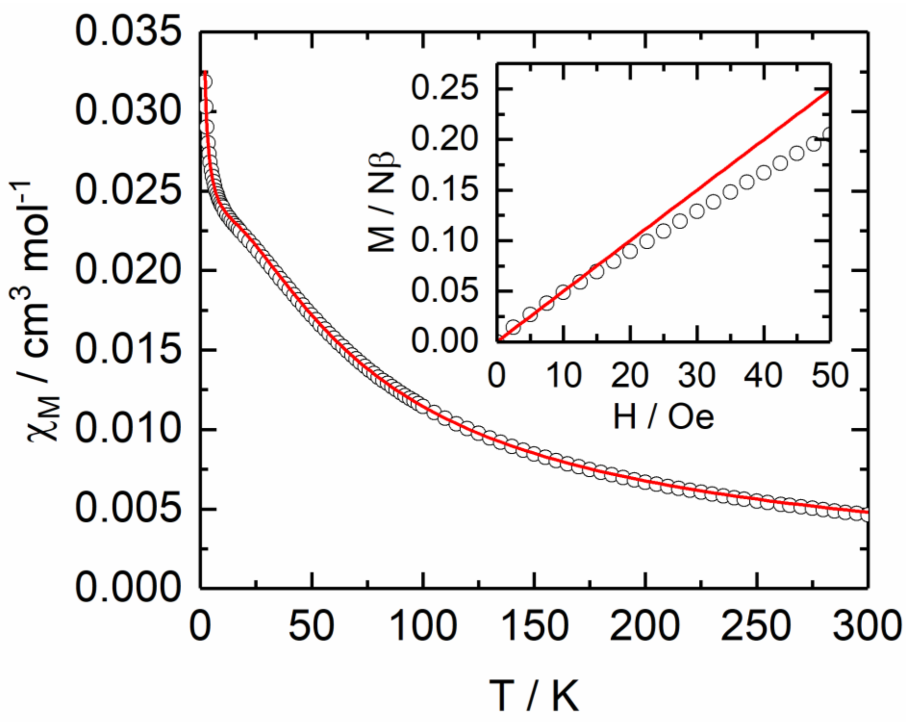

Figure S54. Thermal variation of χ_M for **14** with the magnetization curve at 2 K in inset. The red line corresponds to the best fitted curve for χ_M vs. T (see main text).

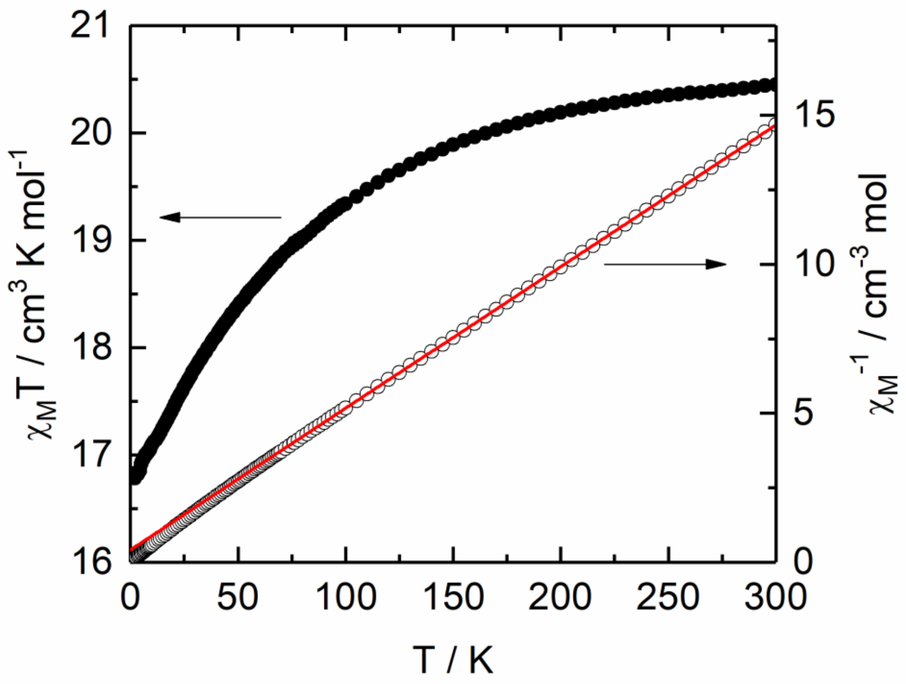

Figure S55. Thermal variation of χ_MT and χ_M^{-1} for **15**. The red line corresponds to the best fitted curve for χ_M^{-1} vs. T with Curie-Weiss law (see main text).

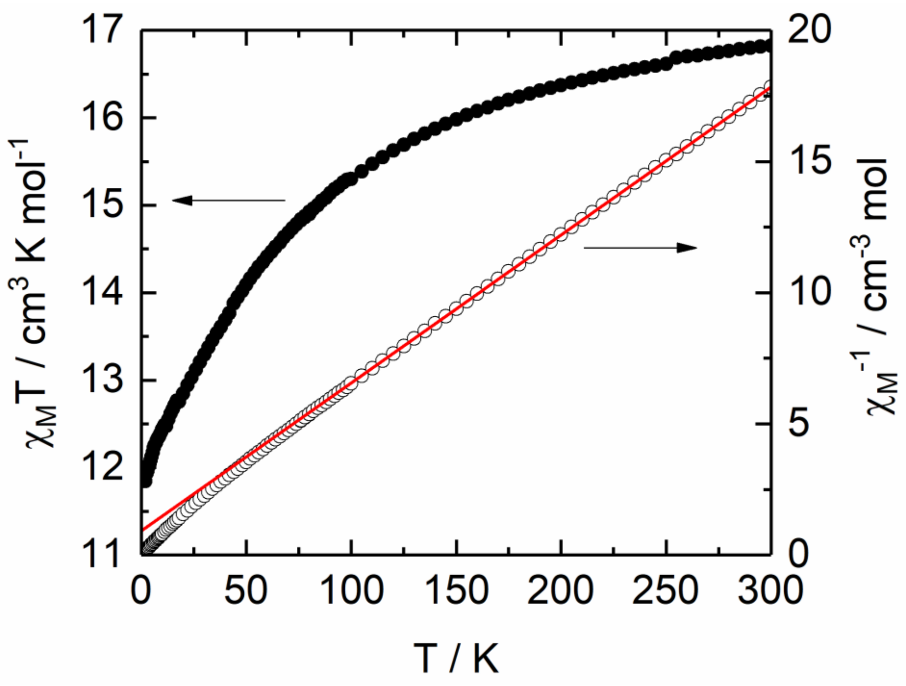

Figure S56. Thermal variation of $\chi_M T$ and χ_M^{-1} for **16**. The red line corresponds to the best fitted curve for χ_M^{-1} vs. T with Curie-Weiss law (see main text).

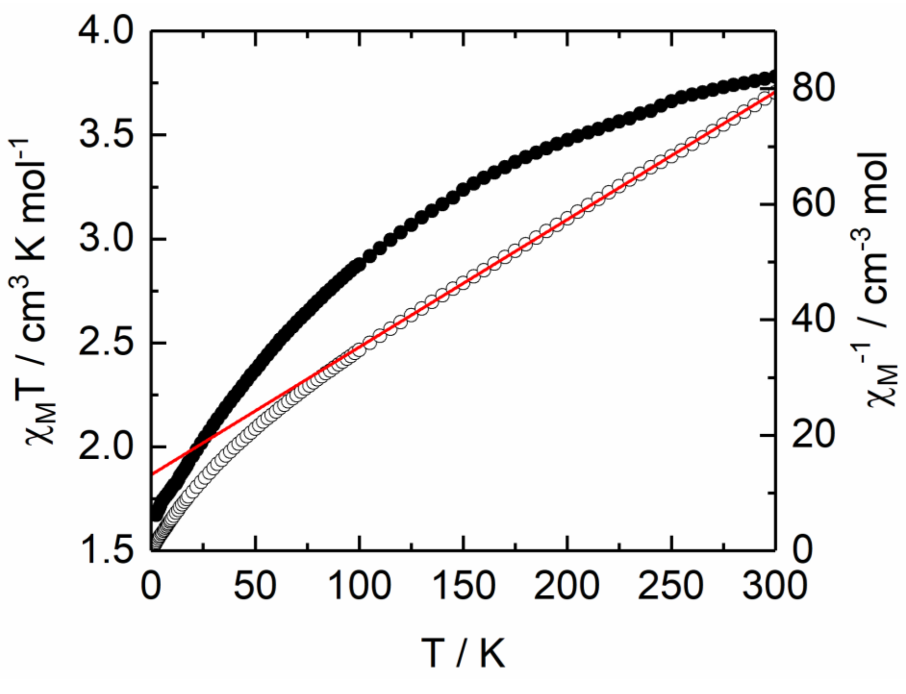

Figure S57. Thermal variation of $\chi_M T$ and χ_M^{-1} for **17**. The red line corresponds to the best fitted curve for χ_M^{-1} vs. T with Curie-Weiss law (see main text).

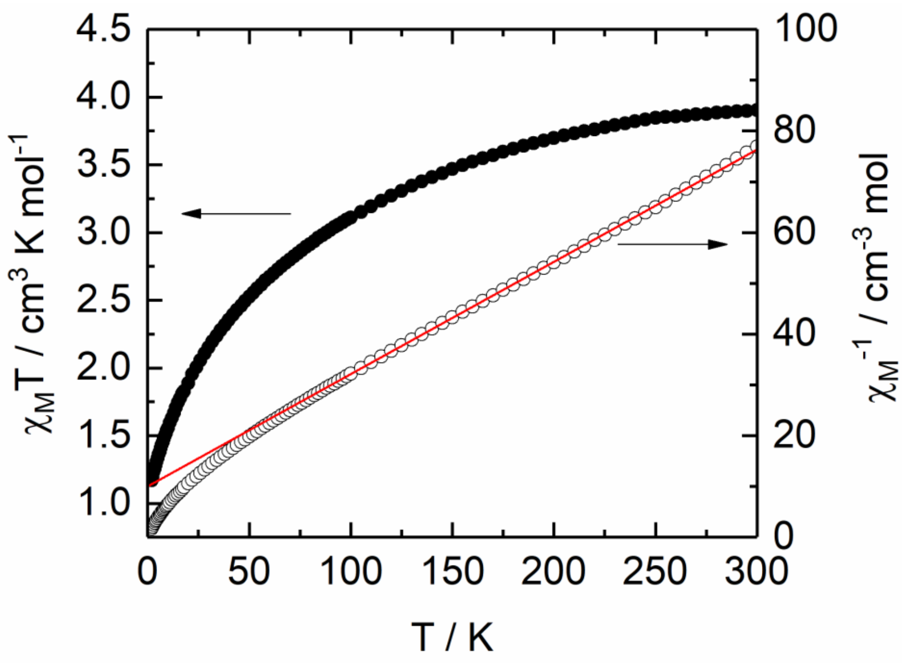

Figure S58. Thermal variation of $\chi_M T$ and χ_M^{-1} for **19**. The red line corresponds to the best fitted curve for χ_M^{-1} vs. T with Curie-Weiss law (see main text).

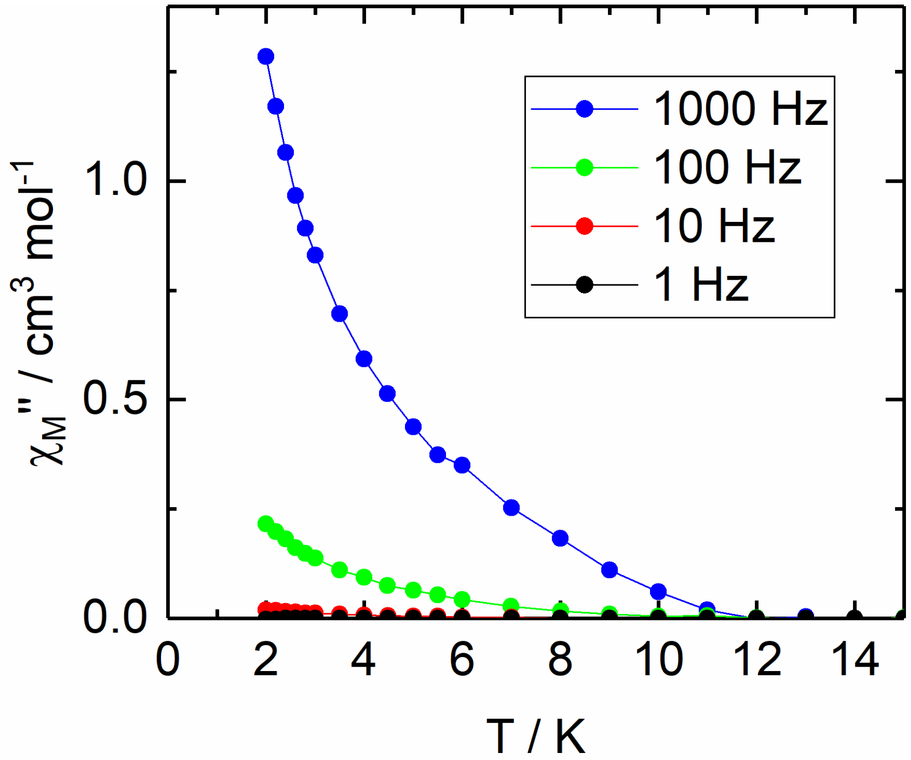

Figure S59. Thermal variation of χ_M'' in zero external dc field for **1** at various frequencies of the oscillating field.

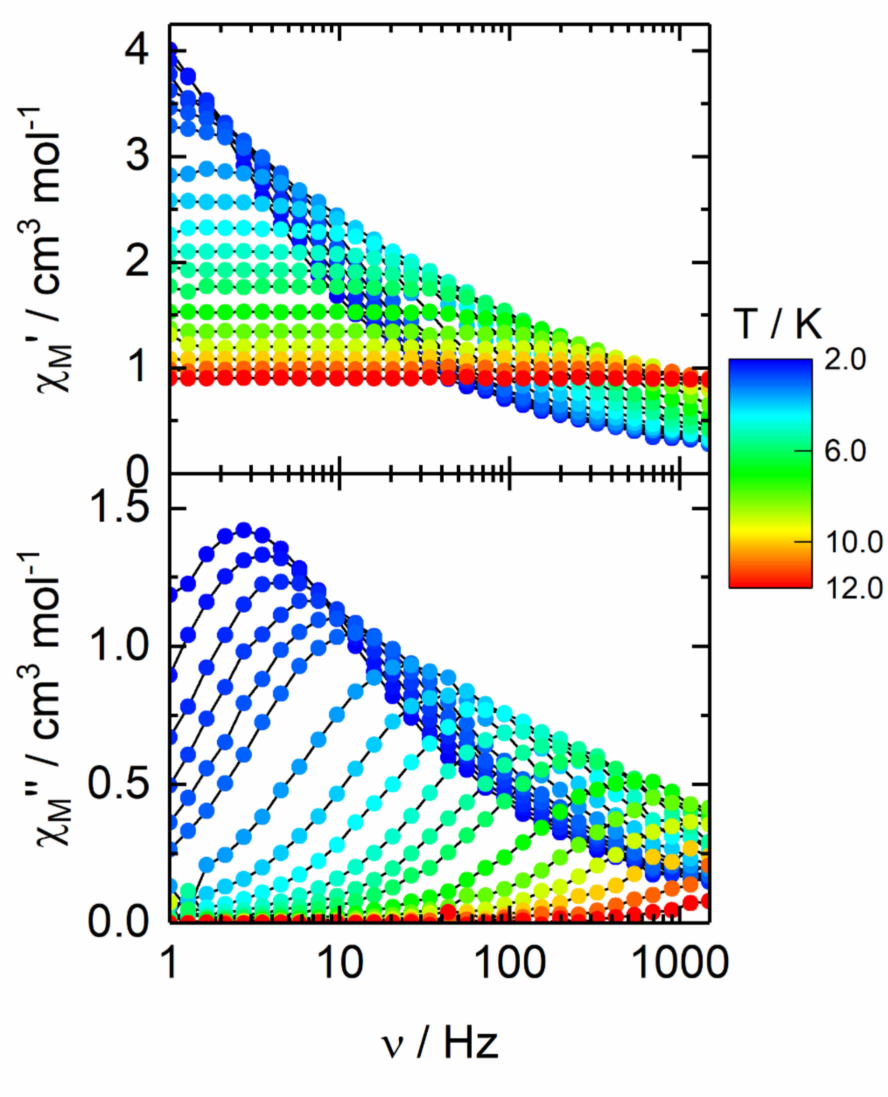

Figure S60. Frequency dependence of the in-phase (above) and out-of phase (below) components of the magnetic susceptibility for **1** under an applied magnetic field of 1500 Oe in the temperature range 2-12 K.

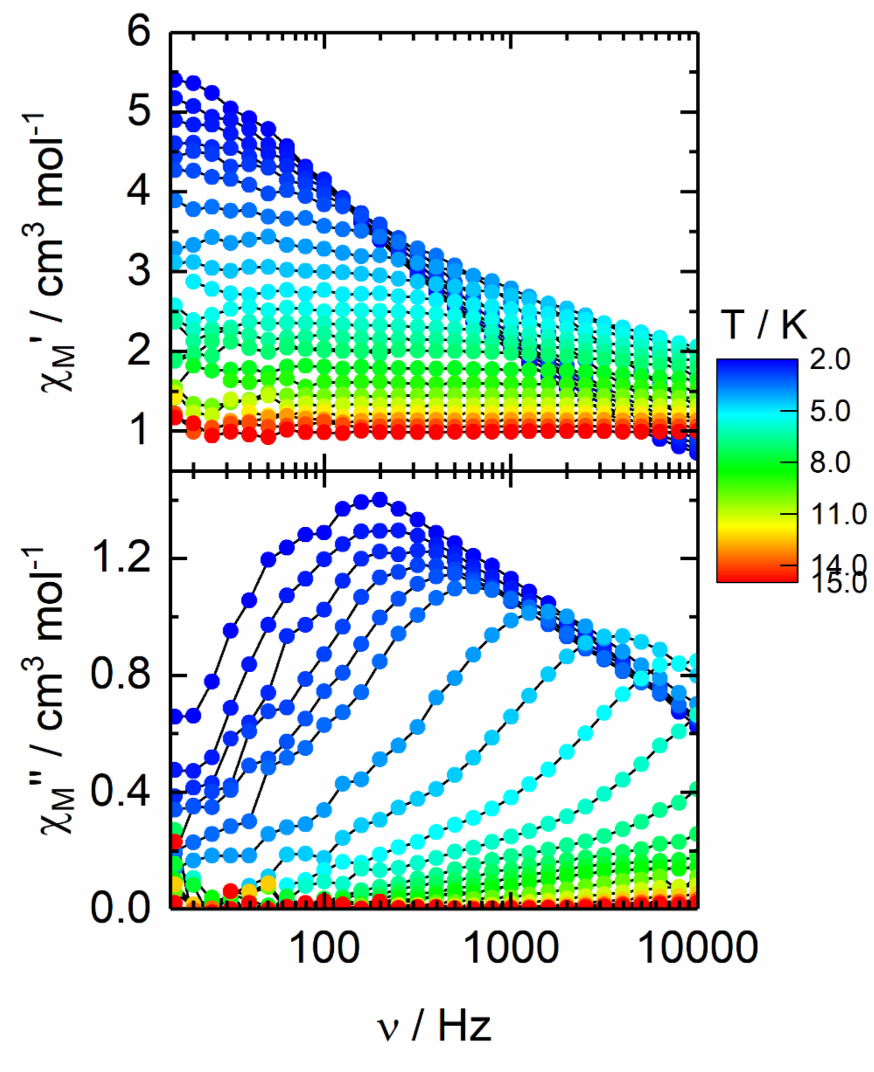

Figure S61. Frequency dependence of the in-phase (above) and out-of phase (below) components of the magnetic susceptibility for **2** under an applied magnetic field of 1500 Oe in the temperature range 2-15 K.

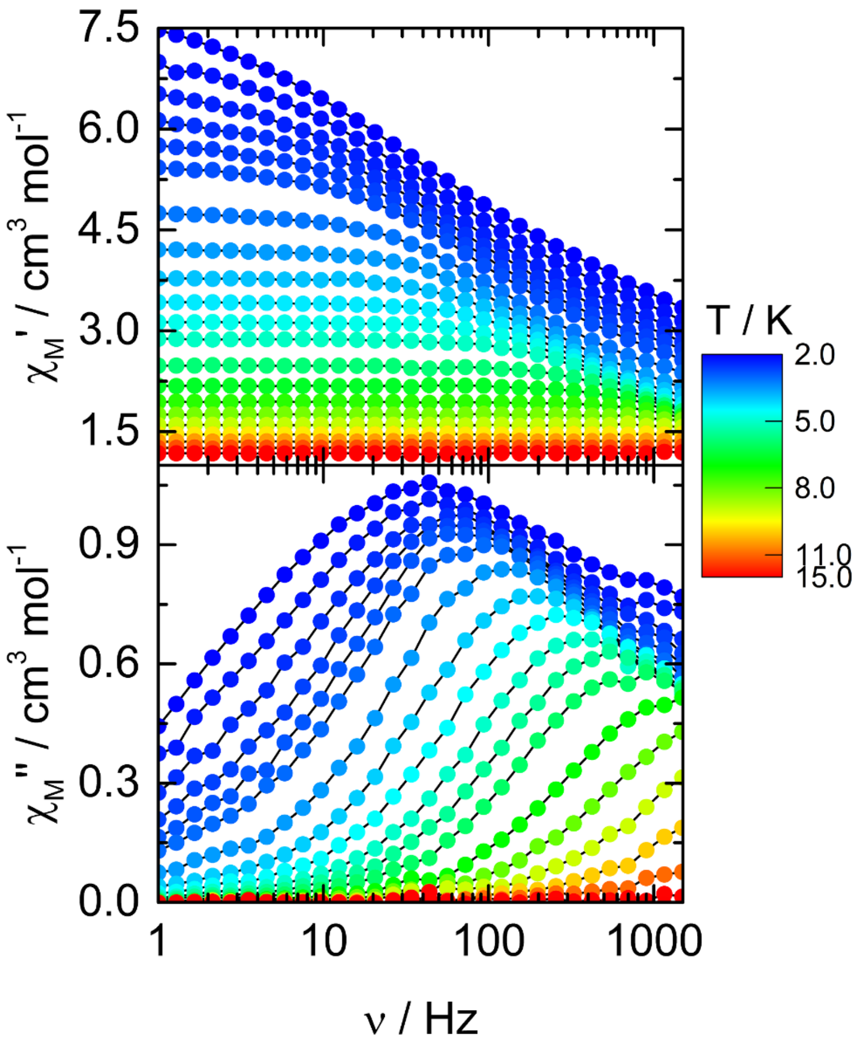

Figure S62. Frequency dependence of the in-phase (above) and out-of phase (below) components of the magnetic susceptibility for **4** under an applied magnetic field of 1500 Oe in the temperature range 2-15 K.

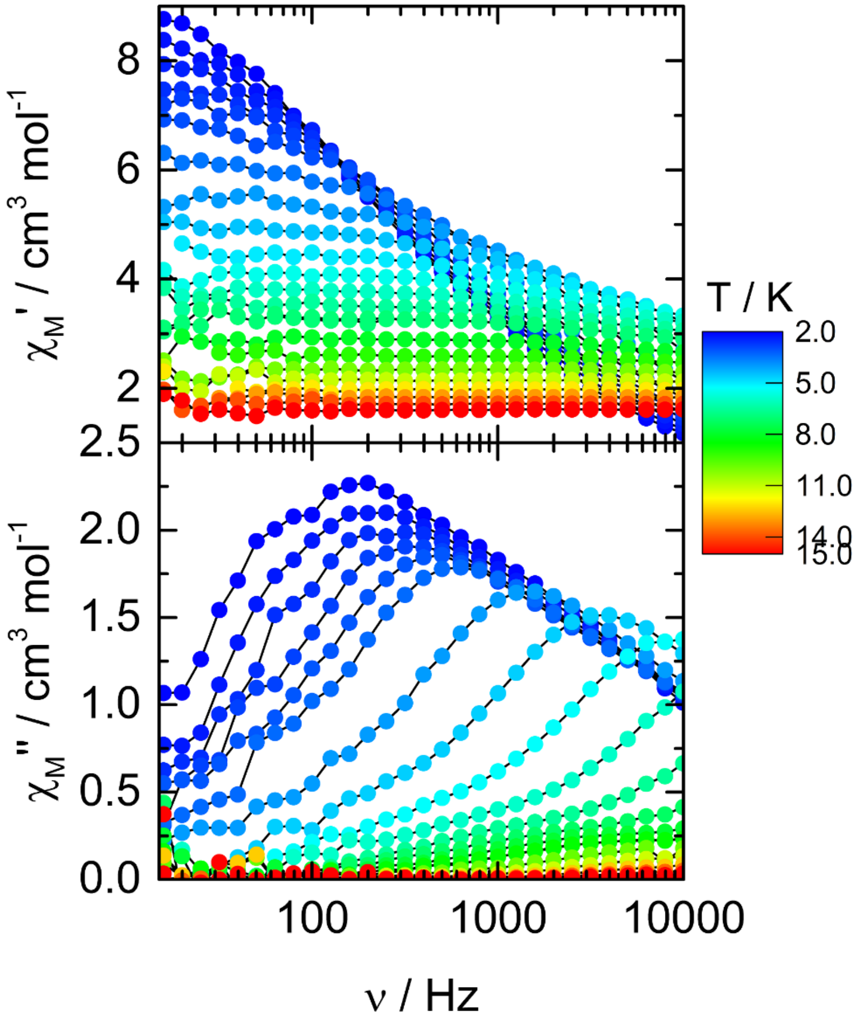

Figure S63. Frequency dependence of the in-phase (above) and out-of phase (below) components of the magnetic susceptibility for **7** under an applied magnetic field of 1500 Oe in the temperature range 2-15 K.

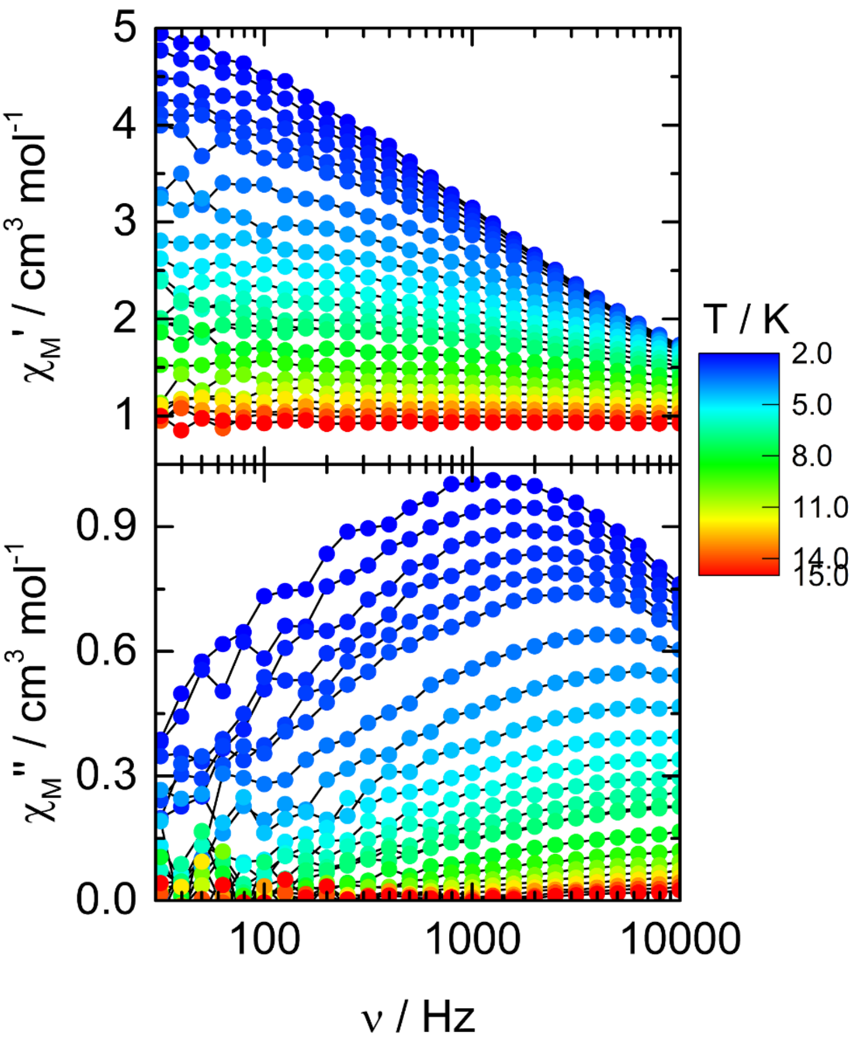

Figure S64. Frequency dependence of the in-phase (above) and out-of phase (below) components of the magnetic susceptibility for **9** under an applied magnetic field of 1500 Oe in the temperature range 2-15 K.

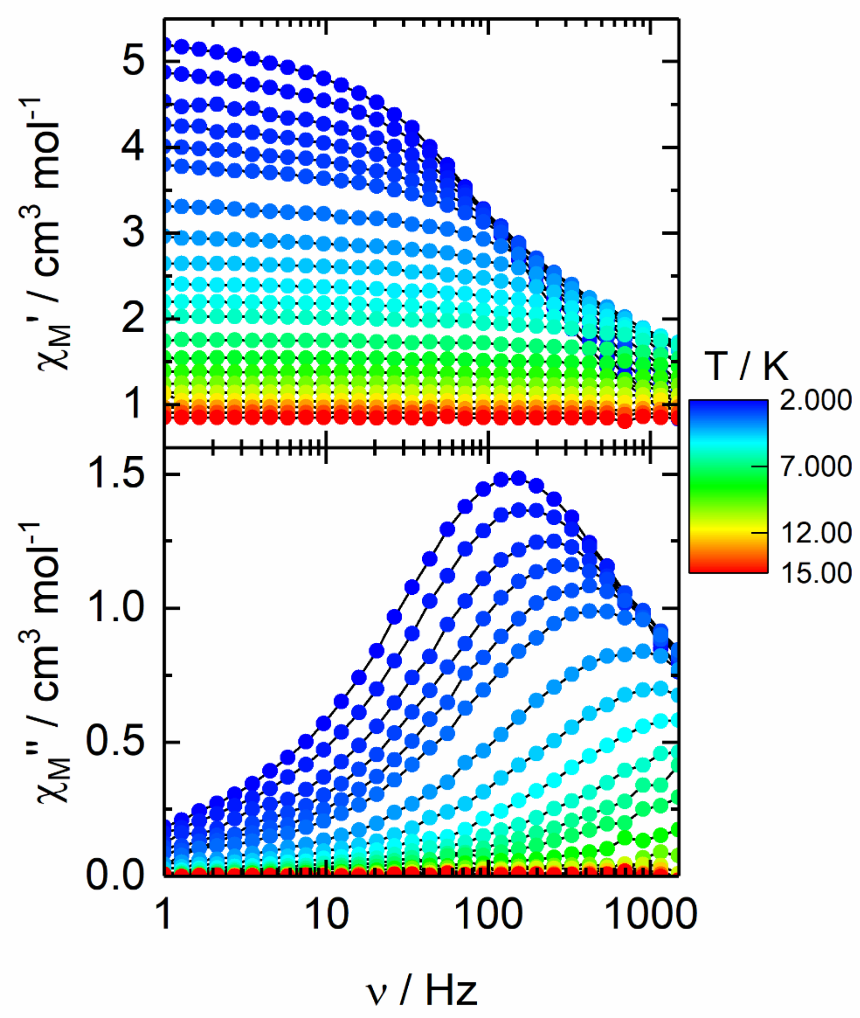

Figure S65. Frequency dependence of the in-phase (above) and out-of phase (below) components of the magnetic susceptibility for **11** under an applied magnetic field of 1500 Oe in the temperature range 2-15 K.

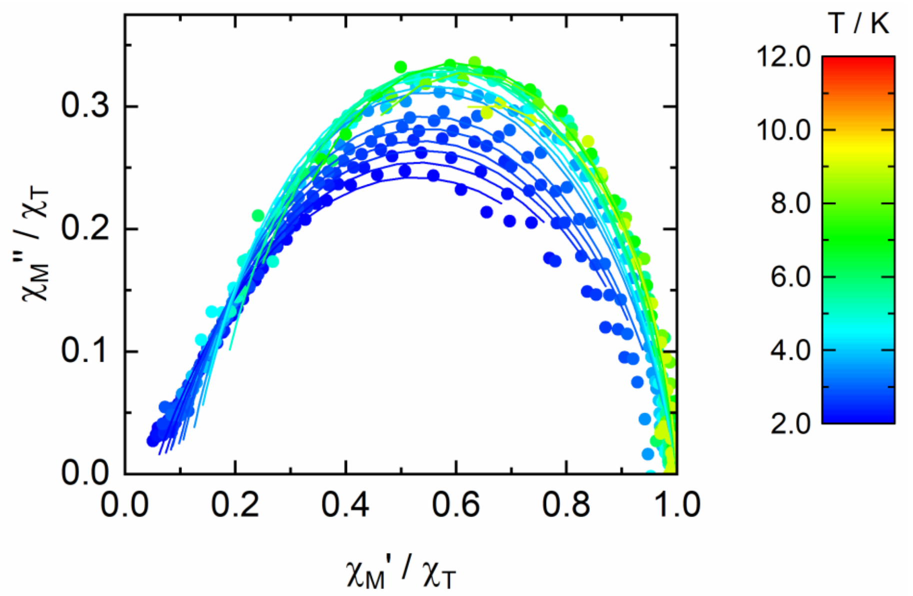

Figure S66. Normalized Cole-Cole plots for **1** at several temperatures between 2 and 9 K under an applied magnetic field of 1.5 kOe. Full lines are the best fitted curve with the extended Debye model.

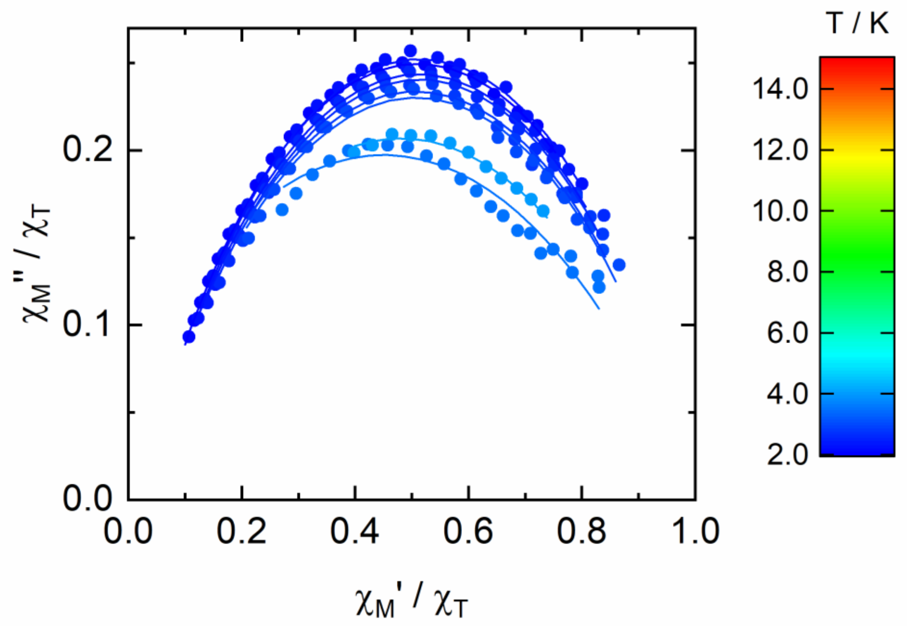

Figure S67. Normalized Cole-Cole plots for **2** at several temperatures between 2 and 4.5 K under an applied magnetic field of 1.5 kOe. Full lines are the best fitted curve with the extended Debye model.

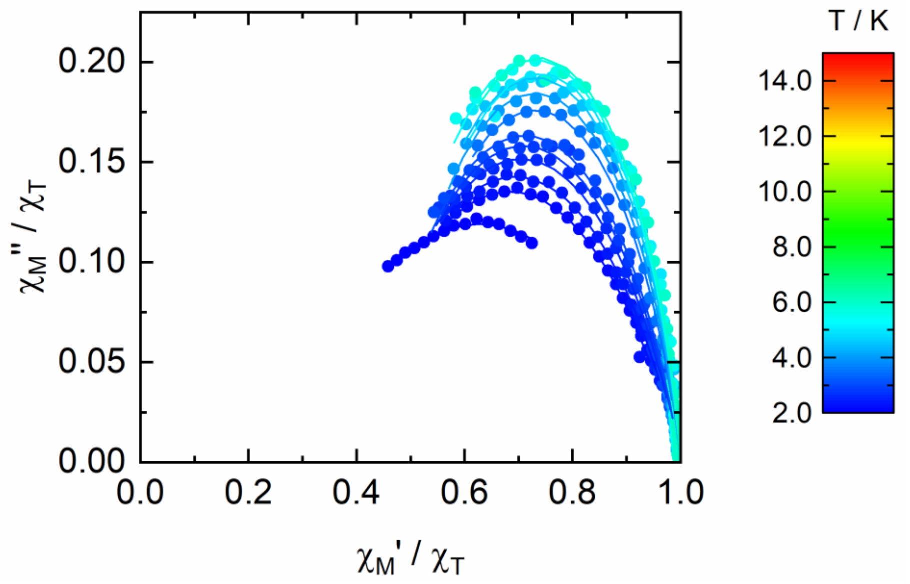

Figure S68. Normalized Cole-Cole plots for **4** at several temperatures between 2 and 6.5 K under an applied magnetic field of 1.5 kOe. Full lines are the best fitted curve with the extended Debye model.

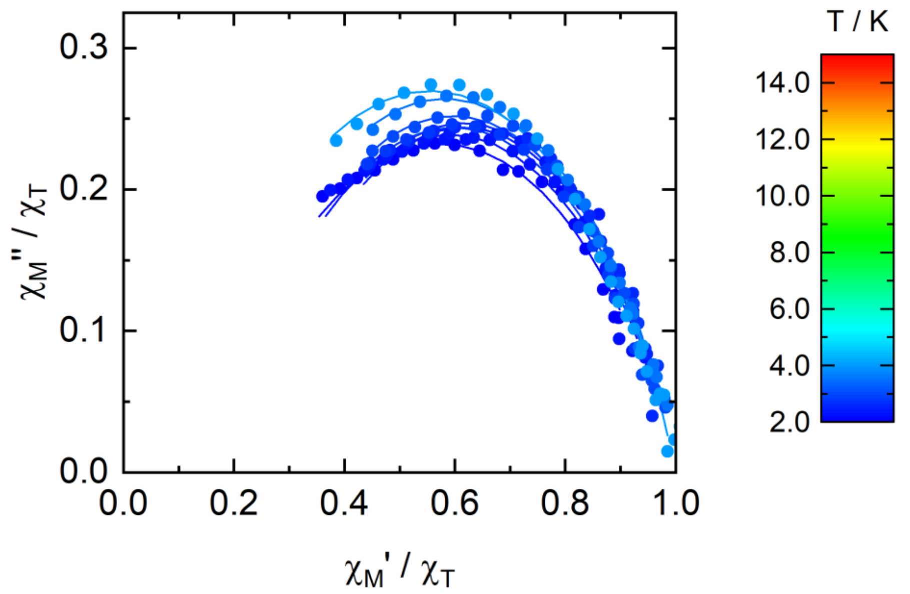

Figure S69. Normalized Cole-Cole plots for **7** at several temperatures between 2 and 4.5 K under an applied magnetic field of 1.5 kOe. Full lines are the best fitted curve with the extended Debye model.

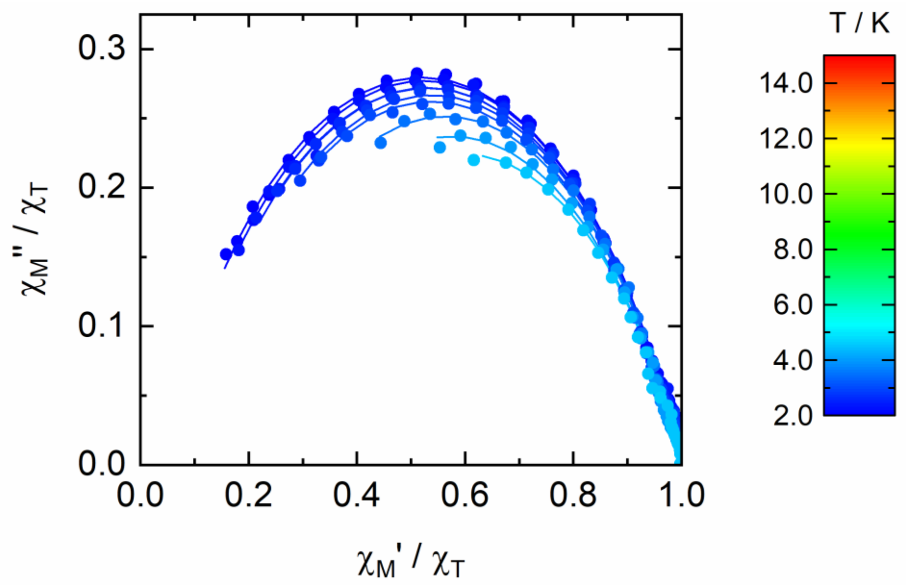

Figure S70. Normalized Cole-Cole plots for **11** at several temperatures between 2 and 4.5 K under an applied magnetic field of 1.5 kOe. Full lines are the best fitted curve with the extended Debye model.

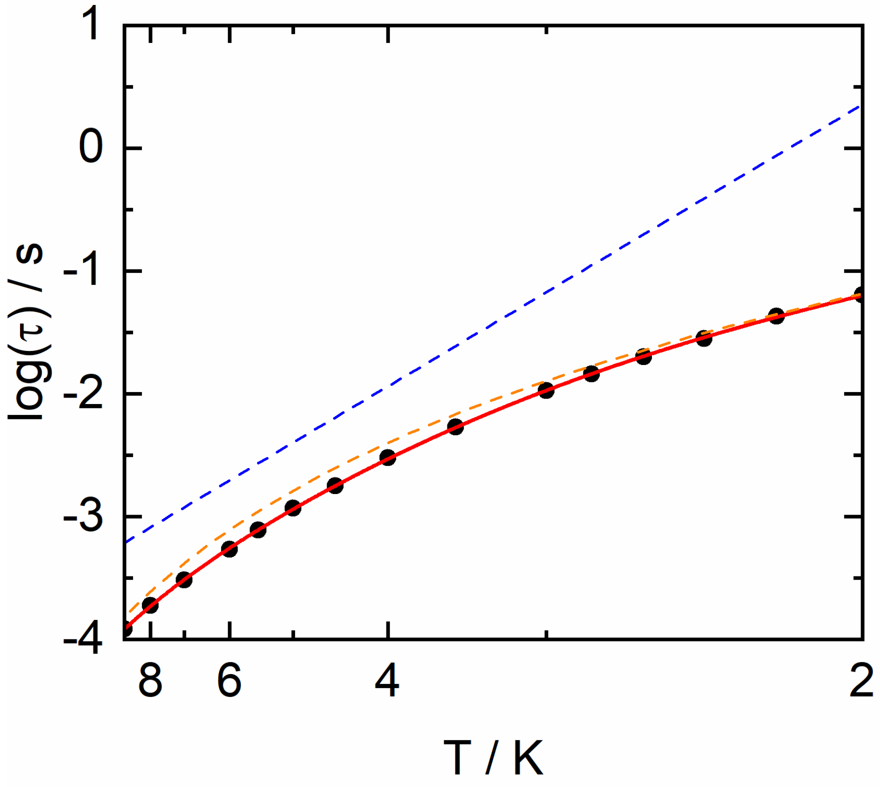

Figure S71. Temperature dependence of the relaxation time for **1** at 1.5 kOe in the temperature range of 2 – 9 K with the best-fitted curve (full red line) with the combination Orbach + Raman processes. The Orbach and Raman contributions to the relaxation time are respectively represented in dashed blue line and dashed orange line (the parameters are given in Table S16).

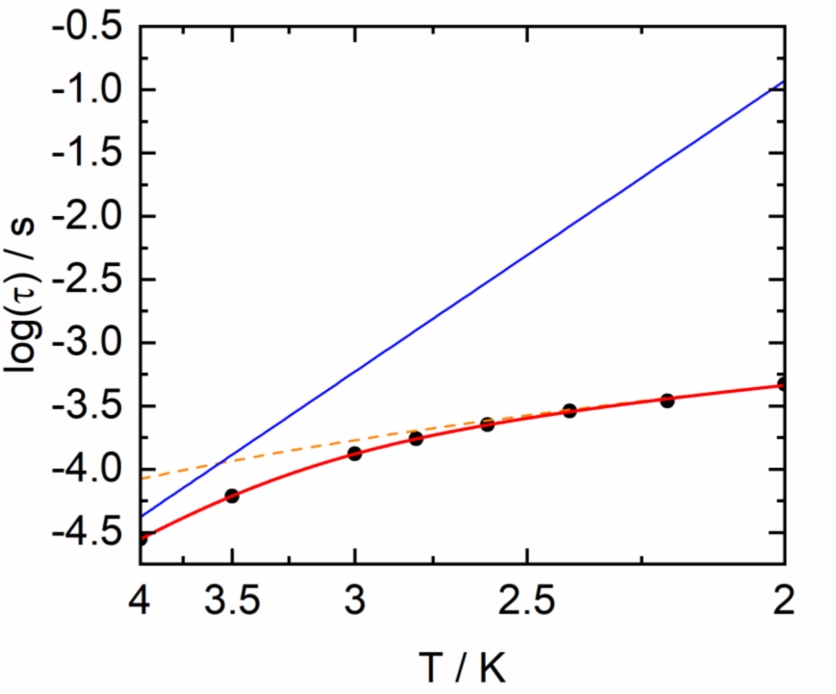

Figure S72. Temperature dependence of the relaxation time for **2** at 1.5 kOe in the temperature range of 2 – 4 K with the best-fitted curve (full red line) with the combination Orbach + Raman processes. The Orbach and Raman contributions to the relaxation time are respectively represented in blue line and dashed orange line (the parameters are given in Table S16).

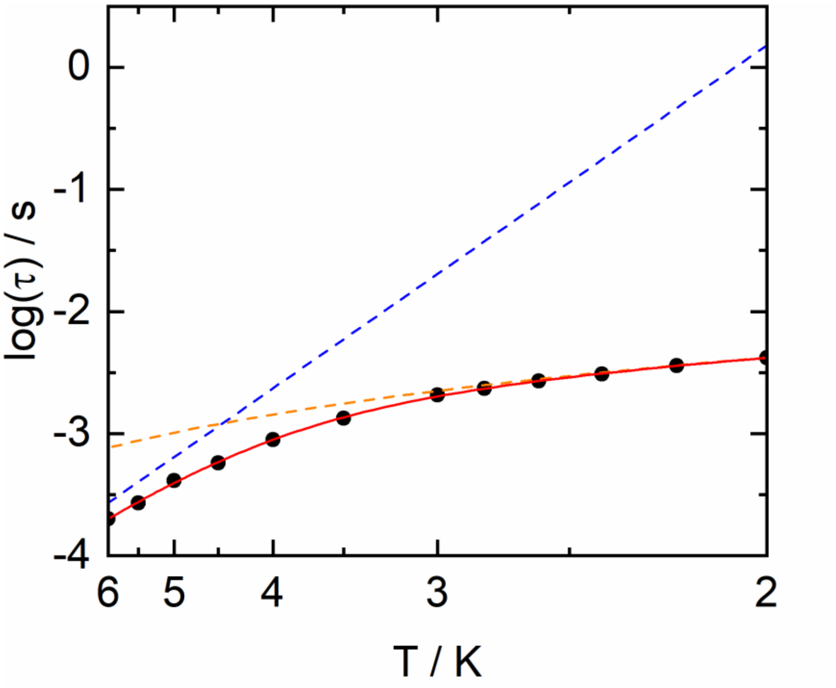

Figure S73. Temperature dependence of the relaxation time for **4** at 1.5 kOe in the temperature range of 2 – 6 K with the best-fitted curve (full red line) with the combination Orbach + Raman processes. The Orbach and Raman contributions to the relaxation time are respectively represented in dashed blue line and dashed orange line (the parameters are given in Table S16).

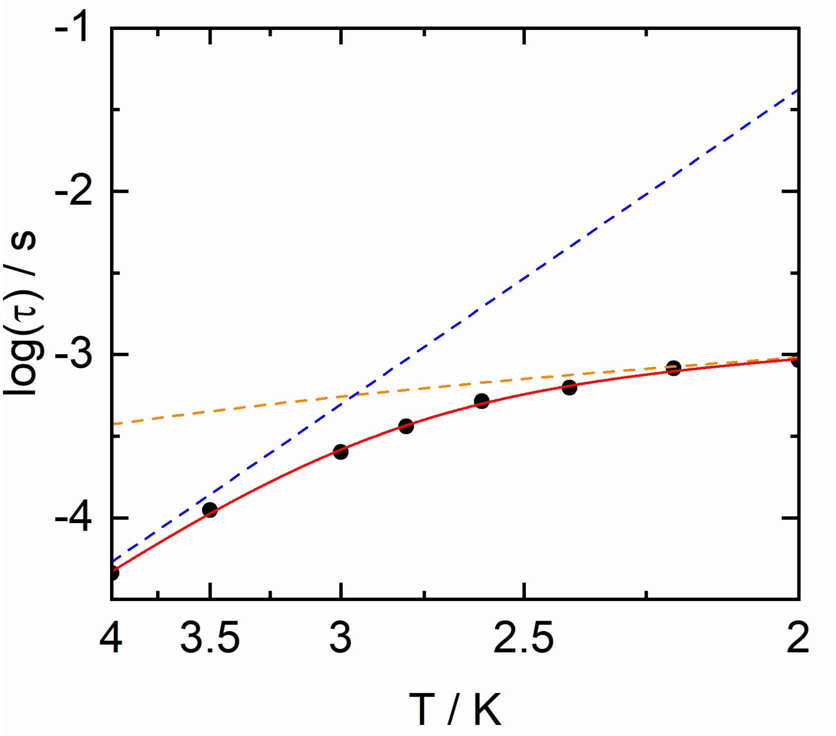

Figure S74. Temperature dependence of the relaxation time for **7** at 1.5 kOe in the temperature range of 2 – 4 K with the best-fitted curve (full red line) with the combination Orbach + Raman processes. The Orbach and Raman contributions to the relaxation time are respectively represented in dashed blue line and dashed orange line (the parameters are given in Table S16).

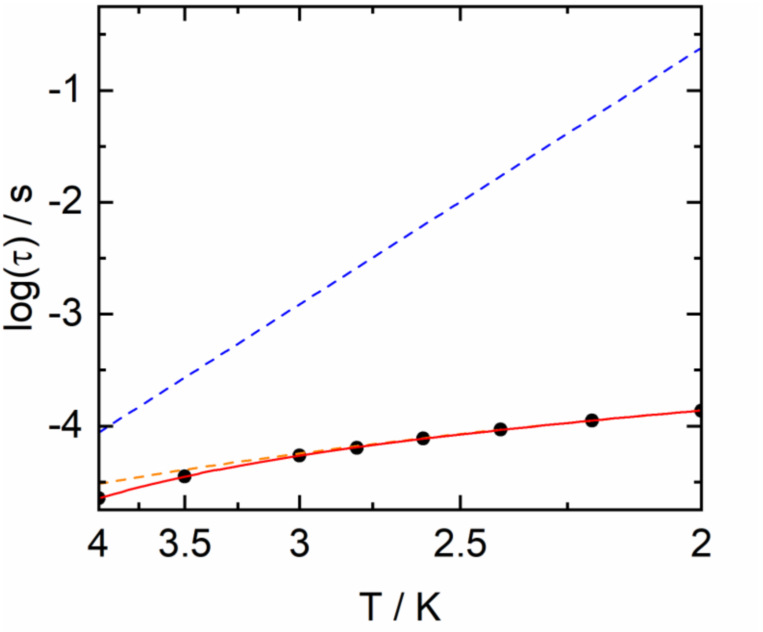

Figure S75. Temperature dependence of the relaxation time for **9** at 1.5 kOe in the temperature range of 2 – 4 K with the best-fitted curve (full red line) with the combination Orbach + Raman processes. The Orbach and Raman contributions to the relaxation time are respectively represented in dashed blue line and dashed orange line (the parameters are given in Table S16).

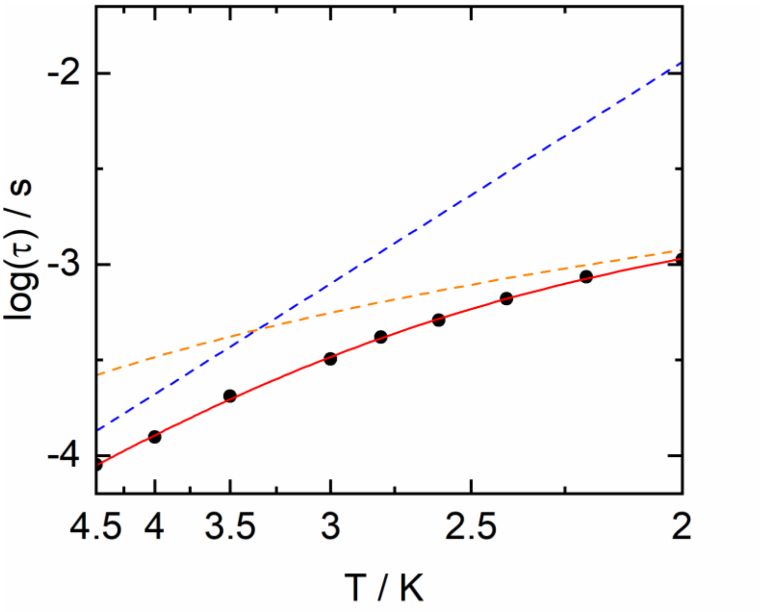

Figure S76. Temperature dependence of the relaxation time for **11** at 1.5 kOe in the temperature range of 2 – 4.5 K with the best-fitted curve (full red line) with the combination Orbach + Raman processes. The Orbach and Raman contributions to the relaxation time are respectively represented in dashed blue line and dashed orange line (the parameters are given in Table S16).

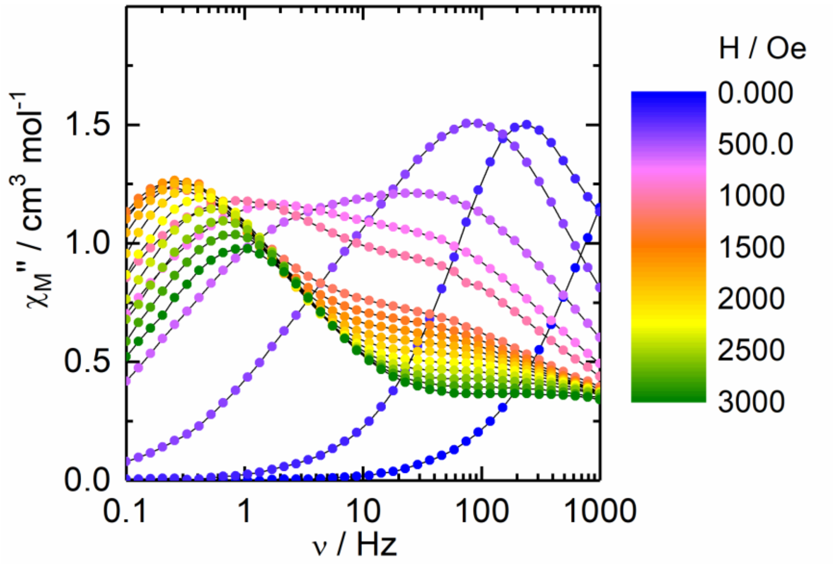

Figure S77. Frequency variation of χ_M'' for **15** at 2 K at various external dc fields.

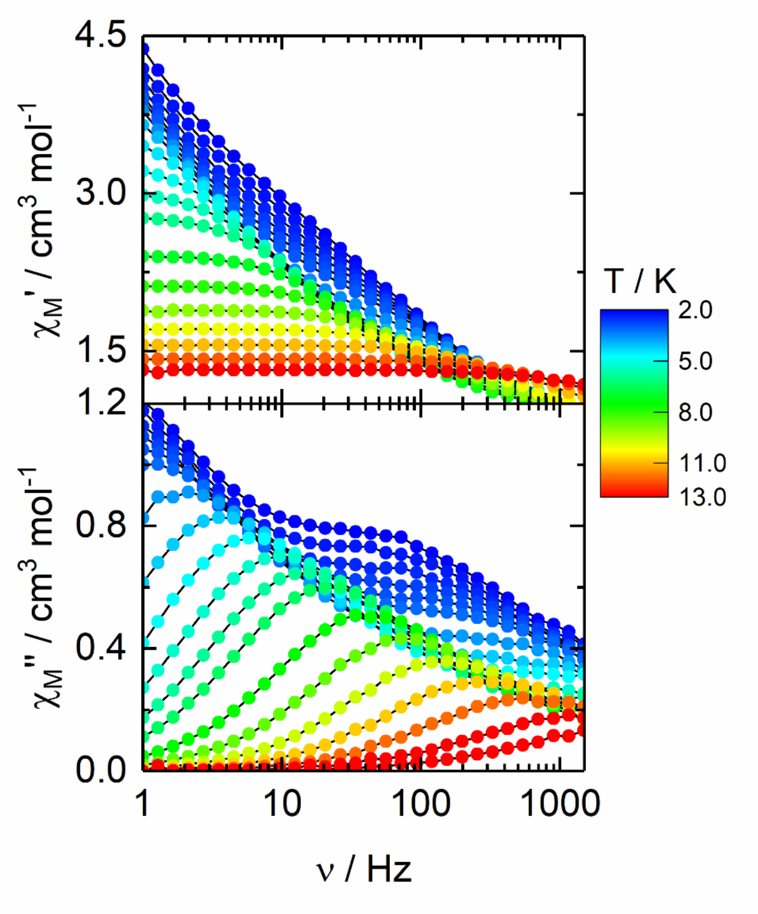

Figure S78. Frequency dependence of the in-phase (above) and out-of phase (below) components of the magnetic susceptibility for **15** under an applied magnetic field of 1500 Oe in the temperature range 2-13 K.

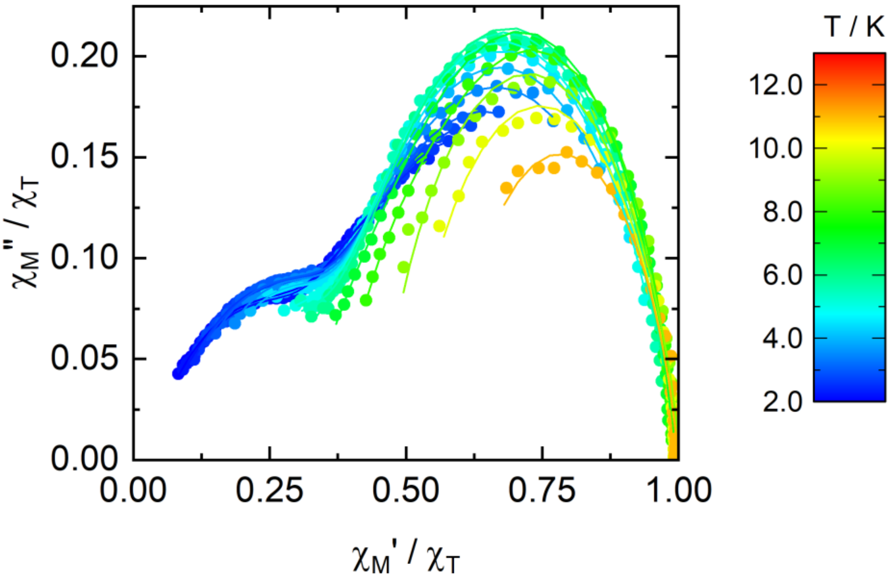

Figure S79. Normalized Cole-Cole plots for **15** at several temperatures between 2 and 11 K under an applied magnetic field of 1.5 kOe. Full lines are the best fitted curve with the extended Debye model.

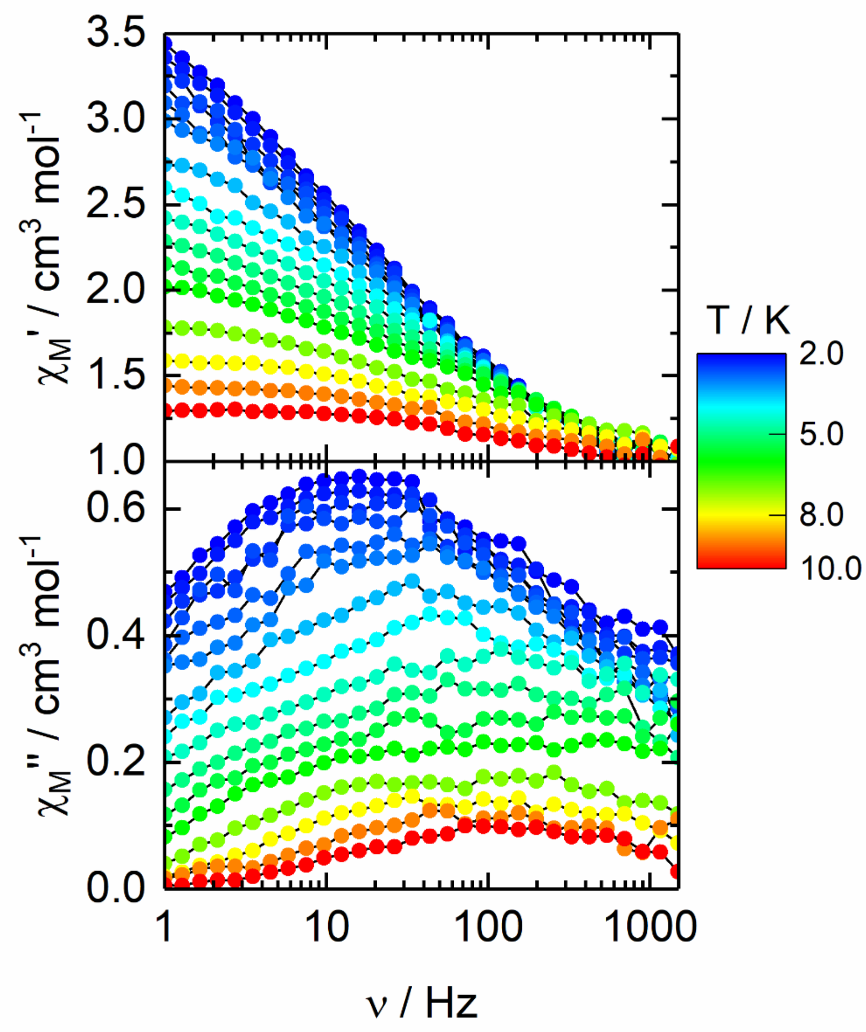

Figure S79. Frequency dependence of the in-phase (above) and out-of phase (below) components of the magnetic susceptibility for **16** under an applied magnetic field of 3000 Oe in the temperature range 2-10 K.

Table S1. X-ray crystallographic data for the complexes **1**, **3**, **4**, **6**, **8**, **11-13**.

Compounds	[CdDy(hfac)$_5$(**L**)]$_2$ (**1**)	[ZnYb(hfac)$_5$(**L**)]$_2$·(CH$_2$Cl$_2$) (**3**)	[MnDy(hfac)$_5$(**L**)]·2(CH$_2$Cl$_2$) (**4**)
Formula	$C_{118}H_{70}Cd_2Dy_2F_{60}N_{16}O_{20}S_{12}$	$C_{119}H_{72}Cl_2Zn_2Yb_2F_{60}N_{16}O_{20}S_{12}$	$C_{61}H_{39}Cl_4MnDyF_{30}N_8O_{10}S_6$
M / g.mol^{-1}	4106.42	4118.36	2165.60
Crystal system	Triclinic	Triclinic	triclinic
Space group	P-1 (N°2)	P-1 (N°2)	P-1 (N°2)
Cell parameters	a = 12.700(3) Å	a = 12.640(4) Å	a = 12.813(2) Å
	b = 24.985(5) Å	b = 26.082(8) Å	b = 17.119(3) Å
	c = 26.286(5) Å	c = 26.380(8) Å	c = 19.788(4) Å
	α = 101.213(6)°	α = 101.645(8)°	α = 86.381(6)°
	β = 99.668(5)°	β = 90.606(9)°	β = 89.219(6)°
	γ = 98.737(6)°	γ = 100.406(9)°	γ = 76.672(6)°
Volume / Å^3	7917(3)	8368(5)	4215.0(14)
Cell formula units	2	2	2
T / K	150 (2)	150(2)	150(2)
Diffraction reflection	$5.83 \leq 2\theta \leq 54.97$	$4.16 \leq 2\theta \leq 55.52$	$4.12 \leq 2\theta \leq 55.49$
ρ_{calc}, g.cm^{-3}	1.723	1.641	1.706
μ, mm^{-1}	1.490	1.701	1.427
Number of reflections	193117	276977	78615
Independent reflections	36147	38578	19393
Fo^2 > 2σ(Fo)^2	17178	18770	13489
Number of variables	2120	2058	1087
R$_{int}$, R$_1$, wR$_2$	0.1721, 0.1650, 0.4257	0.2104, 0.1184, 0.2354	0.1006, 0.1338, 0.3231
CCDC numbers	1865127	1865128	1865129

Compounds	[CoY(hfac)$_5$(**L**)]·(CH$_2$Cl$_2$) (**6**)	[CoYb(hfac)$_5$(**L**)] (**8**)	[ZnDy(tta)$_2$(hfac)$_3$(**L**)]·(CH$_2$Cl$_2$) (**11**)
Formula	$C_{60}H_{37}Cl_2CoYF_{30}N_8O_{10}S_6$	$C_{59}H_{35}CoYbF_{30}N_8O_{10}S_6$	$C_{66}H_{43}Cl_2ZnDyF_{24}N_8O_{10}S_8$
M / g.mol^{-1}	2011.07	2010.28	2119.33
Crystal system	Monoclinic	triclinic	triclinic
Space group	P2$_1$/n (N°14)	P-1 (N°2)	P-1 (N°2)
Cell parameters	a = 13.189(2) Å	a = 12.664(3) Å	a = 13.226(3) Å
	b = 16.340(3) Å	b = 16.455(4) Å	b = 17.850(3) Å
	c = 40.379(7) Å	c = 21.398(5) Å	c = 21.031(4) Å
		α = 90.682(8)°	α = 102.119(5)°
	β = 98.251(4)°	β = 102.892(8)°	β = 93.735(5)°
		γ = 93.699(9)°	γ = 110.483(5)°
Volume / Å^3	8612(2)	4335.9(17)	4495.3(15)
Cell formula units	4	2	2
T / K	150 (2)	150(2)	150(2)
Diffraction reflection	$2.28 \leq 2\theta \leq 55.10$	$1.95\leq 2\theta \leq 55.12$	$5.83\leq 2\theta \leq 54.97$
ρ_{calc}, g.cm^{-3}	1.683	1.540	1.566
μ, mm^{-1}	1.256	1.524	1.440
Number of reflections	62407	88634	82862
Independent reflections	18545	18906	20454
Fo^2 > 2σ(Fo)^2	5686	6583	5657
Number of variables	1140	1074	1073
R$_{int}$, R$_1$, wR$_2$	0.2160, 0.1984, 0.4781	0.2107, 0.1496, 0.3248	0.2256, 0.1697, 0.3840

CCDC numbers	1865131	1865133	1865134

Compounds	[Cu(hfac)(CH_3OH)(**L**)]·0.5(C_6H_{14}) (**12**)	[Cu(H_2O)Dy(hfac)$_4$(**L**)]·[Dy(hfac)$_4$]·(CH_2Cl_2) (**13**)
Formula	$C_{31}H_{31}CuF_6N_1O_3S_6$	$C_{75}H_{42}Cl_2CuDy_2F_{48}N_8O_{17}S_6$
M / g.mol^{-1}	863.54	2888.95
Crystal system	Triclinic	Triclinic
Space group	P-1 (N°2)	P-1 (N°2)
Cell parameters	a = 9.7341(18) Å	a = 14.501(4) Å
	b = 13.820(3) Å	b = 19.225(6) Å
	c = 15.588(3) Å	c = 20.545(6) Å
	α = 113.594(6)°	α = 91.777(10)°
	β = 107.762(6)°	β = 103.902(9)°
	γ = 93.416(6)°	γ = 111.996(9)°
Volume / Å^3	1790.0(6)	5108(3)
Cell formula units	2	2
T / K	150	150
Diffraction reflection	$4.43 \le 2\theta \le 54.89$	$5.83 \le 2\theta \le 54.97$
ρ_{calc}, g.cm^{-3}	1.602	1.878
μ, mm^{-1}	1.029	1.981
Number of reflections	36206	103507
Independent reflections	8146	23325
$Fo^2 > 2\sigma(Fo)^2$	5127	16423
Number of variables	442	1427
R_{int}, R_1, wR_2	0.0814, 0.0707, 0.1821	0.1656, 0.2073, 0.5031
CCDC numbers	1865130	1865132

Table S2. X-ray crystallographic data for the complexes **14-19**.

Compounds	[Pr(hfac)$_3$(**L**)]$_2$·0.5(C_6H_{14}) (**14**)	[$Dy_{1.21}Nd_{0.79}$(hfac)$_6$(L)]·2(CH_2Cl_2)·(C_6H_{14}) (**15**)	[$Dy_{1.11}Nd_{0.89}$(tta)$_3$(hfac)$_3$(L)] (**16**)
Formula	$C_{101}H_{73}Pr_2F_{36}N_{16}O_{12}S_{12}$	$C_{72}H_{54}Cl_4Dy_{1.21}Nd_{0.79}F_{36}N_8O_{12}S_6$	$C_{73}H_{45}Dy_{1.11}Nd_{0.89}F_{27}N_8O_{12}S_9$
M / g.mol^{-1}	3053.3	2550.57	2336.46
Crystal system	monoclinic	monoclinic	Triclinic
Space group	C2/c (N°15)	P2$_1$/n (N°14)	P-1 (N°2)
	a = 42.278(14) Å	a = 22.440(2) Å	a = 10.170(2) Å
	b = 11.697(4) Å	b = 12.6945(12) Å	b = 16.139(3) Å
Cell parameters	c = 50.539(17) Å	c = 33.791(3) Å	c = 30.871(6) Å
			α = 97.354(6)°
	β = 92.934(4)°	β = 100.983(3)°	β = 91.253(6)°
			γ = 99.875(6)°
Volume / Å^3	24960(14)	9449.7(16)	4946.0(17)
Cell formula units	2	4	2
T / K	150 (2)	150(2)	150(2)
Diffraction reflection	$5.45 \le 2\theta \le 55.35$	$5.86 \le 2\theta \le 54.97$	$5.83 \le 2\theta \le 54.96$
ρ_{calc}, g.cm^{-3}	1.636	1.794	1.569
μ, mm^{-1}	1.099	1.765	1.590
Number of reflections	72888	103333	83873
Independent reflections	29067	20831	21407

$Fo^2 > 2\sigma(Fo)^2$	10203	17401	12845
Number of variables	1535	1214	1178
R_{int}, R_1, wR_2	0.2119, 0.1293, 0.2889	0.0689, 0.1172, 0.2726	0.0985, 0.1494, 0.3369
CCDC numbers	1865135	1865136	1865138

Compounds	$[Yb_{1.04}Nd_{0.96}(hfac)_6(\mathbf{L})]$ (**17**)	$[Nd_2(hfac)_6(\mathbf{L})]\cdot(C_6H_{14})$ (**18**)	$[YbPr(hfac)_6(\mathbf{L})]$ (**19**)
Formula	$C_{64}H_{36}Yb_{1.04}Nd_{0.96}F_{36}N_8O_{12}S_6$	$C_{70}H_{50}Nd_2F_{36}N_8O_{12}S_6$	$C_{64}H_{36}YbPrF_{36}N_8O_{12}S_6$
M / g.mol^{-1}	2303.80	2360.02	2299.32
Crystal system	Monoclinic	monoclinic	monoclinic
Space group	$P2_1/n$ (N°14)	$P2_1/n$ (N°2)	$P2_1/n$ (N°2)
	a = 22.2669(16) Å	a = 22.811(4) Å	a = 22.487(5) Å
	b = 12.6525(9) Å	b = 12.634(2) Å	b = 12.711(2) Å
Cell parameters	c = 33.194(2) Å	c = 31.848(6) Å	c = 33.458(7) Å
	β = 99.920(2)°	β = 103.311(5)°	β = 100.768(7)°
Volume / Å^3	9212.0(11)	8932(3)	9395(3)
Cell formula units	4	4	4
T / K	150 (2)	150(2)	150(2)
Diffraction reflection	$4.292 \leq 2\theta \leq 55.16$	$5.94 \leq 2\theta \leq 54.96$	$5.94 \leq 2\theta \leq 54.96$
ρ_{calc}, g.cm^{-3}	1.660	1.755	1.626
μ, mm^{-1}	1.830	1.425	1.731
Number of reflections	116477	113102	69279
Independent reflections	21085	20331	20218
$Fo^2 > 2\sigma(Fo)^2$	11609	6634	12433
Number of variables	1323	1155	1140
R_{int}, R_1, wR_2	0.0745, 0.1339, 0.3397	0.5182, 0.1417, 0.2339	0.1091, 0.2464, 0.5190
CCDC numbers	1865140	1865139	1865137

Table S3. Cell parameters for the compounds **2**, **5**, **7**, **9** and **10**.

Compounds	$[ZnDy(hfac)_5(\mathbf{L})]\cdot 2(CH_2Cl_2)\cdot(C_6H_{14})$ (**2**)	$[MnYb(hfac)_5(\mathbf{L})]\cdot 2(CH_2Cl_2)$ (**5**)	$[CoDy(hfac)_5(\mathbf{L})]\cdot 2(CH_2Cl_2)\cdot(C_6H_{14})$ (**7**)
Formula	$C_{67}H_{53}Cl_4ZnDyF_{30}N_8O_{10}S_6$	$C_{61}H_{39}Cl_4MnYbF_{30}N_8O_{10}S_6$	$C_{67}H_{53}Cl_4CoDyF_{30}N_8O_{10}S_6$
M / g.mol^{-1}	2260.90	2166.38	2255.77
Crystal system	Monoclinic	Triclinic	Monoclinic
	a = 13.0349(50) Å	a = 12.6744(19) Å	a = 13.0886(24) Å
	b = 16.0719(67) Å	b = 17.2322(26) Å	b = 16.1922(30) Å
Cell parameters	c = 40.5385(143) Å	c = 19.7161(29) Å	c = 40.6329(76) Å
		α = 93.2236(54)°	
	β = 98.7432(113)°	β = 91.3049(54)°	β = 99.1885(46)°
		γ = 104.6066(61)°	
Volume / Å^3	8393.94(912)	4157.34(170)	8500.95(457)
Z	4	2	4
T / K	150 (2)	150(2)	150(2)
2θ range /°	4.74 ≤ 2θ ≤ 38.96	4.68 ≤ 2θ ≤ 37.92	4.72 ≤ 2θ ≤ 37.22
Number of reflections	9185	5975	9906

Compounds	$[NiDy(hfac)_5(\mathbf{L})]\cdot 2(CH_2Cl_2)\cdot(C_6H_{14})$ (**9**)	$[NiYb(hfac)_5(\mathbf{L})]$ (**10**)	
Formula	$C_{67}H_{53}Cl_4NiDyF_{30}N_8O_{10}S_6$	$C_{59}H_{35}NiYbF_{30}N_8O_{10}S_6$	
M / g.mol^{-1}	2255.57	2010.08	
Crystal system	Monoclinic	Triclinic	
Cell parameters	a = 13.1928(18) Å	a = 12.7539(33) Å	
	b = 16.1446(23) Å	b = 16.3134(45) Å	
	c = 39.8516(59) Å	c = 21.1691(56) Å	
		α = 90.6833(80)°	
	β = 98.7085(46)°	β = 102.7846(76)°	
		γ = 94.2735(83)°	
Volume / Å^3	8390.22(357)	4281.48(325)	
Z	4	2	
T / K	150(2)	150(2)	
2θ range /°	4.72 ≤ 2θ ≤ 37.22	4.54 ≤ 2θ ≤ 29.22	
Number of reflections		9872	

Table S4. Selected intra- and inter-molecular bond lengths (Å) for complexes **1, 3, 4, 6, 8, 11** and **13**.

	Average d(M-O)/Å	Average d(M-N)/Å	Average d(Ln-O)/Å	Average d(Ln-N)/Å	Intramolecular d(Ln-M)/Å	Intermolecular d(Ln-M)/Å	Intermolecular d(Ln-Ln)/Å
1	2.290(13) 2.268(15)	2.303(14) 2.279(18)	2.375(12) 2.343(14)	2.515(11) 2.518(18)	10.221(3) 10.766(3)	8.868(2) 9.003(2)	8.129(2) 8.419(2) 8.917(2)
3	2.102(9) 2.088(9)	2.102(11) 2.109(11)	2.330(10) 2.321(9)	2.482(10) 2.494(11)	9.723(3) 10.676(4)	9.271(3) 10.394(3)	8.716(2) 9.947(2) 10.255(2)
4	2.159(11)	2.226(12)	2.374(10)	2.535(10)	10.658(3)	9.072(3)	8.656(2)
6	2.047(13)	2.098(14)	2.344(13)	2.493(14)	10.104(3)	9.468(3)	10.283(3)
8	2.069(11)	2.074(13)	2.343(10)	2.480(13)	10.018(3)	10.631(3)	9.900(2)
11	2.117(13)	2.147(16)	2.365(11)	2.561(11)	10.005(3)	11.206(3)	8.989(2)
13	2.043(20)	1.990(25)	2.373(21) 2.328(21)	2.510(30) /	10.052(6)	5.989(4)	8.519(3)

Table S5. SHAPE analyses of the coordination polyhedra around the lanthanide ion in complexes **1, 3, 4, 6, 8**, **11** and **14**.

	Metal	CShM$_{TCTPR-9}$ (Spherical tricapped trigonal prism D_{3h})	CShM$_{CSAPR-9}$ (Spherical capped square antiprism C_{4v})	CShM$_{MFF-9}$ (Muffin C_s)
1	Dy1	0.942	0.936	1.402
	Dy2	1.313	0.553	0.931
3	Yb1	1.178	0.497	0.795
	Yb2	0.434	0.904	1.551
4	Dy1	1.512	0.708	0.995
6	Y1	0.901	0.854	1.040
8	Yb1	0.466	0.909	1.419
11	Dy1	0.790	1.081	1.474
14	Pr1	1.117	1.828	1.920
	Pr2	2.467	1.884	1.319

Table S6. Selected short contacts (Å) and angles (°) for complexes **1, 3, 4, 6, 8, 11** and **13**.

	α/Å	Short contacts/Å
1	74.4(4) 54.8(6)	S11···O2=3.058 S11···S3=3.381 S11···S4=3.681 S10···S5=3.787 S10···S6=3.691
3	76.2(3) 65.6(3)	S9···S5=3.690 S10···S6=3.743 S11···S3=3.597 S12···S4=3.654
4	69.7(4)	S5···S3=3.748 S6···S4=3.759
6	76.4(4)	S5···S3=3.796 S6···S4=3.626
8	69.8(4)	S5···S3=3.641 S6···S4=3.569
11	67.7(4)	S5···S3=3.706 S6···S4=3.680
13	84.6(4)	S8···S8=3.967

Table S7. Selected intra- and inter-molecular bond lengths (Å) for complexes **14-19**.

	Average d(Ln*-O)/Å	Average d(Ln*-N)/Å	Average d(Ln-O)/Å	Average d(Ln-N)/Å	Intramolecular d(Ln-Ln)/Å	Intermolecular d(Ln-Ln)/Å
14	2.474(11) 2.483(11)	2.647(12) 2.650(12)	/	/	/	9.592(3)
15	2.414(10)	2.573(11)	2.347(9)	2.547(10)	10.895(4)	9.690(3)
16	2.429(13)	2.597(14)	2.345(11)	2.521(12)	10.242(4)	8.613(2)
17	2.406(16)	2.619(11)	2.348(11)	2.541(10)	10.767(4)	9.098(3)
18	2.433(16)	2.623(16)	2.419(14)	2.623(13)	10.890(4)	8.259(3)
19	2.447(19)	2.620(19)	2.306(17)	2.540(19)	10.859(4)	9.534(2)
Dy2	2.362	2.527	2.339	2.527		
Yb2	2.333	2.487	2.295	2.490		

* Lanthanide ion in the N_3O_9 coordination site.

Table S8. Selected short contacts (Å) and angles (°) for complexes **14-19**.

	α/Å	Short contacts/Å
14	86.1(3) 86.2(4)	S4···S9 = 3.714 S4···S10 = 3.719 S5···S11 = 3.714 S5···S12 = 3.732
15	76.1(3)	S3···S6=3.785
16	73.5(3)	S4···S6=3.672
17	72.6(3)	S3···S6=3.649
18	77.9(5)	S4···S5=3.595
19	80.8(5)	S4···S5=3.750

Table S9. SHAPE analyses of the coordination polyhedra around the lanthanide ion in complexes **15-19**.

	Metal	CShM$_{SAPR-8}$ (square antiprism D_{4d})	CShM$_{TDD-8}$ (triangular dodecahedron D_{2d})	CShM$_{BTPR-8}$ (biaugmented trigonal prism C_{2v})	CShM$_{TCTPR-9}$ (spherical tricapped trigonal prism D_{3h})	CShM$_{CSAPR-9}$ (spherical capped square antiprism C_{4v})	CShM$_{MFF-9}$ (Muffin C_s)
15	Dy1	0.487	2.797	2.503	-	-	-
	Nd1/Dy2	-	-	-	0.663	1.111	1.435
16	Dy1	0.908	1.796	1.744	-	-	-
	Nd1/Dy2	-	-	-	0.577	0.981	1.486
17	Yb1	0.540	2.623	2.403	-	-	-
	Nd1/Yb2	-	-	-	0.911	1.097	1.308
18	Nd1	0.627	2.515	2.543	-	-	-
	Nd2	-	-	-	0.877	0.844	1.432
19	Yb1	0.439	2.773	2.399	-	-	-
	Pr1	-	-	-	0.785	1.198	1.621

Table S10. Oxidation potentials (V *vs* SCE, nBu_4NPF_6, 0.1 M in CH_2Cl_2 at 100 mV.s^{-1}) of the complexes **1-19**.

	$E^1_{1/2}$ / V		$E^2_{1/2}$ / V	
	$^{Ox}E^1_{1/2}$	$^{Red}E^1_{1/2}$	$^{Ox}E^2_{1/2}$	$^{Red}E^2_{1/2}$
1	0.58	0.46	0.98	0.82
2	0.60	0.51	1.01	0.88
3	0.55	0.44	0.99	0.82
4	0.58	0.46	0.97	0.84
5	0.60	0.45	1.01	0.84
6	0.64	0.45	1.02	0.86
7	0.65	0.45	1.03	0.86
8	0.59	0.48	1.01	0.92
9	0.66	0.49	1.07	0.91
10	0.63	0.52	1.05	0.93
11	0.64	0.44	1.07	0.86
12	0.54	0.45	1.01	0.88
13	0.64	0.49	1.05	0.89
14	0.71	0.63	0.97	0.89
15	0.56	0.46	0.96	0.85
16	0.56	0.47	0.99	0.89
17	0.56	0.38	1.00	0.85
18	0.55	0.45	0.98	0.87
19	0.56	0.47	0.99	0.85

Table S11. Best fitted parameters (χ_T, χ_S, τ and α) with the extended Debye model for compound **1** at 1500 Oe in the temperature range 2-9 K.

T / K	χ_T / cm^3 mol^{-1}	χ_S / cm^3 mol^{-1}	α	τ / s	R^2
2	5.74167	0.2865	0.39965	0.06397	0.99735
2.2	5.07811	0.31597	0.36742	0.0428	0.99725
2.4	4.50752	0.31958	0.34128	0.02813	0.99707
2.6	4.15552	0.30284	0.3244	0.02001	0.99737
2.8	3.81778	0.32359	0.29646	0.01447	0.99734
3	3.53908	0.32439	0.27252	0.01061	0.99796
3.5	2.98794	0.32866	0.22123	0.00535	0.99756
4	2.6487	0.31245	0.20617	0.00301	0.99891
4.5	2.37043	0.28171	0.19205	0.00178	0.99837
5	2.13267	0.31976	0.15966	0.00117	0.999
5.5	1.94718	0.29458	0.15437	7.76007E-4	0.99921
6	1.78497	0.29755	0.14279	5.42872E-4	0.99904
7	1.5342	0.31015	0.10887	3.04707E-4	0.99974
8	1.3463	0.33335	0.08695	1.8804E-4	0.99951
9	1.20629	0.38124	0.07992	1.21983E-4	0.99849

Table S12. Best fitted parameters (χ_T, χ_S, τ and α) with the extended Debye model for compound **2** at 1500 Oe in the temperature range 2-4 K.

T / K	χ_T / cm^3 mol^{-1}	χ_S / cm^3 mol^{-1}	α	τ / s	R²
2	0.10428	0.573	0.39965	0.06397	0.99735
2.2	0.13473	0.63194	0.36742	0.0428	0.99725
2.4	0.11045	0.63916	0.34128	0.02813	0.99707
2.6	0.11628	0.60569	0.3244	0.02001	0.99737
2.8	0.0598	0.64717	0.29646	0.01447	0.99734
3	0.0617	0.64877	0.27252	0.01061	0.99796
3.5	0.0038	0.65732	0.22123	0.00535	0.99756
4	0.00121	0.62489	0.20617	0.00301	0.99891

Table S13. Best fitted parameters (χ_T, χ_S, τ and α) with the extended Debye model for compound **4** at 1500 Oe in the temperature range 2-6.5 K.

T / K	χ_T / cm^3 mol^{-1}	χ_S / cm^3 mol^{-1}	α	τ / s	R²
2	8.68446	2.22778	0.60558	0.0031	0.99996
2.2	7.39879	2.70677	0.48646	0.00306	0.99996
2.4	6.78453	2.63043	0.4442	0.00252	0.99998
2.6	6.27691	2.56915	0.39582	0.00209	0.99994
2.8	5.87255	2.4536	0.36616	0.00177	0.99992
3	5.51625	2.33696	0.34328	0.00151	0.99991
3.5	4.7828	2.20781	0.26189	0.00116	0.99991
4	4.2342	1.95039	0.23555	7.76975E-4	0.99989
4.5	3.80447	1.7619	0.20807	5.6667E-4	0.99991
5	3.43519	1.64762	0.18245	4.1745E-4	0.9999
5.5	3.14067	1.43666	0.18582	2.85705E-4	0.9999
6	2.88395	1.3657	0.16602	2.17276E-4	0.99992
6.5	2.48511	1.20961	0.14519	1.27156E-4	0.99992

Table S14. Best fitted parameters (χ_T, χ_S, τ and α) with the extended Debye model for compound **7** at 1500 Oe in the temperature range 2-4 K.

T / K	χ_T / cm^3 mol^{-1}	χ_S / cm^3 mol^{-1}	α	τ / s	R²
2	5.85941	0.88878	0.3624	0.08478	0.99925
2.2	5.35024	0.97461	0.32681	0.08041	0.99882
2.4	4.98382	1.15039	0.27966	0.0481	0.99943
2.6	4.6802	1.07909	0.27301	0.03799	0.99951
2.8	4.52946	0.87925	0.3065	0.03278	0.99962
3	4.23086	0.81738	0.28879	0.02845	0.99958
3.5	3.71686	0.6043	0.28288	0.01851	0.99978
4	3.31412	0.36234	0.30653	0.01956	0.99948

Table S15. Best fitted parameters (χ_T, χ_S, τ and α) with the extended Debye model for compound **11** at 1500 Oe in the temperature range 2-4.5 K.

T / K	χ_T / cm^3 mol^{-1}	χ_S / cm^3 mol^{-1}	α	τ / s	R^2
2	5.26007	0.21482	0.32753	0.00106	0.99986
2.2	4.91727	0.24516	0.32705	8.60562E-4	0.99986
2.4	4.56367	0.26842	0.33191	6.60046E-4	0.99983
2.6	4.27844	0.25961	0.33122	5.1069E-4	0.99989
2.8	4.02019	0.31684	0.331	4.15771E-4	0.99989
3	3.79369	0.29642	0.34117	3.19953E-4	0.99991
3.5	3.31336	0.42175	0.33377	2.04467E-4	0.99992
4	2.94674	0.45434	0.34921	1.25088E-4	0.99994
4.5	2.64968	0.54061	0.34784	8.93361E-5	0.99992

Table S16. Best fitted parameters (χ_T, χ_S, τ_1, τ_2, α and β) with the extended Debye model for compound **15** at 1500 Oe in the temperature range 2-12 K. τ_1 and τ_2 are the two relaxation times and β the ratio between the these two processes amplitude.

T / K	χ_T / cm^3 mol^{-1}	χ_S / cm^3 mol^{-1}	β	τ_1 / s	τ_2 / s	α	R^2
2	0.29098	9.71031	0.71674	1.20776	0.00147	0.49133	0.99991
2.2	0.33675	9.16813	0.72201	1.05834	0.00129	0.48042	0.99991
2.4	0.40459	7.54444	0.70305	0.47535	9.85863E-4	0.44512	0.99991
2.6	0.40065	6.90708	0.70129	0.34022	7.50432E-4	0.43166	0.99994
2.8	0.42787	6.34207	0.70373	0.23943	5.95928E-4	0.41633	0.9999
3	0.46974	5.79555	0.70424	0.16428	5.00198E-4	0.39284	0.99994
3.5	0.5448	4.91337	0.71722	0.08112	3.37201E-4	0.35028	0.99996
4	0.58094	4.26523	0.73301	0.04274	2.22346E-4	0.31635	0.99994
4.5	0.58303	3.78414	0.74005	0.02527	1.60362E-4	0.28558	0.99993
5	0.31324	3.42732	0.71 (fixed)	0.01503		0.28888	0.99973
5.5	0.31759	3.10998	0.71 (fixed)	0.00988		0.26658	0.99979
6	0.32595	2.85059	0.71 (fixed)	0.00678		0.2513	0.99975
7	0.36286	2.44538	0.71 (fixed)	0.00351		0.22921	0.99975
8	0.44256	2.14006	0.71 (fixed)	0.00197		0.20916	0.99983
9	0.55738	1.89957	0.71 (fixed)	0.00114		0.18777	0.99983
10	0.84504	1.72001		5.01853E-4		0.23088	0.99986
11	0.89023	1.56452		2.67254E-4		0.21843	0.9999
12	0.93013	1.42503		1.34871E-4		0.20637	0.99997

Table S17. Parameters of the magnetic relaxation processes for the heterobimetallic compounds.

Compounds		Orbach		Raman	
		τ_0 / s	Δ / K	C / $s^{-1}K^{-n}$	n
1		5.84(11)×10^{-5}	21.1(7)	0.94(3)	4.03(3)
2		1.50(89)×10^{-8}	31.8(25)	392.2(56)	2.46(19)
4		3.64(66)×10^{-6}	25.9(12)	81.6(73)	1.55(11)
7		6.82(39)×10^{-8}	26.7(24)	405.1(16)	1.36(55)
9		3.18(34)×10^{-8}	31.7(47)	1598.8(87)	2.18(7)
11		3.84(76)×10^{-6}	16.0(22)	233(111)	1.86(80)
15	Dy1	/	/	0.03(1)	4.77(10)
	Dy2	/	/	90.45(6)	2.81(6)
16		3.07(24)×10^{-4}	13.4(5)	/	/

References

1 M. F. Richardson, W. F. Wagner and D. E. Sands, *J. Inorg. Nucl. Chem.,* 1968, ***30***, 1275-1289.
2 A. I. Vooshin, N. M. Shavaleev and V. P. Kazakov, *J. Lumin.* 2000, **91**, 49-58.
3 M. Feng, F. Pointillart, B. Lefeuvre, V. Dorcet, S. Golhen, O. Cador and L. Ouahab, *Inorg. Chem.,* 2015, **54**, 4021-4028.
4 G. M. Sheldrick, A*cta Crystallogr., Sect. A Found Adv.,* 2015**, 71**, 3–8.
5 G. M. Sheldrick, *Acta Crystallogr. Sect. C,* 2015, **71**, 3-8.
6 A. L. Spek, *J. Appl. Crystallogr.,* 2003, **36**, 7-13.